THE HONG KONG
POLYTECHNIC UNIVERSITY
香港理工大學
Pao Yue-kong Library
包玉剛圖書館

Copyright Undertaking

This thesis is protected by copyright, with all rights reserved.

By reading and using the thesis, the reader understands and agrees to the following terms:

1. The reader will abide by the rules and legal ordinances governing copyright regarding the use of the thesis.

2. The reader will use the thesis for the purpose of research or private study only and not for distribution or further reproduction or any other purpose.

3. The reader agrees to indemnify and hold the University harmless from and against any loss, damage, cost, liability or expenses arising from copyright infringement or unauthorized usage.

Pao Yue-kong Library, The Hong Kong Polytechnic University, Hung Hom, Kowloon, Hong Kong

http://www.lib.polyu.edu.hk

GAN-BASED OPTOELECTRONIC DEVICES FOR LIQUID PROPERTIES DETECTION

LU GAOFEI

PhD

The Hong Kong Polytechnic University

2024

The Hong Kong Polytechnic University

Department of Applied Physics

GaN-based Optoelectronic Devices for Liquid Properties Detection

LU Gaofei

A thesis submitted in partial fulfilment of the requirements for the degree of Doctor of Philosophy

August 2023

CERTIFICATE OF ORIGINALITY

I hereby declare that this thesis is my own work and that, to the best of my knowledge and belief, it reproduces no material previously published or written, nor material that has been accepted for the award of any other degree or diploma, except where due acknowledgement has been made in the text.

_____ (Signed)

_____ LU Gaofei _____ (Name of student)

Abstract

Measurement of liquid properties holds significant research importance across fields such as environmental protection, the food industry, manufacturing processes, and so on. The investigation of liquid properties detecting is therefore deemed a top priority. The most commonly used liquid sensing methods, electrical and optical methods, offer their own advantages. However, electrical methods cannot guarantee measurement accuracy in electromagnetic environments, while optical methods are limited by the large size external light source. In order to develop compact liquid sensor, in this thesis, monolithically integrated GaN-based optoelectronic devices are adopted. These GaN devices integrate both light-emitting diode (LED) and photodetector (PD) on the same sapphire substrate, which simultaneously enables both light emission and light detection, enabling precise and portable optoelectronic sensing for liquid properties detection.

First, the monolithically integrated GaN device is fabricated for droplet flow monitoring. When the droplet slides across the device, the reflectance at the sapphire boundary decreases due to reduced refractive index contrast, thereby decreasing the quantity of light reflected onto the PD. The integrated device provides a fast transient response with rise and fall times of 3.88 µs and 3.53 µs, achieving instantaneous droplet flow sensing.

Then, a monolithically integrated optoelectronic device, equipped with an indicator film, is fabricated for enhanced pH detection. The pH sensor showcases a

swift reaction time and an extensive linear range, achieving real-time pH detection with a minimal 1 µL sample and a response time of merely 3.8 s. The wide linear range of 5-13 pH of the sensor demonstrates its promise for practical applications.

Finally, the GaN optoelectronic device is designed for organic liquid identification facilitated with photonic crystals. Meanwhile, the reflectance spectrum shift of photonic crystals in interaction with organic molecules is explored. The proposed optoelectronic device could identify 7 kinds of organic solvents in less than 30 s with reproducibility, which offers a viable solution for rapid response and decision-making in emergency situations such as chemical spills, replacing complicated laboratory analysis.

Publications

1. **G. Lu,** X. An, Y. Luo, Y. Chai and K. H. Li, "Droplet Microsensors Based on GaN Diode Optopairs," 2022 Asia Communications and Photonics Conference (ACP), Shenzhen, China, 2022, pp. 1970-1973, doi: 10.1109/ACP55869.2022.10088713

2. H. Yang[#], Y. Luo[#], **G. Lu**[#], Y. Chai, Z. Chu and K. H. Li, "Viscosity Sensors Based on III-Nitride Optical Devices Integrated With Droplet Sliding Channels," IEEE Electron Device Letters, vol. 43, no. 12, pp. 2169-2172, Dec. 2022, doi: 10.1109/LED.2022.3214830 ([#] co-first authors)

3. **G. Lu**, X. An, Y. Luo, H. Yang and K. H. Li, "Droplet Flow Sensors based on GaN Integrated Devices," The 14th International Conference on Nitride Semiconductors (ICNS-14), Fukuoka, Japan, 2023

4. **G. Lu**, J. Chen, Y. Chai, and K. H. Li, "GaN optical devices integrated with sol-gel films for pH detection," IEEE Transactions on Electron Devices, 2023, Under review

5. **G. Lu**, Y. Chai, and K. H. Li, "An optoelectronic device for organic solvents identification: assembled of photonic crystal and monolithic integrated photonic chip," In preparation

Acknowledgments

I would like to take this opportunity to express my heartfelt gratitude to all those who have helped me.

First of all, I want to express my gratitude to my supervisors, Prof. CHAI Yang and Dr. LI Kwai Hei. This thesis was completed under the careful supervision of Prof. CHAI and Dr. LI. Prof.CHAI's profound professional knowledge, rigorous attitude and friendly way of treating students had a profound impact on me. Dr. LI inspired me with his unique insights and many innovative ideas. He not only taught me the basic research methods and experimental skills, but also helped and encouraged me in my daily life.

Many thanks to Dr. CHEN Liang, YU Binlu, AN Xiaoshuai, YIN Jiahao, and CHEN Jian for their guidance in experimental skills and help in life. Thanks to my lively, cute and mature senior sister, LUO Yumeng, for adding colors to my research life. Thanks to my meal partner and also experiment mate, YANG Hongying, for her encouragement. Sincerely wish her happiness in her life. I would like to thank TU Yang, PAN Liushu, LIU Zecong, GENG Fan, and other colleagues for their help in creating a vibrant academic atmosphere in the lab.

My thanks are also due to Dr. CAI Lejuan and Ms. WANG Cong from Prof. CHAI Yang's group and Ms. JIANG Biyi from Dr. ZHOU Feichi's group. Thanks to all colleagues in the DE406 office of PolyU and the 401, 404, 509 offices of the School of Microelectronics in SUSTech, former classmates of QUST and OUC, and partners in the "What exactly is this group~" and the "Sports Group". Thanks to my cats Daodao,

Lele and Xiaoheizi.

The highest gratitude goes to my family for giving me the selfless love and relaxed upbringing that was enough to allow me to pursue my studies without any worries.

Finally, I would like to thank my husband, Dr. LIN Fei, for his accompany and support. You are the gift from fortune.

Table of Contents

List of Figures

gases under the interference of magnet.

List of Tables

List of Abbreviations

A	Amp
Al	Aluminum
Al_2O_3	Aluminum oxide
AlGaN	Aluminum gallium nitride
AlN	Aluminum nitride
Ar	Argon
Au	Gold
CBL	Current blocking layer
CKT	Conductive circuit
Cp_2Mg	Cyclopentadienyl magnesium
Cr	Chromium
CRI	Color rendering index
Cu	Copper
DBR	Distributed Bragg Reflector
DI	Distilled
DIC	Differential interference contrast
DCS	Destabilization of colloidal solutions
EL	Electroluminescence
EM	Electromagnetic

E-nose	Electronic nose
FCC	Face-centered cubic
FDTD	Finite-difference time-domain
Ga	Gallium
GaAs	Gallium arsenide
GaN	Gallium nitride
Ge	Germanium
HEMT	High-electron mobility transistor
HF	Hydrofluoric acid
HSP	Hansen solubility parameter
IC	Integrated circuit
ICP	Inductively coupled plasma
In	Indium
InGaAlN	Indium aluminum gallium nitride
InGaN	Indium gallium nitride
InN	Indium nitride
IR	Infrared
ISO	Insulation layer
ITO	Indium Tin Oxide
I-V	Current-voltage
LED	Light-emitting diode
LD	Laser diode

mA   Milliamp

MDP   Minimum detectable photon

MEMS   Microelectromechanical systems

Mg   Magnesium

MIS   Metal-insulator-semiconductor

MOCVD   Metal-Organic chemical vapor deposition

MQW   Multiple-quantum wells

MSM   Metal-semiconductor-metal

NEMS   Nanoelectromechanical systems

n-GaN   n-type gallium nitride

NV   Nitrogen vacancy

O_2 Oxygen

OLED   Organic light-emitting diode

PBS   Phosphate buffer solutions

PCB   Printed circuit board

PD   Photodetector

PDMS   Polydimethylsiloxane

PECVD   plasma-enhanced chemical vapor deposition

PET   Poly(ethylene terephthalate)

p-GaN   p-type gallium nitride

PMU   Polymerization of molecular units

P-nose   Photonic noses

PPG   Photo-plethysmography

PS   Polystyrene

PSS   Patterned sapphire substrates

PSV   Passivation layer

Pt   Platinum

RGB   Red-green-blue

RH   Relative humidity

RI   Refractive index

Si   Silicon

SiC   Silicon carbide

SiH_4 Silicon tetra hydroxide

SiO_2 Silicon dioxide

SiV   Silicon vacancy

TE   Transverse electric

TM   Transverse magnetic

TCL   Transparent conductive layer

TD   Threaded dislocation

TEOS   Tetraethoxysilane

Ti   Titanium

TiO_2 Titanium dioxide

TIR   Total internal reflection

TMGa   Trimethyl gallium

u-GaN   Undoped gallium nitride

UV   Ultraviolet

V   Volt

V_f Forward voltage

W   Watt

Zn   Zinc

ZnO   Zinc oxide

Chapter 1 Introduction

1.1 Background of GaN-based optoelectronic devices

The rapid evolution of modern electronic technology has spurred research and development efforts towards compact, efficient, robust, and cost-effective optoelectronic devices. This development is quickly becoming a major focal point in the electronic industry. Emerging from these efforts are integrated optoelectronic devices. These remarkable innovations seamlessly meld optoelectronic components, such as light sources, light detectors, and light modulators, with microelectronic elements like logic and analogue circuits on a single chip. This new era of devices dramatically enhances system integration and reliability while boosting transmission rates. Furthermore, they pave the way for substantial cost reductions, setting a new standard of electronics.

Since the 1950s, the rapid advancement of microelectronics, centered on integrated circuits (ICs), has been largely propelled by first-generation semiconductor materials, prominently silicon (Si). However, Si's suitability for optoelectronics and high-frequency, high-power devices is constrained by its narrow band gap, limited electron mobility, and low breakdown electric field. This led to the emergence of the second generation of semiconductor materials, typified by gallium arsenide (GaAs), which found application in optoelectronics, particularly in infrared lasers and high-luminosity red diodes[1].

The breakthrough in p-type doping of gallium nitride (GaN) materials, coupled

with the successful development of high-brightness blue light-emitting diodes (LEDs) and blue laser diodes (LDs), heralded the onset of the third generation of semiconductor materials. This generation encompasses wide-band materials like GaN, silicon carbide (SiC), and zinc oxide (ZnO). Figure 1.1 illustrates the electron-hole recombination in direct and indirect band gap semiconductors.
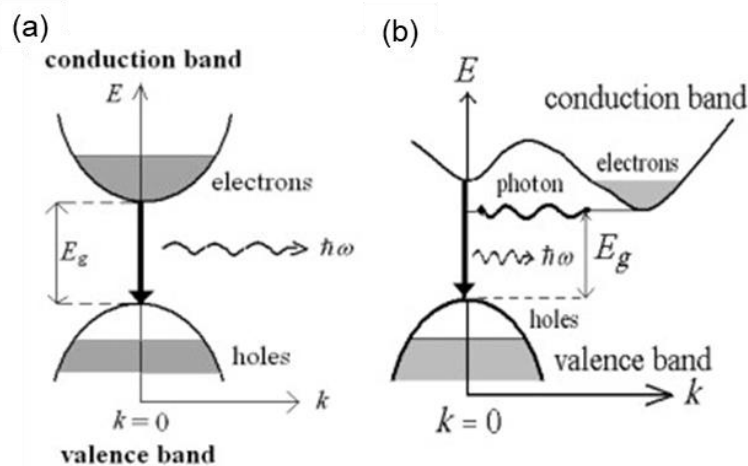
Figure 1.1 Schematic diagram of (a) direct band gap semiconductor and (b) indirect band gap luminescence process [2].

LEDs are semiconductor devices that emit light or generate induction currents when exposed to electrical excitation or external illumination. There are two main categories: inorganic LEDs, with a light-emitting layer exclusively formed from inorganic materials, and organic light-emitting diodes (OLEDs), which use organic compounds to emit light. A specific subtype of inorganic LEDs is nitride-based LEDs, compound semiconductors comprised of various nitrides. These nitride semiconductors include binary compounds (e.g., GaN, indium nitride (InN), aluminum nitride (AlN)), ternary compounds (e.g., indium gallium nitride (InGaN), aluminum gallium nitride (AlGaN)), and quaternary compounds (e.g., indium aluminum gallium nitride

(InGaAlN)). They are known as III-V semiconductors, akin to elemental semiconductors such as Si and germanium (Ge), due to their formation involving an alloy of one, two, or three Group III elements with Group V elements. These devices emit light when an electron in the conduction band recombines with a hole in the valence band, discharging energy as a photon. The frequency and wavelength of this photon, defined by Planck's equation, correlate directly with the bandgap of the material, resulting in light of a specific color [3].

The operational principles of LEDs rest on the concept of bandgap energy (E_g), defined by the equation:

$$E_g = h\gamma = \frac{hc}{\lambda} \tag{1.1}$$

Here, h signifies Planck's constant $h = 6.626 \times 10^{-34}$ J/s, γ is the light frequency, c is the speed of light in vacuum, and λ is the wavelength. The key advantage of compound semiconductor alloys, such as nitride semiconductors, lies in their tunability of this bandgap energy. In the $In_xGa_{1-x}N$ alloys, varying the indium content (x) from 0.02 to 0.3, for example, the bandgap reduces from 3.19 eV to 2.82 eV, shifting the emission wavelength from 390 nm to 440 nm. This bandgap engineering technique enables the attainment of emission wavelengths across the infrared (IR), visible, and ultraviolet (UV) segments of the electromagnetic (EM) spectrum. Nitride semiconductors are also classified as direct bandgap materials, signifying that the highest electron transition from the valence band to the conduction band minimum doesn't require momentum change, thereby allowing for a higher concentration of electron-hole pairs to undergo radiative recombination. This property starkly contrasts

with indirect bandgap semiconductors like Si and Ge, where any transition between the valence and conduction bands necessitates a momentum shift. Radiative recombination in such materials involves the absorption or emission of phonons (lattice vibrations), rendering it less likely within a given timeframe (typically 10^{-8} s). Thus, the direct bandgap characteristics of nitride semiconductors make them the ideal choice for fabricating optoelectronic components such as LEDs, solar cells, and lasers.

Among the plethora of nitride semiconductors, GaN has garnered significant attention due to its outstanding properties, such as high electron mobility and high electron saturation drift rate. These attributes make GaN a material of choice for the fabrication of LEDs, high-electron mobility transistors (HEMTs), and high-power electronic switches. The advancement and diversity of contemporary discrete GaN devices have paved the way for the integration of GaN platforms, thereby expanding their applicability in various domains.

The pioneering nitride-based p-n junction blue LED was developed by Isamu Akasaki in 1989, marking a watershed moment in this domain [4]. This technological leap was primarily attributed to a significant enhancement in GaN crystal quality, achieved by the successful p-doping of GaN through low-energy electron beam irradiation with zinc (Zn) or magnesium (Mg). Despite its innovative nature, this method posed challenges for large-scale production and the involved mechanism remained not fully elucidated. A notable advancement was made in 1993 when Shuji Nakamura invented the first high-brightness InGaN-based blue LED, further propelling the field of optoelectronic devices[5]. Nakamura's innovative approach of employing

thermal annealing further refined the method, rendering it more appropriate for mass production. In collaboration with his team, he unraveled the underlying physical problem, demonstrating that the strong p-type GaN resulted from the passivation of the acceptor in GaN due to hydrogen. The subsequent advancements in nitride-based devices have been momentous, leading to the creation of durable violet LDs, green LEDs, UV detectors, and HEMTs. The development of short-wavelength LEDs in the blue and UV ranges has notably expedited the evolution of white LEDs. Presently, two primary methods are utilized for generating white light from LEDs. The first method, a multi-chip approach, amalgamates the light emitted from three closely situated LED chips—red, green, and blue—to yield white light in the appropriate ratio. This red-green-blue (RGB) color mode can achieve a high color rendering index (CRI), but its intricacy lies in the requirement of multiple LED chips and electronic circuitry to regulate color mixing, which complicates the design of packages and illuminators. Hence, this method is predominantly employed for color-tunable LEDs rather than white LEDs. The second method is a monolithic approach that relies on a single LED chip emitting short-wavelength light (typically blue or ultraviolet). This light is then used to excite a phosphor layer positioned atop the chip, ultimately producing white light.

A photodetector (PD), also referred to as a photosensor, is an optical device engineered to detect target signals[6]. It achieves this by transforming incident light into electrical energy, either in the form of photovoltage or photocurrent. PDs find utility in numerous applications, ranging from smoke and flame detection to radiation

monitoring [7-9]. The predominant types of PDs, including p-n junction and p-intrinsic material-n mode (p-i-n) types, are favored due to their compactness, high switching speed, and efficiency. These types are commonly deployed as avalanche photodiodes and photon counters. Other typical structures, such as metal-semiconductor-metal (MSM) or metal-insulator-semiconductor (MIS) designs, utilize Schottky contacts and offer faster operation than p-n structures, capable of reaching frequencies up to several hundred GHz[10]. As crucial detection elements within integrated optoelectronic devices, PDs see widespread use in diverse fields, including biomedical applications, environmental monitoring, and communication technologies. Among these, silicon PDs are the most prevalent, attributed to their cost-effectiveness and the maturity of their manufacturing process. While optoelectronic integrated systems founded on silicon material platforms have been thoroughly investigated and demonstrated high performance in terms of on-chip integration of light modulators, amplification, and detection, a significant bottleneck persists. Silicon, possessing an indirect bandgap, lacks the capacity for light emission, thus obstructing the monolithic integration of light sources with other optical devices. Various research endeavors have attempted to integrate light sources with silicon PDs using wafer bonding. However, this method remains confined to the laboratory phase and is not suitable for mass production due to its high costs, complex process, and low success rate. Furthermore, during the practical application of photodetection, the majority of commercial PDs necessitate supplementary integration of light sources and waveguides. This requires additional intricate and precise alignment steps to establish a complete photodetection system.

Such detection systems are typically bulky and expensive, presenting numerous practical challenges. Therefore, the development of PDs, which can seamlessly integrate light emitting and detecting functionalities in a cost-effective and reliable manner, holds significant practical value.
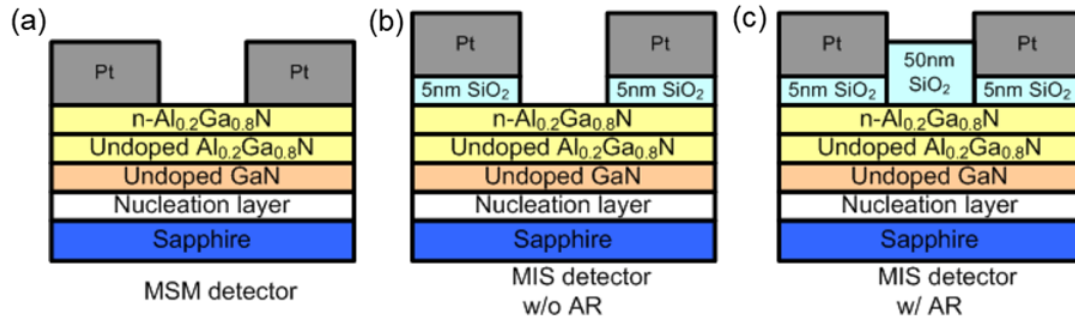
Figure 1.2 Three different AlGaN/GaN PD structures: (a) MSM detector, (b) MIS detector without anti-reflection coating and (c) MIS detector with anti-reflection coating[11].

Figure 1.2 depicts the structural layout of PDs. The assessment of a PD performance encompasses several key metrics, which are listed below:

The responsiveness refers to the PD ability to react or respond to incoming light. The response speed indicates the requirement for a high-frequency response under specific conditions. Noise level denotes the discernibility between the incident light and the noise signal, essentially measuring the PD ability to distinguish useful signals from background noise. The reliability represents the PD ability to maintain its functionality and stability over prolonged periods of operation. And finally is the cost of PDs. It is desirable for the device to be manufacturable at a low cost, a factor which holds significant importance for its broader applications and market feasibility.

Among these fundamental metrics, responsiveness stands out as one of the most

crucial criteria when evaluating the performance of PDs. Responsivity can be defined as the ratio of the output electrical power (commonly quantified as photocurrent or photovoltage) to the incident input optical power. For a specific material, the responsivity often fluctuates with wavelength due to differing band gaps. Hence, it is essential to compute the responsivity at a specific wavelength. The subsequent equation illustrates the model leveraged to calculate the responsivity [12].

$$R_I = \frac{\lambda \eta}{hc} qg \tag{1.2}$$

In this equation, λ denotes the wavelength, h represents Planck's constant, c is the speed of light, q signifies the electron charge, while η and g correspond to the quantum efficiency and photocurrent gain, respectively.

GaN LEDs have undergone rapid industrialization and their luminous efficiency has experienced significant enhancements, which positions GaN and its compounds as the optimal material platforms for the realization of high luminous efficiency light sources and widespread lighting. GaN also boasts a high photoelectric conversion efficiency in the UV band due to its energy band gap of 3.2eV, making it an ideal material choice for UV PDs. Presently, there is a myriad of ongoing studies focused on the design and performance improvement of GaN-based UV PDs. However, although it seems relatively straightforward to execute UV PD manufacturing using the GaN platform, most GaN UV PDs rely on a MSM structure [13, 14]. This structure deviates considerably from the heterojunction structure of multiple quantum wells (MQWs) prevalent in GaN LEDs, thereby preventing the utilization of the same semiconductor process for growth and fabrication and precluding monolithic on-chip integration.

Therefore, to bring to fruition a dual-function optoelectronic device that embodies both light emission and detection, it is paramount to investigate how GaN and its compounds can be harnessed to generate heterojunction devices proficient in light sensing.

With ongoing research into GaN/InGaN MQWs heterojunctions, the Stokes effect has been identified. This revelation has enabled MQWs to produce both electroluminescence and photovoltaic conversion, and generate photocurrents in response to illumination. This pivotal discovery lays a firm theoretical groundwork for the simultaneous fabrication of LEDs and PDs on a unified platform of GaN and its compounds. However, the next necessary step is to design the device in such a way that there is efficient optical coupling between the LED and the PD. A potential solution could be to package two distinct LEDs and PDs in parallel, allowing for simultaneous emission and sensing. This system-level integration, though, might inflate costs and diminish the overall optical coupling efficiency of the device, necessitating exploration into chip-level monolithic integration and optical coupling.

The maturity of GaN epitaxial growth on sapphire substrates and the subsequent semiconductor processing presents an opportunity to produce both LEDs and PDs on a single epitaxial wafer of the sapphire substrate. This would allow for the alteration of the PD photocurrent by changing the refractive index of the sapphire/air interface. Additionally, the sapphire substrate is transparent and functions as a natural optical waveguide, seamlessly guiding a portion of the light from the LED into the monolithic PD without the need for external optical coupling elements, thus reducing coupling loss. Furthermore, the stability, corrosion-resistance, and processability of sapphire allows it

to integrate with other sensitive materials to convert relevant external physical, chemical, and biological changes into light and electrical signals. Ultimately, this flip-chip monolithically integrated GaN LED-PD photoelectric sensor device, due to its simplistic design and compatibility with mature processing technologies, holds promise for high-level integration, cost-effectiveness, and miniaturization. This is of paramount importance in sensor applications as it addresses the challenges associated with the complex and costly composition of traditional optical sensor systems[15].

To achieve high-performance sensing solutions, semiconductor-based optoelectronic devices present a promising strategy. These devices have the ability to concurrently serve as light sources, detectors, and even waveguides, offering the convenience of monolithic integration to minimize optical losses and enhance sensor performance while facilitating system miniaturization. GaN-based semiconductors and their alloys, with their direct bandgap, high stability, and extended lifetimes, are suitable for constructing LEDs and PDs that span UV to visible wavelengths[16, 17]. Additionally, these materials can function as waveguides, which lays the groundwork for the potential realization of monolithic integrated GaN refractive index sensors. However, several conditions must be met to actualize monolithic integrated GaN sensor devices. The first condition is successful monolithic integration of LEDs and PDs on GaN material with appropriate waveguide channels. Then, the efficient optical coupling between the PD and LED should along with the capability to accomplish photoelectric conversion. Lately, the establishment of an effective sensing mechanism correlating photocurrent and refractive index could achieve high-performance refractive index

sensing[18].

1.1.1 Light emitting mechanism and properties of GaN-based LED
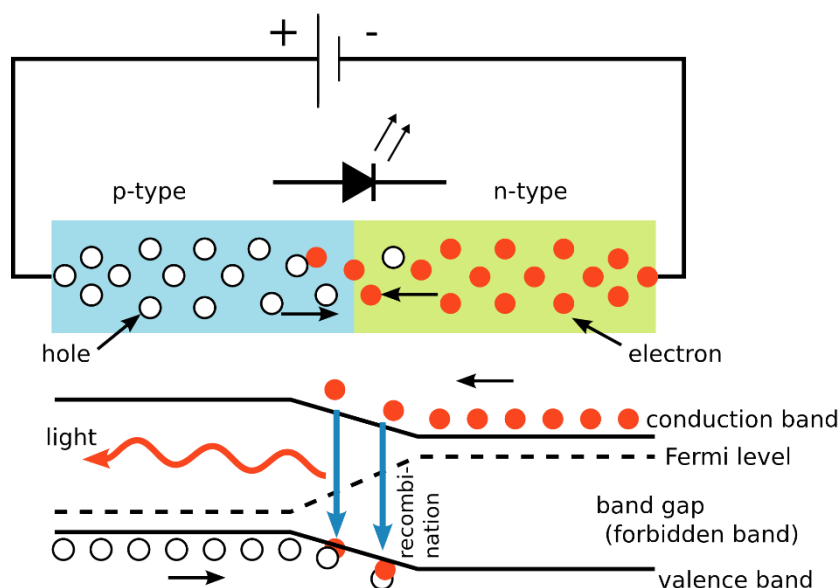
Figure 1.3 Schematic diagram of LED light-emitting principle[19].

In Figure 1.3, when a forward voltage is applied, electrons are injected from the
n-type region into the p-type region, and vice versa for holes. These carriers recombine
at the p-n junction, releasing photons to produce visible light. The MQWs structure,
composed of several ultra-thin quantum well layers, is situated between the p-type and
n-type semiconductors. It plays a crucial role in regulating the movement of carriers
within the device, thereby enhancing the performance of the devices. The quantum
effect induced by the MQWs structure significantly elevates the luminescence and
spectral purity, which are key in fabricating optoelectronic devices such as laser diodes
and LEDs.

According to this principle, the thickness of the quantum well layer in the MQWs
structure controls the energy distribution of carriers, allowing for the band gap width of
the device to be adjusted to produce and absorb light of varying wavelengths. In

addition to the MQWs structure, LEDs can also employ techniques such as multi-color coupling and monochromatic addition of phosphor to emit white light. The optical properties of LEDs can be described as the release of energy, and thus the production of photons, when an electron in the semiconductor material undergoes a transition through a specific energy level. LEDs excite electron transitions and generate photons by injecting current.
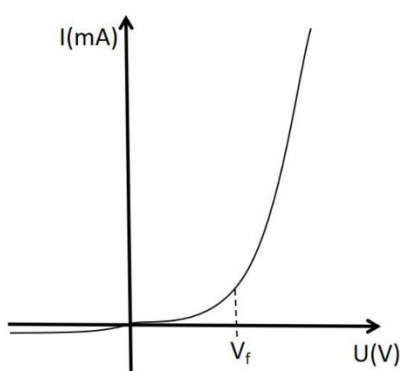
Figure 1.4 The typical I-V Characteristic Curves of LEDs.

In Figure 1.4, the X-axis represents the magnitude of the forward current in milliamps (mA), and the Y-axis represents the magnitude of the forward voltage in volts (V). The curve depicts the forward characteristics of the LED. As the forward voltage increases, the forward current also increases. When the voltage reaches the LED forward voltage (V_f), the current surges dramatically, establishing a linear relationship with the voltage thereafter. Conversely, in the reverse characteristics of the LED, the reverse current is minimal and usually deemed negligible. The current-voltage (I-V) characteristics of different LEDs will differ, and their specific characteristic curves are influenced by factors such as the material, device structure, and fabrication process.

1.1.2 Photodetecting mechanism and properties of GaN-based PD

The fundamental principle of a photodetector revolves around the utilization of the photoelectric effect to transform photons into electrons. Subsequently, the movements of electrons are measured through a circuit to derive information about the intensity and wavelength of the light signal.

The basic principle of a photodetector can be divided into the following stages. The first stage is photoelectric conversion. Upon exposure to incident light in the photosensitive region of the photodetector (typically a p-n junction), photons get absorbed and transformed into electron-hole pairs, a process known as photoelectric conversion. Charge carrier flow is appeared at the nest stage. It refers to the combination of electrons and holes generated by the photoelectric conversion. These charges formed in the PN junction propagate in different directions under the combined influence of the internal electric field and external electric field, resulting in current flow. Finally is the signal amplification. The weak current generated is amplified through a circuit to enable it to be read and processed. Generally, the output signal of a photodetector is a current or voltage. Common photodetectors include photodiodes, photomultiplier tubes, and photoconductive detectors. Different photodetectors have different methods of photoelectric conversion and mechanisms for charge carrier flow. It is important to note that different photodetectors have different performance indicators and applicable ranges, so comprehensive considerations based on specific application requirements are needed when selecting a photodetector.

The performance indicators of a photodetector are important criteria for evaluating its detection capability and effectiveness. These primarily encompass the aspects such

as spectral response, device noise, detection sensitivity, response time, and saturation of optical power.

The sensitivity of a photodetector to various wavelengths of light is often gauged through its responsivity. Responsivity signifies the current/voltage produced per unit of optical power impinging upon the detector. It is quantified as the ratio of photocurrent or voltage to optical power, denoted in amps/watt (A/W) or volts/watt (V/W).

The PD sensitivity can be accurately evaluated by measuring its responsivity to different light wavelengths. Responsivity denotes the current/voltage generated per unit of incident optical power on the detector. It equates to the ratio of photocurrent/voltage to optical power, represented in amps/watt or volts/watt.

The aptitude of a photodetector to discern optical signals is typically measured by the minimum detectable photon (MDP) number, calculated using the following formula:

$$\text{MDP} = \frac{(2qI_d n_B + 4kTB\Delta f)}{A} \tag{1.3}$$

where q is the elementary charge, Id is the dark current of the detector, nB is the carrier concentration, k is the Boltzmann constant, T is the temperature, B is the width of the charge depletion region, Δf is the bandwidth of the detector, and A is the detection area.

The efficiency of PDs can be determined by inspecting their rise and fall times. The rise time and fall time refer to the time taken for the detector output signal to traverse from 10% to 90% and vice versa, respectively. The response time is impacted by factors such as the speed of carrier motion, detector structure, and material used.

This pertains to the maximum optical power that the photodetector can measure.

14

That is, when the incident optical power reaches a particular value, the output current (or voltage) ceases to increase with a rise in incident optical power. The saturation of optical power is influenced by elements like the detector material, structure, and area.

1.1.3 Optical coupling properties and sensing principle of GaN-based monolithic integrated optoelectronic devices
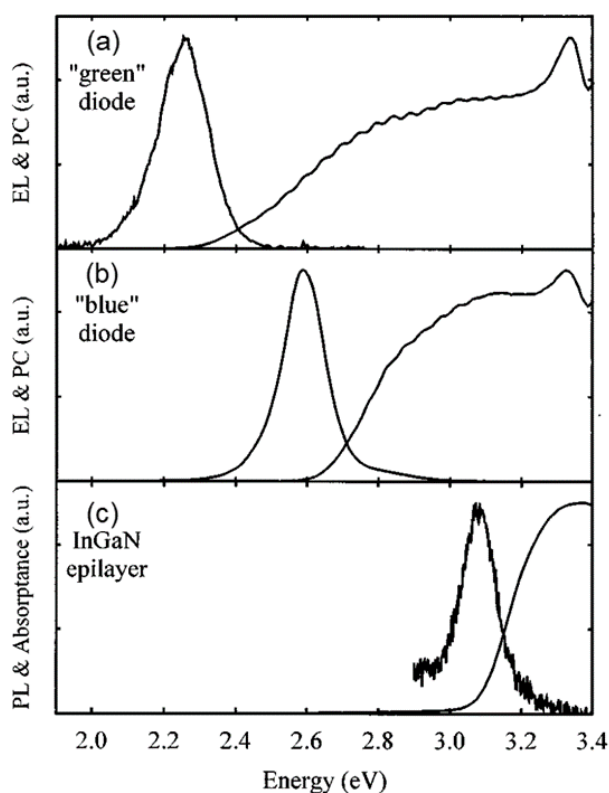
Figure 1.5 Overlap of emission and absorption spectra of different epitaxial

materials[20].

The crux of fabricating a monolithic LED-PD chip that can both emit and detect light lies in achieving an overlap between the LED emission spectrum and the PD absorption spectrum. The degree of this overlap directly influences the PD responsivity, and subsequently, the sensitivity of the photocurrent. Given their identical epitaxial structures, the PD can absorb the light emitted by the homogeneous LEDs, generating

photoinduced electrons and holes that in turn yield a photocurrent. Numerous studies

have illustrated that both LED and PD devices can be fabricated on visible InGaN/GaN

MQWs epitaxial wafers. Due to the Stokes shift, there is a degree of overlap between

their absorption and emission spectra, enabling the PD in a monolithically integrated

device to respond to the LED light. In Figure 1.5, Martin et al. compiled the emission

and absorption spectra of different epitaxial wafers. They discovered that the overlap

between the emission and absorption spectra of UV InGaN/GaN epitaxial wafers

exceeds that of visible light. This conclusion, which asserts that the Stokes shift

diminishes as the indium-doped content in the MQWs decreases, is further validated by

Li et al.'s results[21].
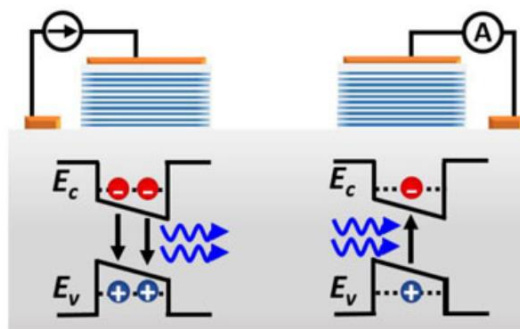
Figure 1.6 Schematic diagram depicting the mechanisms of emission and detection

using identical MQWs structure.

The GaN LED-PD sensor device model and its sensing mechanism constitute the

central scientific focus of this study. Figure 1.6 shows the working principle of the GaN-

based optoelectronic devices with the same MQW structure. When the current is

injected into the LED, the electrons in the conduction band combine with the radiation

from the valence band holes, resulting in light emission from the active region. The PD

in the GaN-based monolithic integrated optoelectronic device works on the opposite principle of the LED. At the same time, the GaN-based materials that generate photons by radiation combination also have the property of generating photocurrents by absorbing photons. For the PD part, the emitted light from LED is coupled through the substrate to the PD, where it is absorbed by the PD. The electrons in the valence band are excited to jump to the conduction band to generate electron-hole pairs, which in turn generate photocurrents. The multiple quantum wells (MQW) structures in the LED and PD are identical, but due to the Stokes shift, the PD can only partially respond to the emitted light from the LED. Still, the overlap of the PD absorption spectrum with the LED emission spectrum is sufficient to detect the change in intensity of the backscattered light signal.

Light undergoes different degrees of reflection as it propagates, and for GaN devices with sapphire substrates, the amount of light captured by PD depends largely on the interface reflection properties. Researchers have used the principle that changes in reflectance can change the intensity of reflected light to sense the amount to be characterized by the detected changes in photocurrent. In addition to directly changing the reflectivity, parameters such as distance, angle and roughness of the applied reflective interface can also affect the photocurrent of the PD.

Moreover, light radiation will be reflected and refracted at the interface of media with different refractive indices. As sapphire has a high refractive index (RI, n=1.77 RIU), if the RI of the test material is less than that of the sapphire, total reflection occurs at the interface, and some light is coupled into the PD, generating a photocurrent.

According to Snell's law (equation 1.4), the total reflection will occur at the sapphire/air interface, causing the emitted light from the LED to be totally coupled to the PD above the angle of $\arcsin(n_1/n_2)$.

$$\theta_c = \sin^{-1} \frac{n_{solution}}{n_{sapphire}} \tag{1.4}$$

where $n_{solution}$ and $n_{sapphire}$ correspond to the refractive indices of air and sapphire, respectively.

When the air medium is replaced by a substance with a different RI, the amount of light received by the PD will change, leading to a change in the photocurrent. Changes in the RI of the material can be continuously detected online by measuring the PD photocurrent, rendering a method that is simple, high-resolution, stable, and reliable.

1.2 Recent progress in GaN based optoelectronic sensor

The preceding section explored the characteristics, parameters, and prevalent integration strategies of various GaN-based optoelectronic devices. In light of recent advancements in wearable sensing and interaction design, the discussion around GaN-based optoelectronic chips within the sensing domain has notably intensified.

The following section will elucidate the sensing principles of GaN-based optoelectronic chips. The design of GaN-based optoelectronic sensors integrated with diverse devices, flexible optical structures, and cutting-edge materials will be summarized and reviewed. This discussion will highlight recent advances in GaN-based optoelectronic sensors, focusing on the varied components combined in the reported optoelectronic chips.

1.2.1 Design and applications of heterogeneously integrated GaN-based optoelectronic devices

While the optoelectronic chip exhibits exceptional sensitivity in areas such as refractive index variation and distance detection, it shows minimal response to physical parameters including angle, pressure, and wind speed. Furthermore, the rigid structure of GaN devices curbs their potential for large-scale flexible applications like motion sensing. Researchers have taken note of these limitations and sought to overcome them through the development of advanced transfer techniques or by incorporating different physical structures into the optoelectronic chip. As a result, these previously unresponsive signals are now successfully converted into optoelectronic signals, thereby broadening the range of applications for the optoelectronic chip. The ability to transfer large-area GaN-based MQW-diodes to flexible substrates holds great significance for flexible optical communications, wearable smart devices, and other applications. Drawing on prior work, as depicted in Figure 1.7 (a), Shi and his team have devised an intermediate wafer-level process to successfully transfer 1.5 mm diameter InGaN/GaN MQW-diodes from silicon substrates to flexible poly(ethylene terephthalate) (PET) substrates[22]. Meanwhile, Lee et al. developed flexible GaN piezoelectric nanogenerators and GaN LEDs using the laser lift-off method (Figure 1.7 (b))[23].
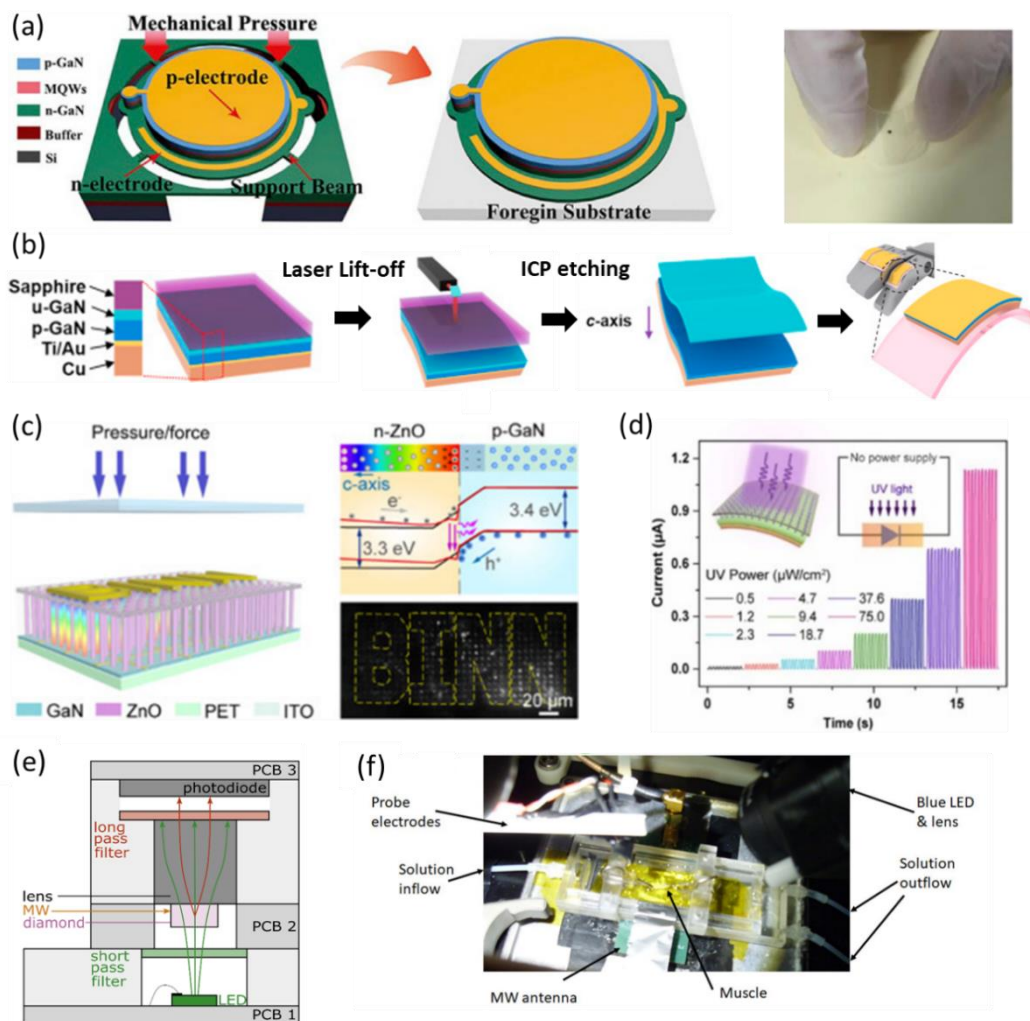
Figure 1.7 (a) Conceptual diagrams detailing the manufacturing processes for the diode situated on the polymer substrate [22]. (b) A series of schematic illustrations showcasing the manufacturing process of the flexible GaN nanogenerator [23]. (c) Operational principal explaining pressure sensor functionality [24]. (d) Working principle of the UV sensor [25]. (e) Design schematic of magnetometer employing NV$^-$ center assemblies [26, 27]. (f) The photograph representing the diamond quantum sensor [28].

The external strain magnitude and bending motion direction can alter the interface polarization charge, with motion information relayed via voltage and

electroluminescence (EL) emission changes. This motion sensor demonstrates exceptional sensitivity to the direction of movement, boasting linear regressions of up to 0.98 and 0.96 under concave and convex bending, respectively. Elsewhere, Pan's team introduced flexible and stable LED pressure sensor arrays comprised of p-GaN/n-ZnO nanowire heterostructures, utilizing a laser to transfer GaN-based sensing arrays to flexible substrates[24], as shown in Figure 1.7 (c). The constructed pressure sensor exhibits both high resolution and commendable flexibility, and the LED array design facilitates easy measurement of EL emission from various segments to ascertain pressure distribution. Subsequently, the team applied a similar flexible GaN/ZnO heterostructure for UV detection, assembling a self-powered UV sensor (Figure 1.7 (d))[25]. This device features an on/off current ratio of 7.36×10^6 and a UV detection sensitivity of 6.82×10^{13} Jones, coupled with a millisecond response rate.

In recent years, the rapid development of advanced materials such as carbon nanotubes, graphene, and diamond, along with the progressive evolution of microelectromechanical systems (MEMS) and nanoelectromechanical systems (NEMS) technologies, has established a solid foundation for the creation of sensing and detection devices. Among these, diamond is highly regarded as an ideal material for semiconductor sensing and detection due to its exceptional chemical stability, irradiation resistance, and insusceptibility to irradiation interference. There is an escalating utilization of diamond-based sensing and detection devices for various applications, including the detection of gases (CO, NH_3, etc.), particles (α particles, protons, neutrons, etc.), rays (X-rays, γ-rays, etc.), ultraviolet light, magnetic fields, and

more. The continuous advancement in diamond fabrication and processing technology is paving the way for increased commercial application, drawing significant attention towards the prospect of new diamond-based sensors[29, 30].

In the diamond lattice, when a nitrogen atom replaces a carbon atom in a face-centered cubic structure, and a lattice vacancy is present in the immediate vicinity, a fluorescent nitrogen vacancy (NV) color center defect is created[31]. This spatially vector-sensitive center possesses electron spin attributes that impact the fluorescence properties of the NV center, in both the direction of the static magnetic field (aligned with the NV axis) and the direction of the polarized electromagnetic field (perpendicular to the NV axis plane), facilitating effective detection of static, weak magnetic fields at low frequencies[32]. Conversely, diamonds hosting silicon vacancy (SiV) centers serve as exceptional fluorescence emitters for a myriad of biosensing applications. The SiV center, characterized by a symmetrical structure, exhibits energy level transitions relatively uninfluenced by phonons and presents sharp near-infrared optical properties[33]. In recent research, investigators utilized high-power LEDs for the optical excitation of diamond NV centers, constructing a miniaturized magnetic field sensor based on the negatively charged NV center by harnessing its sensitivity to magnetic field intensity (Figure 1.7 (e))[27]. Translating this technology to biological applications, Webb and his team employed diamond quantum sensors to detect in vitro action potentials in live mammalian samples via magnetic fields. As depicted in Figure 1.7 (f), their approach utilized a blue LED as a muscle stimulation source and facilitated continuous sensor measurements even as the specimen remained active, by monitoring

induced fluorescence in the NV center[28].

Diamond displays distinct sensing attributes across an extensive array of research disciplines. Should nanoscale diamond particles, diamond arrays, or diamond films be integrated with monolithically constructed III-nitride optoelectronic devices, it would potentially broaden the sensing spectrum of the optoelectronic chips and enable concurrent detection of multiple parameters. Such a breakthrough necessitates concerted efforts from researchers to integrate the device structure of the diamond-III-nitride optoelectronic chip.

1.2.2 Design and applications of monolithic on-chip integrated GaN-based optoelectronic devices

Given the sensing mechanisms delineated above, there has been a growing interest in chip-scale integrated III-nitride optoelectronics over the past decade. Scholars have made noteworthy strides in applying pure III-nitride chips in realms such as optical communication and heart rate detection.

In a relevant case study focusing on visible light communication, Gao conceived a self-sustaining underwater optical communication system, depicted in Figure 1.8 (a)[26]. This system facilitates underwater wireless power transmission, thus offering a straightforward, cost-effective, and miniaturized communication apparatus suitable for marine communication applications. Delving deeper into the utilization of III-nitride devices for biological applications, Chu's team has trailblazed the integration of a GaN-based monolithic chip with a differential interference contrast (DIC) microscope[34].
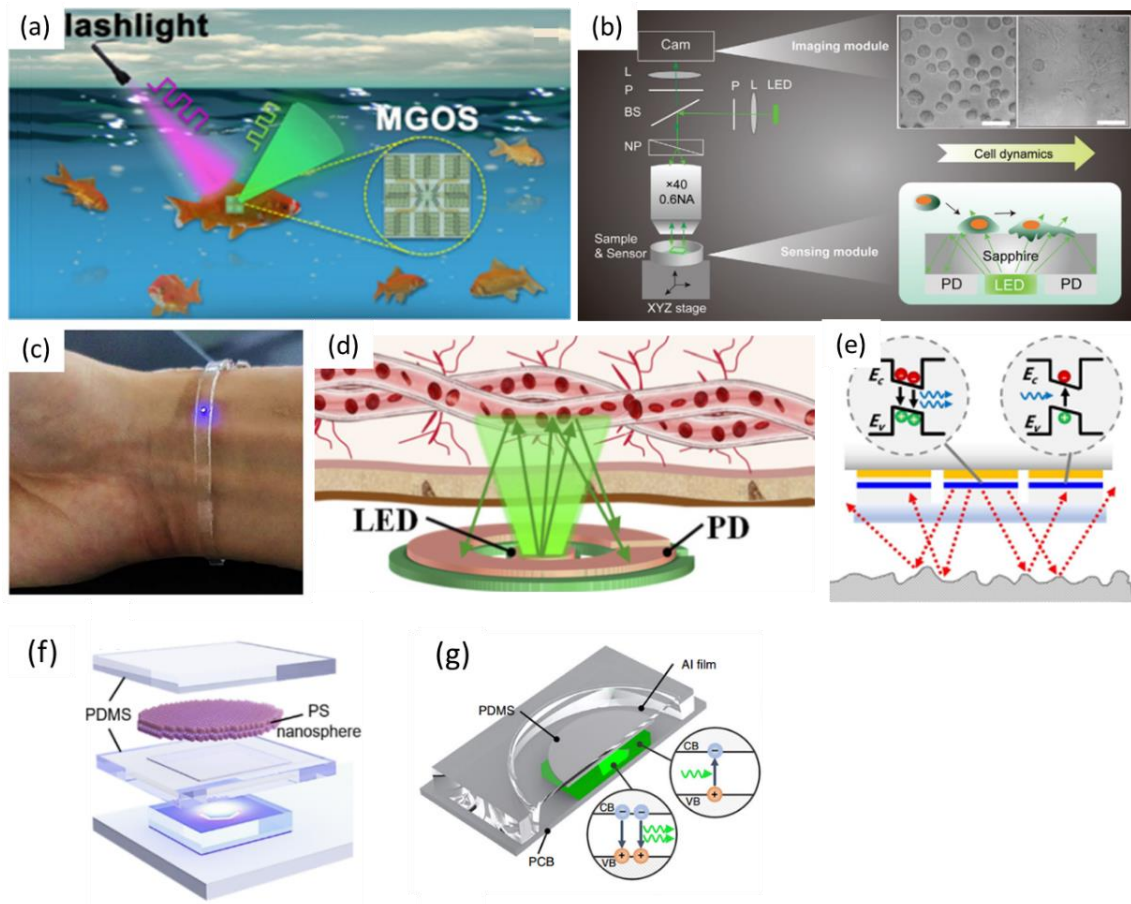
Figure 1.8 (a) A functional block diagram depicting the underwater operability of the monolithic GaN optoelectronic system [26]. (b) Configuration of the optical setup for the monolithic GaN photonic chipscope [34]. (c) A visual representation capturing heart pulse monitoring from the wrist [35]. (d) Exploratory outline of the working principles behind the reflection-type PPG pulse sensor [36]. (e) Conceptual framework describing the GaN LED-PD chip functionality for surface roughness measurements [37]. (f) Structural diagram of the optical pressure sensor layout [38]. (g) Schematic representations delineating the design and functionality of the airflow sensor [39].

This innovative combination facilitates the quantitative and dynamic detection of cell attachment, flattening, spreading, and detachment, all without the need for any

labels. Moreover, as depicted in Figure 1.8 (b), the chip scope holds extensive potential in various applications, including drug screening and cell differentiation studies. Expanding on this potential, Chen developed a photo-plethysmography (PPG) pulse sensor, utilizing a symmetrically integrated LED-PD optoelectronic chip[35]. In this setup, the light signal from the LED is transmitted through the arterial blood flow to the PD, with any alteration in the photocurrent received by the PD serving as a reflection of the heart pulse signal. As demonstrated in Figure 1.8 (c), the pulse sensor employs a flip-chip technique that allows the sapphire surface to make close contact with the skin, thereby enhancing the accuracy of PPG detection. Building on this foundation, Yan and his team subsequently constructed a comprehensive PPG pulse sensing system[36]. The research introduced a processing circuit, signal analysis and display unit, enhanced the LED-PD structure with an inner circle and outer ring, and discussed the optimal wavelength for the sensor, laying the groundwork for a wearable PPG pulse sensor. The operational principle of the reflection-type PPG pulse sensor is depicted in Figure 1.8 (d).

Chen et al. developed a monolithically integrated InGaN/GaN optoelectronic chip for refractive index sensing in solutions, leveraging the alteration of the critical angle and Fresnel reflection at the sapphire/solution interface[40]. The authors credit the expansive refractive index sensing range (1.3325-1.5148 RIU) and high resolution (6.4×10^{-6} RIU) to the implementation of a Distributed Bragg Reflector (DBR), thus laying the foundation for the development of a chip-scale refractometer. Continuous refractive index monitoring carries significant industrial relevance. Drawing from

additional research, three GaN LED-PD devices, functioning at distinct wavelengths within the blue-green-visible spectrum, were devised for in-situ monitoring of resin curing processes[41]. The GaN devices manage to capture the minute refractive index alterations occurring during resin curing, and their compact dimensions of 1.1 x 1.1 x 0.21 mm^3 extend their potential for various industrial applications. Evaluating sugar concentration is crucial in food and medical fields, yet conventional methods of determining glucose and fructose solution concentrations are often laborious and expensive. Investigating the application of III-Nitride microchips for sugar concentration detection, Chen's research points out the correlation between the refractive index of glucose and fructose solutions and their respective concentrations[42]. Their work demonstrates that the GaN optoelectronic chip offers swift response times within a sub-second range and accurate concentration sensing from 0-50%, which significantly enhances the efficiency of sugar concentration detection. Integrated III-nitride optoelectronic devices also hold potential for industrial applications such as the detection of trace amounts of water in alcohol. An et al. introduced a sensor that leverages the difference in refractive index at the interface of sapphire and ethanol to swiftly identify the water content within alcohol[43]. As alluded to earlier, the principle of reflection has been implemented in the context of proximity sensors[44]. In an exploration of different reflectivity films and their impact on photocurrent, the team found that the chip's swift response enabled the proximity sensor to accurately detect the vibration frequency of objects located within sub-centimeter distances, all within a few microseconds. Considering the potential damage risks

associated with contact surface roughness inspection, Yin and his team proposed a circular-ring GaN optoelectronic device for non-contact surface roughness inspection[37]. In this setup, a circular PD is encircled by an LED ring, enlarging the sensing area and enhancing roughness detection accuracy (see Figure 1.8 (e)). This optoelectronic sensor amalgamates the benefits of a small form factor, high precision, cost-effectiveness, and non-destructive detection, offering a dependable monitoring solution for precision machining.

In an innovative application, Jing incorporated self-assembled (PS) photonic crystals into flexible (PDMS) as the mechanosensory component, depicted in Figure 1.8 (f). In conjunction with an optoelectronic chip, this setup effectively utilizes the mechanism of angle-dependent reflective characteristics to transduce pressure into an optical signal, subsequently converted into a photocurrent[38]. This strategy offers a more compact, faster-responding, and more reproducible alternative to traditional mechanical sensors. A similar opal structure can also serve in humidity detection. Luo devised a method wherein a silica opal film covers the GaN chip surface, translating changes in relative humidity (RH) quantitatively via the film's reflectivity sensitivity to humidity over a linear sensing range from 10%-90%[45]. As depicted in Figure 1.8 (g), when a PDMS cavity structure couples with highly reflective aluminum foil, the PDMS film's interaction with the airflow alters the distance between the aluminum foil and the sapphire surface, resulting in a change in the photocurrent. This fluctuation can be monitored to measure wind speed, with the airflow sensor detecting wind speeds up to 53.5 m s^{-1} with a sensitivity of 0.2686 μA/ (m·s^{-1})[39]. When a specifically patterned

PDMS interfaces with the sapphire surface of the optoelectronic device, the photocurrent varies in response to external pressure. Building on this, An et al. designed a dome-shaped PDMS combined with GaN optoelectronic devices, capable of detecting a wide sensing range from 0-50 kPa, sensitive enough to recognize human breathing, speech, and other specific movements[46]. These contributions provide experimental groundwork for the development of wearable smart electronic devices.

1.3 Research Contributions and Organization

This thesis focuses on monolithic integrated flip-chip GaN LED-PD devices. The main research is on the working principle of monolithic flip-chip GaN LED-PD, the design and assembly of three patterns of LED-PD devices, and their application in the detection of various liquid properties.

In this chapter, the research background of GaN-based LEDs and PDs is introduced. The working principles of LEDs and PDs are presented, including the light emitting principle, the light sensing principle, and the optical coupling mechanism. The need to integrate both LED and PD on a single device is suggested. At the same time, summarize the development and current status of GaN-based monolithic integrated devices, and discuss their applications in sensors. According to the current research status of GaN-based optoelectronic integrated devices, put forward the research purpose of this thesis.

Chapter 2 describes the structure of flip-chip GaN LED-PD devices, the design of the mask, and the evaluation method of the optical and electronic characteristics. The fabrication process of flip-chip devices is introduced, including the main processes of

epitaxy and lithography. The printed circuit board (PCB) design and solder selection are carried out according to the device structure design to complete the package, and the optoelectronic properties of monolithic flip-chips are discussed.

Chapter 3 proposes a new method using micro-GaN chips applied to droplet and viscosity sensing. Two types of LED-PD chips which homogeneously integrated on a sapphire substrate are designed for droplet sensing and viscosity measurement applications, respectively. Droplet sensing mainly exploits the different effects of air and droplets on the total reflection interface, while viscosity testing is based on the length of time that different droplets traverse the chip to determine viscosity.

Chapter 4 reports a novel GaN-based microchip for pH detection. A porous membrane anchored with an acid-base indicator was combined with the GaN chip to read out the sample pH by photocurrent using the reflectance spectral change of the acid-base indicator in the wavelength interval of the chip operating wavelengths. In addition, and the repeatability test and the ionic interference test proved that the device has good stability.

In Chapter 5, an optoelectronic nose based on a GaN monolithic integrated chip is applied in organic identification. The optoelectronic nose uses a thin film of PDMS-PS photonic crystals as the sensing medium. By exploiting the property that photonic crystals can selectively reflect light of specific wavelengths, the amount of light received by the PD is varied, and then organic gas is recognized. Theoretical calculations and simulations confirm that the reflection spectrum of the photonic crystal partially overlaps with the working wavelength interval of the chip. After testing, the

optoelectronic nose can distinguish 7 types of gases volatilized by organic liquids.

Chapter 6 summarizes the research content of this thesis and suggests feasible future research directions.

Chapter 2 Fabrication and Characterization of GaN-based monolithic integrated flip-chip optoelectronic devices

2.1 Design of GaN-based monolithic integrated flip-chip optoelectronic devices

2.1.1 Structure of GaN-based monolithic integrated flip-chip optoelectronic devices

Since the structure of a GaN-based optoelectronic device is related to its packaging method, we will briefly introduce the chip packaging formats before delving into the chip structure.

Two prevalent GaN chip structures are observed, namely the wire-bonding structure (conventional structure) and the flip-chip structure, as depicted in Figure 2.1. The GaN chip of wire-bonding structure is illustrated in Figure 2.1(a). In this structure, layers are stacked from bottom to top in the following order: substrate, an undoped GaN (u-GaN) buffer layer, n-type GaN (n-GaN), the MQWs, p-type GaN (p-GaN), Indium Tin Oxide (ITO), and lastly, the electrodes and pads. The electrodes of wire-bonded chip faces upwards and are electrically connected to the metal base, while the substrate faces downwards and is attached with a bonding material. In this configuration, both electrodes are placed on the light-emitting surface of the chip, which tends to absorb part of light by the electrodes and welding point, thereby diminishing light efficiency.
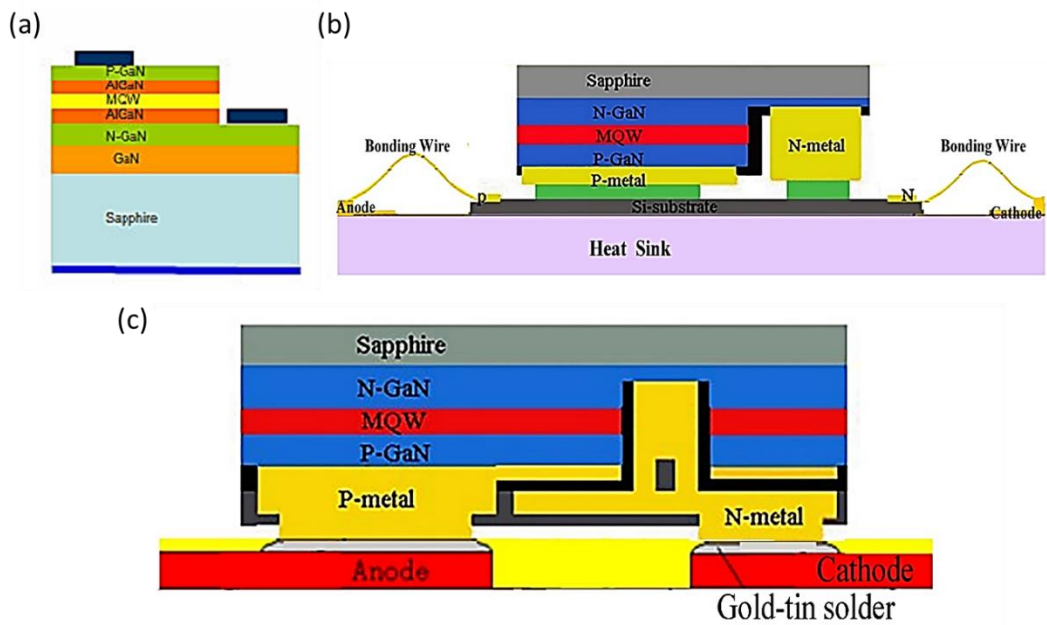
Figure 2.1 Schematic diagram of (a) wire-bonding[47], (b) wired flip-chip and (c)

wireless flip-chip package structure[48].

Additionally, due to the low level conductivity of the p-GaN layer, a current

spreading layer is often deposited on its surface to improve the current spread in the p-

GaN layer. To minimize light absorption, the thickness of this diffusion layer is reduced

to several hundred nanometers. However, this thickness reduction, in turn, can

compromise the current uniformity across the p-GaN layer surface and the reliability of

the diffusion current. Hence, this design significantly restricts the operating power of

GaN-based devices.

The alternative is the wired flip-chip GaN-based device, depicted in Figure 2-1(b).

The structure of a GaN-based flip-chip, from bottom to top, consists of a substrate, a u-

GaN buffer layer an n-GaN layer, MWQs, a p-GaN layer, a p- and n-metal layer, a

passivation layer, and p- and n-electrodes.

A flip-chip GaN chip positions the substrate upwards, with the electrodes facing

downwards. The electrodes connect electrically to the PCB through metal bumps, thus reducing the number of wiring process steps. In this configuration, light is emitted from the substrate, bypassing the current spreading layer with light absorption properties. As the light does not emanate from the current spreading layer, the opaque current spreading layer can be made thicker, thereby augmenting the current density of GaN chips. Moreover, the light emitted from the active layer can be directed downwards by the p-electrode, enhancing the light output efficiency. Such design also allows the heat generated by the p-n junction to transfer directly to the higher thermal conductivity silicon substrate via the metal bumps, circumventing the heat dissipation issues attributed to the low thermal conductivity of the holder seen in conventional wire-bonding structure. The flip-chip structure features many advantages. The use of the bump structure significantly reduces interconnection length, resistance, and inductance, dramatically improving the package electrical performance. Furthermore, the heat generated within the chip is directly transferred to the package substrate via the solder bumps.

Nonetheless, a wired flip-chip package structure is bonded to a Si substrate using metal bumps, followed by drawing positive and negative terminals on the Si substrate and then packaging with other accessories. The wired flip-chip structure requires the integration of other heat sink materials, such as aluminum (Al) substrates, to effectively decrease thermal resistance. However, due to the considerable size of the Si substrate, and thermal conductivity is only 1/3 to 1/2 of that of metals like Al or copper (Cu), heat dissipation is less efficient. At the same time, the addition of heat sink material also

correspondingly increases the size of the device, which is not conducive to the application of the device. Additionally, the chip electrodes must be bonded to the Si substrate with metal bumps, a process that is complex and influenced by multiple factors, thereby potentially complexing the manufacturing process and diminishing the yield of the GaN devices.

In an effort to mitigate the aforementioned issues, a novel package structure of GaN-based LED chip, the wireless flip-chip structure, has been devised. The structure of this refined GaN-based flip-chip is illustrated in Figure 2-1(c). In this setup, both the positive and negative electrodes of the GaN flip-chip reside on the reflective surface of substrate and occupy the same horizontal plane. This arrangement notably augments the light output area compared to the wire-bonding GaN chip and vertical LED chip designs.

Furthermore, the wireless flip-chip structure does not require any gold or silver wire for electrical connections between the electrodes, as the positive and negative electrodes are directly soldered onto the PCB. This eradicates the need for electrode leads, thereby enhancing reliability. Importantly, there is also no need to create metal bumps between the GaN chip electrodes for bonding the electrodes to the Si substrate, improving the robustness of GaN-based devices. Light from the active area of the GaN flip-chip is extracted through the transparent sapphire substrate, thus preventing light absorption by the current spreading layer. The downward-facing light is reflected upwards by the reflective layer (DBR or silver mirror), substantially boosting light efficiency. Concurrently, heat is effectively conducted to the PCB via the electrodes,

ensuring excellent thermal conductivity.

While the wire-bonded photodetection system exhibits high sensitivity and optical coupling efficiency, it also encounters thermal effects and stray light issues. In contrast, the flip-chip package light detection system demonstrates superior optical coupling efficiency and diminished thermal effects, though care must be taken to protect the sensitive surface of devices. In pursuit of optimal liquid detection effect, this research employs a flip-chip LED structure.

The system has been designed with monolithic integration to reduce the device size and complexity, while also minimizing signal loss and noise. Such design eliminates the need for external optics, further simplifying the system design and fabrication process.

Among prevalent substrate materials of GaN-based optoelectronic devices, sapphire proves more favorable for light emission compared to silicon and silicon carbide, attributed to its high mechanical strength, robust chemical stability, and adaptability to high-temperature environments. Furthermore, the feature of easy cleanliness further bolsters the utility of sapphire substrates. However, due to a reflection coefficient greater than air, sapphire substrates experience Fresnel reflection when light is emitted, and the majority of light generated in the active layer gets absorbed within the LED and transforms into heat, a phenomenon known as total internal reflection (TIR). This issue can be mitigated by patterning the sapphire surface. Additionally, as sapphire is hydrophobic, it caters well to the requirements of liquid detection[49].

Sapphire is composed of aluminum oxide (Al_2O_3), which is made up of three oxygen atoms and two Al atoms bonded in a covalent pattern. The crystal structure of sapphire is a hexagonal lattice structure, which often used in a-plane (1120) (non-polar), c-plane (0001) (polar), m-plane (1100) (semi-polar) and r-plane (1012) (semi-polar) facets. Threaded dislocations (TDs) on the a-plane, r-plane, and m-plane of sapphire lead to a high count of dislocations, which often penetrate the surface and create a substantial distribution of pits and defective trapping carriers, substantially reducing the luminous efficiency[50]. Conversely, the epitaxy technology on the c-plane of sapphire is mature, stable, and cost-effective, making it a favorable choice.
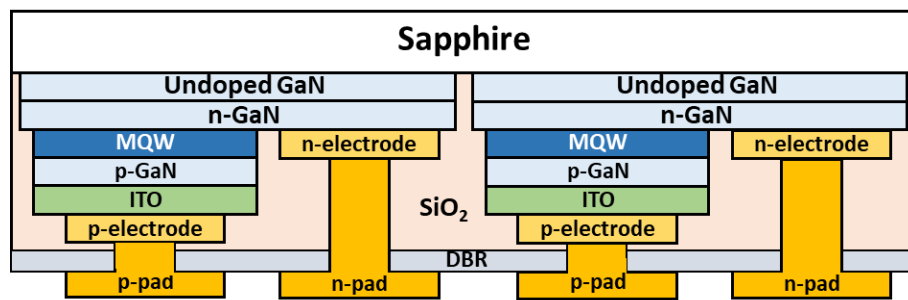
Figure 2.2 Structure of the GaN-based monolithic flip-chip LED-PD device.

Our design employs a wireless flip-chip package structure, integrating GaN-based LED and PD onto the same c-plane sapphire substrate. This arrangement, as depicted in the Figure 2.2, comprises nine layers: a sapphire substrate, an undoped GaN buffer layer, n-GaN, InGaN/GaN MQWs, p-GaN, a current spreading layer, internal metal electrodes, a reflective layer, and pads (p-pad and n-pad).

Specifically, the c-plane sapphire substrate is typically prepared by thin-film growth techniques and etched into a specific shape, so called patterned sapphire substrates (PSS), which minimized the dislocation density of GaN crystals and

providing a stable foundation with commendable thermal and mechanical stability. Additionally, the PSS offers excellent optical transmission, allowing luminescence to radiate outward from the bottom. Then, an undoped GaN buffer layer is developed on the sapphire surface, followed by subsequent layering of n-GaN, GaN/InGaN MQWs and p-GaN atop the u-GaN layer.

The Si-doped n-GaN layer serves as an n-type doped layer, providing electron channels and regions for electron injection, while the Mg-doped p-GaN layer functions as a p-type doped layer, offering hole channels and areas for hole injection. The union of n-GaN and p-GaN results in a p-n junction. The InGaN/GaN MQWs layer as the active layer, where luminescence occurs, forms the pivotal component of the LED. With a vertical energy gap distribution and high carrier concentration, the InGaN quantum well improves the efficiency and brightness of LED. The TCL locates on above of the p-GaN layer, full named as transparent conductive layer, composed of ITO, and helps evenly distribute current across the LED, averting central overheating. The conductive circuit (CKT), facilitates the injection of electrons and holes into the MQWs layer by connecting the p-GaN and n-GaN layers. The reflective layer is DBR, which aids in reflecting the emitted light from the MQWs back towards the sapphire, thereby enhancing light output efficiency. Lastly, the p-pad and n-pad deposit onto the CKT layer and serve as connectors for external circuits to power the LEDs.

2.1.2 Photomask design of GaN-based monolithic integrated flip-chip optoelectronic devices
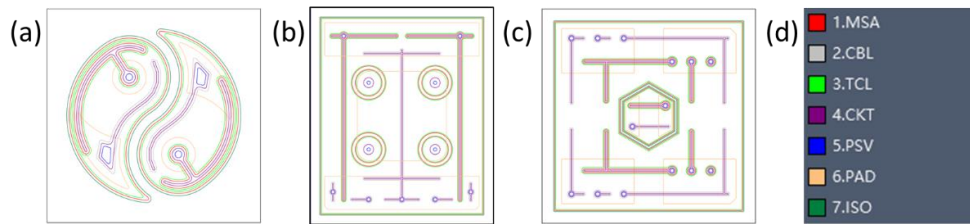
Figure 2.3 Photomask design of monolithic integrated flip-chip GaN-based

optoelectronic devices for (a) droplet microsensor, (b) pH sensor, and (c) organic

liquid optoelectronic nose. (d) The corresponding color of each photomask.

In line with the structural analysis of the wireless flip-chip GaN-based

optoelectronic devices, the overarching mask design is depicted in Figure 2.3, with

different color lines corresponding to the hierarchy. The device comprises seven mask

layers, including the mesa (MSA), CBL, ISO, ITO, CKT, PSV, and PAD layers. Each

of these layers has specific functions, with the MSA layer primarily used to etch and

expose n-GaN to form n-finger. The CBL is current blocking layer, which composed by

passivation material SiO_2 and deposited on p-GaN to prevent the vertical expansion of

current. ISO corresponds to insulation layer to realize the electrical insulation of a

single chip. Since the composition of the TCL layer described in the previous section is

ITO, the ITO layer is the equivalent of the TCL, i.e., the transparent conductive layer.

The ITO semiconductor is deposited on the SiO_2 passivation material through the ITO

photomask to help the current of p-GaN layer expand uniformly laterally. Since the

passivation layer has the same shape as the reflective layer, the PSV corresponds to

both the passivation layer and the DBR layer, which means that SiO_2 is deposited on

the part beyond the CKT to protect the fingers. And then, the silicon dioxide (SiO_2)/

titanium dioxide (TiO_2) multilayer film structure is deposited on top of the passivation

layer to form the DBR to realize the reflection of the emitted light. Finally, the PAD layer corresponding to p-pads and n-pads is deposited outside the CKT for electrical interconnection.

Strict adherence to design rules is essential when considering the layering of photomasks during the manufacturing process. While the PAD pitch is typically 150 μm, it can go down to 50 μm for LEDs. In monolithically integrated flip-chip GaN LED-PD devices, the LEDs and PDs, fabricated on the same GaN wafer, must function independently. Therefore, it is crucial to determine the space between the LEDs and PDs using an ISO layer mask that is deeply etched into the sapphire layer, to ensure complete separation of the n-GaN layers for electrical insulation.

In this study, we present three different monolithic integrated flip-chip LED-PD devices. To analyze the effect of GaN LED-PD chip size on optoelectronic characteristics while considering the micro and nano-manufacture process.

Specifically, the LED and PD of the chip for the droplet microsensor are presented in a centrosymmetric pattern, as shown in Figure 2.3(a). The chip size is $630 \times 630\ \mu m^2$, and the LED and PD cover the same surface area. The size of the optoelectronic chip for the pH sensor is $1300 \times 1100\ \mu m^2$, as shown in Figure 2.3(b). In the design of this chip, the LED is divided into four circular light emitting regions evenly distributed in the center of the chip, with the PD portion on the outside. The LED and PD share the same n-electrode, so the PAD layer consists of only the n-pad, the LED p-pad and the PD p-pad. The chip displayed in Figure 2.3(c) is employed for the organic liquid optoelectronic nose. Such a design sets the ortho-hexagonal LED in the center of the

chip, surrounded by the area of the PD, with an overall size of 1000×1000 μm^2.

2.2 Manufacturing process of GaN-based monolithic integrated flip-chip optoelectronic devices

The manufacturing of GaN-based devices comprises two primary stages: epitaxial growth and the processing of chip. During the epitaxial growth phase, the GaN epitaxial wafers are cultivated on the selected substrate. Subsequently, in the processing of chip, the GaN chip structure is created on the epitaxial wafer using electronic manufacturing methods such as vapor deposition, photolithography, and etching. The key manufacturing processes include the cultivation of epitaxial wafers and the vapor deposition and etching of each structural layer, which necessitate the use of various technologies and equipment, including metal-organic chemical vapor deposition equipment, plasma-enhanced chemical vapor deposition machines, inductively coupled plasma etching machines, and OPTOTECH OTFC-1300 optical coating machines. The primary role of these machines is to control the thickness and quality of the layers during the manufacturing process and to ensure the accurate alignment of each layer. Additionally, it is crucial to pay attention to the purity of the materials and the content of impurities, as they can significantly influence the quality and performance of the LED chip. It is worth noting that the manufacturing process of monolithic flip-chip GaN-based LED-PD devices represents a unique manufacturing technology, with a process that diverges from traditional manufacture of LED chips.
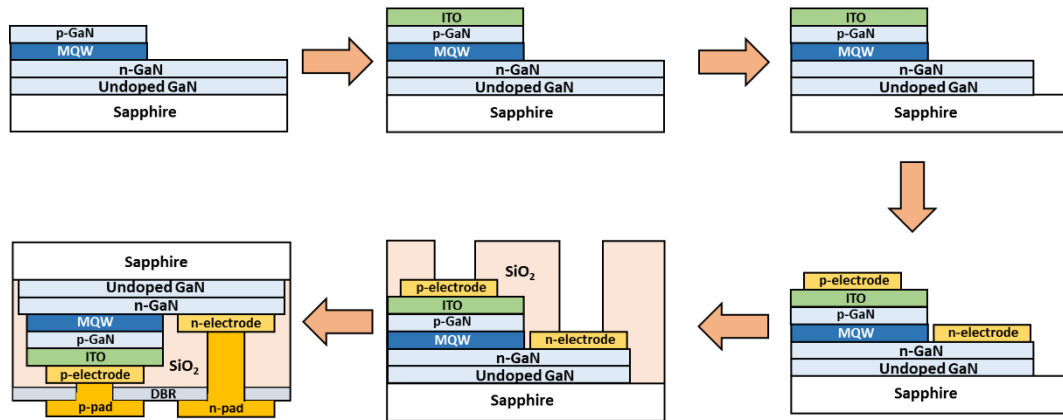
Figure 2.4 The fabrication process of flip-chip LED.

The following steps are the manufacturing processes of monolithic integrated LEDs and PDs based on mature semiconductor processes, as shown in Figure 2.4.

2.2.1. GaN epitaxial layer growth

Initially, an epitaxial structure containing u-GaN, n-GaN, GaN/InGaN MQWs and p-GaN are grown on a 4-inch c-plane sapphire substrate using metal-organic chemical vapor deposition (MOCVD).

Ensuring the quality of epitaxial growth requires thorough cleaning and high-temperature treatment for the sapphire substrate. The main objectives are to eliminate residual impurities on the surface and enhance the smoothness of sapphire. Furthermore, it is vital to cultivate a u-GaN single crystal layer on the substrate to act as a buffer layer, remitting the issue of lattice mismatch between sapphire and GaN. The buffer layer typically measures about 30 nm in thickness.

Once the buffer layer is prepared, the n-GaN layer with a thickness of about 3 μm is grown onto the u-GaN layer. The growth is achieved by injecting trimethyl gallium (TMGa) and silicon tetra hydroxide (SiH$_4$) gas into the reaction chamber under high-

pressure and low-temperature conditions. TMGa, a metal-organic compound and gallium (Ga) atoms precursor is introduced alongside SiH_4, a gaseous silane and Si atoms precursor. Throughout the growth process, Si atoms, possessing one additional valence electron than Ga atoms, could replace Ga atoms, which leads to the grown epitaxial layer predominantly consisting of electrons, i.e., n-GaN.

MQWs structure is grown for 3-15 cycles in a N_2-protected atmosphere at temperatures ranging from 720 to 920 °C and pressures between 26.66 to 79.98 kPa. Initially, shallow quantum wells with a thickness of 3-5 nm are grown at low temperatures. Next, the temperature is controlled between 720-820 °C, and the pressure is adjusted to 26.66-66.65 kPa to form low-temperature MQWs layers. In this process, the composition of indium (In) atoms needs to be consistent. The thickness of the MQWs light-emitting structure ranges from 2 to 5 nm. By doping with In atoms, the bandgap could be significantly reduced, facilitating easier electron excitation and substantially enhancing the luminescence efficiency of the active region.

Lastly, p-GaN is grown on the MQWs layer, with the temperature and pressure regulated at high and low levels, respectively. By introducing cyclopentadienyl magnesium (Cp_2Mg) into the reaction chamber, Ga atoms can be replaced by Mg atoms, leading to the majority of the carriers becoming holes, and ultimately forming p-GaN with a thickness of approximately 0.5 μm.

2.2.2 The processing of GaN chip

The epitaxial wafers are cleaned with the acid solution, setting the stage for the chip micro- and nano-processing. The aqua regia effectively removes residual metal

oxides and metal particles, as well as other contaminants from the epitaxial wafer. At the same time, aqua regia does not corrode GaN or sapphire substrates below 24 ℃. Therefore, aqua regia is generally used to remove metals or metal oxides from the epitaxial wafer surface.

To achieve the electrical isolation of the devices, a thin film structure is formed by initially depositing the material required for the circuit on the wafer, using photolithography technology to define the area. The film is then coated with a positive photoresist, which is removed post-exposure development.

The MESA pattern on the mask is transferred to the wafer by lithography and etched by inductively coupled plasma (ICP) to a depth of 1.2 μm to expose the n-GaN. The remaining photoresist is removed. The 10-μm-wide GaN interval between the LED and PD is entirely removed via photolithography and ICP etching.

Then, a 190 nm thick SiO_2 layer is deposited using plasma-enhanced chemical vapor deposition (PECVD) and then photolithographed to create a current blocking layer pattern.

The reactive plasma deposition process is performed on the wafer to form the TCL. The sealed cavity is filled with argon (Ar) and oxygen (O_2) under high voltage. Ar is ionized to form Ar^+ ions that bombard the target, facilitating the sputtering of ITO onto the p-GaN layer at a specific rate to form a continuous 120 nm thick ITO film. The ITO layer pattern is then etched using the same photolithography method.

Additionally, the CKT layer for inner metal electrodes, composed of Chromium (Cr), Platinum (Pt), and Gold (Au) with respective thicknesses of 50 nm, 50 nm, and

2.1 μm, are fabricated on n-GaN and ITO layer. The p- and n-electrodes are produced through electron-beam evaporation and photolithography.

Later, a 360 nm thick SiO_2 isolation layer is deposited using the PECVD method. After 23 pairs of TiO_2/SiO_2 films are formed on the ISO layer as DBR reflectors using optical thin-film coater, the p- and n-electrodes are exposed by photolithography and ICP. The n- and p-pads are formed by depositing 1.65 μm of Chromium (Cr)/Al/ Titanium (Ti)/ Platinum (Pt)/gold (Au) mixed metals on the exposed surface of electrodes using the electron-beams.

Ultimately, the sapphire is mechanically ground and polished. The fabricated wafer is laser diced into chips of the specific size.

2.3 Packaging of GaN-based monolithic integrated flip-chip optoelectronic devices

Monolithic flip-chip GaN LED-PD devices pose significant packaging challenges due to their minuscule dimensions and high integration density. To fulfil high performance and longevity demands, a substrate that pairs well with the flip-chip GaN LED-PD device is required for packaging. Such substrates must meet physical size compatibility requirements, in addition to exhibiting superior electrical, thermal, and mechanical properties.

It is also crucial to ensure that the optoelectronic characteristics of the device remain unaffected during the packaging process. Electrical interconnection represents a vital concern in the packaging design process. To ensure the reliability and stability of GaN devices, it is necessary to link the flip-chip GaN LED-PD devices with the

electronic components on the package substrate via a suitable electrical interconnection. Moreover, protective support is another vital aspect of packaging. Through the careful selection and design of packaging material, the mechanical stability and impact resistance of devices can be enhanced.

Heat dissipation also deserves careful consideration during the packaging process. Flip-chip GaN LED-PD devices generate substantial heat during operation. If this heat is not promptly dissipated, the device's temperature will rise, leading to a reduction in performance and lifespan, and potentially resulting in device failure. Therefore, for a single flip-chip GaN LED-PD device packaging design, it is necessary to consider electrical interconnection, protective support, and heat dissipation. By selecting suitable packaging materials and design methods, it is possible to fulfil the requirements of high performance and longevity while ensuring the preservation of optoelectronic performance.

The substrate materials commonly used are Al substrates and ceramic substrates. Flip-chip packaging typically utilizes the reflow soldering method, which necessitates completion under high-temperature conditions. As such, the selection of substrate materials with high thermal conductivity and mechanical strength can enhance both the reflow efficacy of the packaging process and the heat dissipation efficiency during chip operation.

Al substrates, in particular, are widely utilized across various fields due to their excellent characteristics. These include outstanding thermal conductivity, robust mechanical strength, stable durability, and affordable costs. Additionally, they are easy

to process and are supported by well-established manufacturing technology. The preparation and processing procedure for the Al substrate involves depositing a layer of SiO_2 onto a 1.6 mm thick Al substrate as an insulating layer. A 35 μm thick Cu layer is then laid down in a specific area of the silica insulating layer to serve as a connecting layer. Lastly, Au is deposited on the copper to form pads for achieving external interconnections. The line width and line pitch of the Al substrate are set at 150 μm.

The substrate used in this study, as depicted in Figure 2.5. The LED and PD pads are located on the top of the substrate, while the test connector pads are positioned at the bottom. The dark blue color on the substrate represents the silica insulating layer on the Al substrate, with the wires on top made of metallic copper. This configuration facilitates the electrical signal interconnection between the chip and the connector. The light blue portion on the surface is a white ink layer, acting as the solder resist. Upon finalizing the device packaging, the connector interconnects with the power supply and current detector through a soft line, thereby completing the input and output of electrical signals.

The packaging reliability of monolithic flip-chip GaN LED-PD devices is a direct determinant of device performance and lifespan. To ensure high-quality packaging, we opted to use SD-588T lead-free solder paste for reflow soldering. This paste has a particle size ranging from 1 to 10 μm and a melting point of 217 °C.
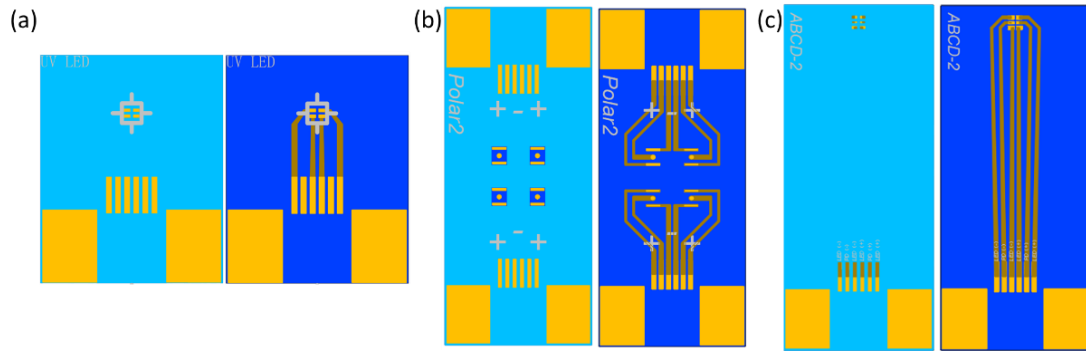
Figure 2.5 PCB design of pads and inner layer alignment for (a) droplet microsensor,

(b) pH sensor, and (c) organic liquid optoelectronic nose.

During the packaging process, the first step involves applying an appropriate amount of solder paste to the PCB pad. Subsequently, the rear of the pads chip are aligned with the solder paste. The device is then placed on a heating table set at 250 ℃ and left for approximately one minute until the bond is cured.

The reflow temperature must be meticulously controlled. This is to ensure that when the bottom side undergoes reflow, the solder paste on the front side doesn't become compromised by secondary reflow. Such control is critical in maintaining packaging quality and device performance.

2.4 Characterization of optical and electrical properties of GaN-based monolithic integrated flip-chip optoelectronic devices

Following the packaging steps, it delve into the instrumentation used for the electrical and optical characterizations of the GaN chips and the corresponding experimental instruments.

The electrical properties of the LED are commonly evaluated using I-V tests.

Analysis of the resulting I-V characteristic curve provides insight into the turn-on voltage, resistance, and voltage at a specific injection current of LED. The turn-on voltage is determined by the x-axis coordinates corresponding to the inflection points between the forward dead zone and the working zone, with different colors of LEDs exhibiting varying turn-on voltages. Resistance is calculated from the inverse slope of the line in the working zone, and its magnitude influences both power and heat generation in the LED, thereby affecting overall performance. The I-V characteristics of the LED are measured using a sourcemeter (KEITHLEY 2450), capable of resolving current down to 50pA.

The optical performance of LED is commonly evaluated using tests such as LED output power at varying injection currents, LED luminescence spectra at specific injection currents, and LED peak luminescence wavelength at specific injection currents. In this study, LED output power is measured in terms of irradiance, which represents the total electromagnetic energy emitted per unit area per unit time and signifies performance of the device. Theoretically, a well-performing LED exhibits a linear correlation between irradiance and working current, with luminous flux increasing as current increases. The luminous intensity or output power of the LED varies with wavelength, and when plotted as a distribution curve, it is known as the luminous spectrum or spectral distribution curve. This curve is determined by factors such as the type of compound semiconductor used in preparation, the nature and structure of the p-n junction (e.g., epitaxial layer thickness, doping impurities), and is not influenced by device geometry or packaging methods. Regardless of the material

used to construct an LED, its light-emitting spectrum exhibits a relative light intensity at its strongest point (maximum light output), corresponding to a specific wavelength known as the peak wavelength. Monochromatic LED have a peak wavelength that should ideally remain stable, although slight red or blue shifts may occur in special cases. The above optical characterizations are all measured by the combination of a spectrometer (OHSP-350C) and an integrating sphere. By driving the LED with a current ranging from 1-10 mA and placing the device inside the integrating sphere, we could measure the emitted spectrum response and output power of the LED.

The photoconversion performance of PD is evaluated using data such as I-V characteristic of the PD, photocurrent response at a specific LED injection current, and transient response. The I-V curve of a PD is measured using the 2450 sourcemeter. After connecting the PD to the sourcemeter, the PD is subjected to a sweeping voltage from -3 V to 3 V in the absence of LED illumination. The dark current of the PD could be observed a stable and smooth line in the -3 V to 0 V region, indicating that the PD operates stably in the -3 V to 0 V region. To evaluate the photoconversion performance of PD, a power supply (KEITHLEY 2230) is connected to the LED, which is then supplied with an injection current to emit light. A significant difference between the photocurrent and dark current when an injection current of 1-10mA is applied to an LED indicates good photodetection performance by the PD. As the luminous intensity of a well-performing LED device is proportional to its injection current, a linear relationship between the PD photocurrent and the LED injection current demonstrates that the photocurrent exhibits a good linear relationship with the amount of incident

light.

The transient response time of a PD characterizes how quickly it can track changes in external light quantity and is determined by factors such as carrier lifetime, device structure, and circuit impedance. From a testing perspective, transient response is the delay between when the LED is turned on or off and when the PD responds. PD transient response time is divided into rise time (t_{10}) and fall time (t_{90}). Rise time (t_{10}) represents the time it takes for luminous brightness to increase from 10% to 90% of its normal value when the LED is turned on. Fall time (t_{90}) represents the time it takes for luminous brightness to decrease from 90% to 10% of its normal value when the LED is turned off. A well-performing PD should have as short a response time as possible to meet instantaneous sensing requirements.

Chapter 3 GaN-based optoelectronic devices for droplet sensing

Droplet sensors play an important role in various fields such as environmental protection, food industry, and medical testing. With the increasing demand for portable devices in practical applications, in-depth research on achieving miniaturization and low-power droplet sensors has been conducted. In this work, we adopt an optoelectronic approach to develop a GaN-based integrated device for droplet flow sensing.

3.1 Introduction

Liquids represent one of the fundamental states of matter and hold significant research importance across fields such as environmental protection [51], the food industry [52], manufacturing processes [53], and so on. Droplet sensors have emerged as crucial tools for monitoring liquid droplets, enabling the acquisition of physical and chemical parameters related to the tested liquids. This facilitates both qualitative identification and quantitative measurement [54]. Driven by advances in science and technology, diverse methodologies have been explored for droplet sensing. Two primary categories have emerged: electrical methods[55] and optical methods[56]. Optical methods permit direct interaction with the liquid, leveraging low-power light sources [57]. However, optical signals are prone to interference from non-specific liquid properties [58]. On the other hand, electrical methods offer stable signals but often lack direct liquid contact [59], leading to reduced sensitivity and necessitating additional power sources [60]. Integrating the strengths of both approaches, this

research endeavors to construct a compact, precise, and energy-efficient liquid sensor using optoelectronic principles.

In the context of optoelectronic sensing, external components are often deemed undesirable [61]. Consequently, on-chip integration has gained prominence for its compactness, reduced power consumption, and enhanced robustness. This study leverages on-chip integration using GaN devices, yielding advantages such as a smaller form factor and increased durability [62]. Compact monolithic integration, facilitated by GaN devices, yields several advantages including reduced size, lower energy consumption, and heightened stability durability[40]. This study centers on the development of a GaN-based chip incorporating a hydrophobic PDMS layer for droplet flow detecting. Through a thorough investigation into device properties and operational mechanisms, the sensing capacity of the proposed droplet sensor is substantiated.

3.2 Fabrication and working principle of droplet sensor
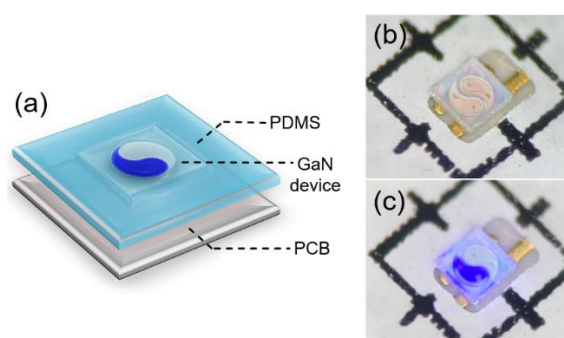
Figure 3.1 The diagram (a) presents the schematic layout of the advanced droplet sensor proposed in this study. The optical images showcase the GaN optoparis (b) before and (c) after the operational phase.

Figure 3.1(a) delineates the components of the droplet microsensor, encompassing a GaN device, a PCB, and a water-resistant PDMS layer enveloping the GaN device. Figures 3.1(b) and 1(c) offer microphotographs of the packaged GaN device, revealing its intricate structure and dimensions. Notably, the device integrates LED and PD functionalities, divided by the light-emitting and non-luminescent areas, respectively. The PDMS gel undergoes a curing process, forming a protective layer around the device.
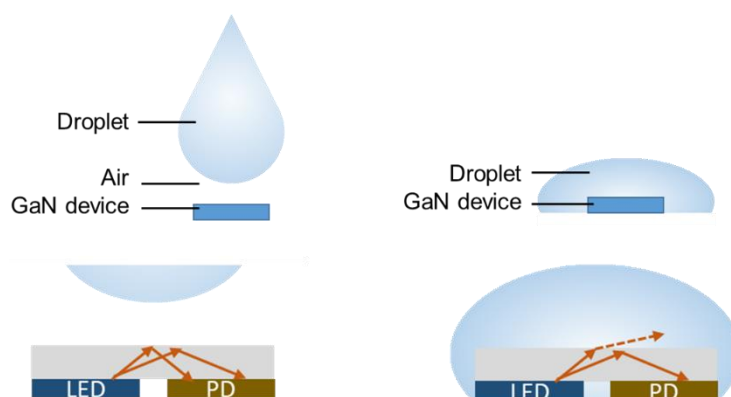
Figure 3.2 A schematic diagram elucidates the mechanism governing the functionality of the novel droplet sensor.

The mechanism of the droplet microsensor is expounded in Figure 3.2. One of the optopairs acts as an LED, emitting light upon current injection due to electron-hole recombination. The emitted light is guided to the PD across the sapphire substrate, where its absorption leads to electron-hole pair generation. Notably, droplet presence alters the sapphire boundary reflectance, modifying the light reaching the detector. Photocurrent readouts thus enable droplet detection.

3.3 Optical and electrical properties of GaN-based optoelectronic device for droplet sensing
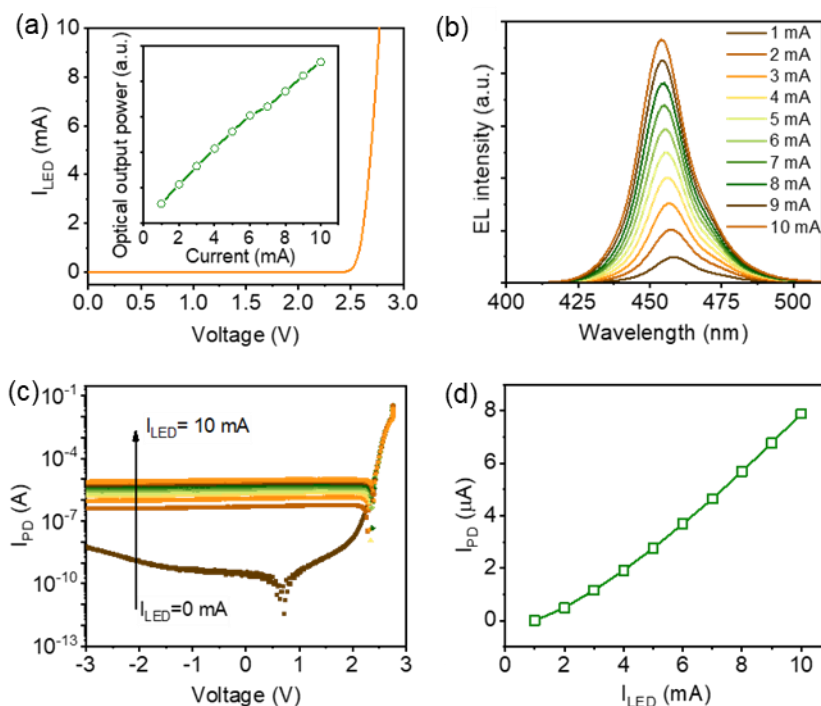
Figure 3.3 (a) I-V characteristic of the LED. Inset is the relationship between the light output power and the injection current. (b) Emission spectra of the LED while subject to varying injection currents. (c) The I-V curves of the PD across different LED currents. (d) The photocurrents of PD correlation with the LED current.

Electrical characteristics are assessed using a Keithley 2450 sourcemeter. Figure 3.3(a) illustrates the LED forward I-V characteristic, offering insight into its behavior. The inset of Figure 3.3(a) depicts the linear relationship between light output power and current. Figure 3.3(b) showcases electroluminescence spectra under varying injection currents, and the peak shifts could be primarily attributed to band-filling effects[40].

Figure 3.3(c) presents PD I-V curves at different LED currents, demonstrating the PD's response to LED emission. The linear correlation between PD photocurrent and LED intensity is evidenced in Figure 3.3(d), showcasing the linear responsivity of PD.
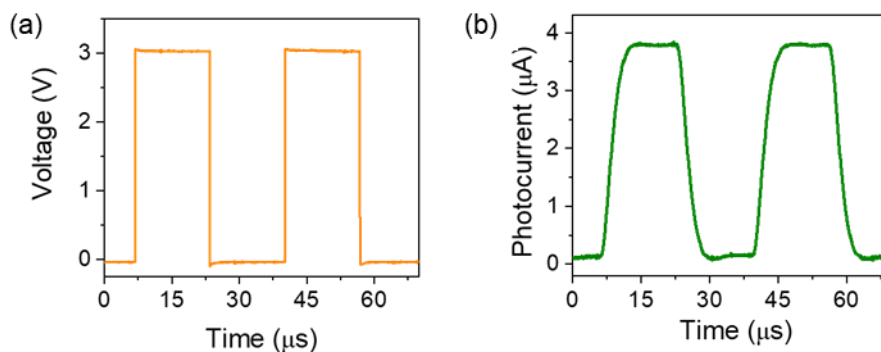
Figure 3.4 (a) Square wave signals applied to the LED. (b) Transient responses

originating from the PD.

Transient response analysis follows, involving square wave excitation and preamplified signal acquisition. Figure 3.4 portrays the time-dependent signals, highlighting rise and fall times crucial for assessing system dynamics. Quantitative system dynamics parameters are derived, including rise and fall times, defining the time for the signal to transition from 10% to 90% and from 90% to 10% of its steady value, respectively, measured at around 3.88 μs and 3.53 μs.

3.4 Sensing performance of droplet sensor
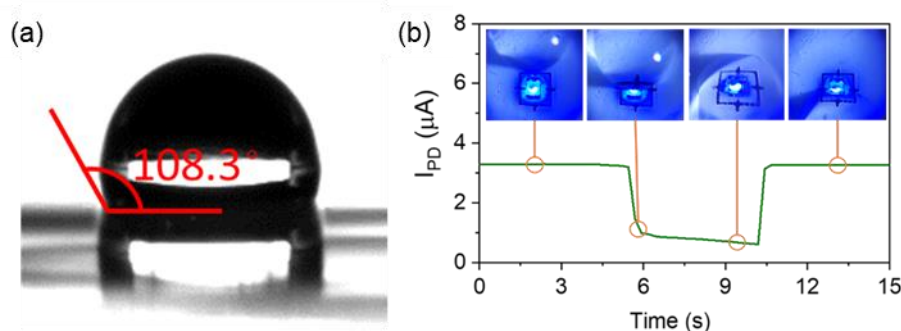
Figure 3.5 (a) The image depicting the contact angle of a water droplet on the PDMS

layer. (b) The photocurrent curve obtained during single droplet flow. The inset shows

the optical images showcasing different stages of droplet movement.
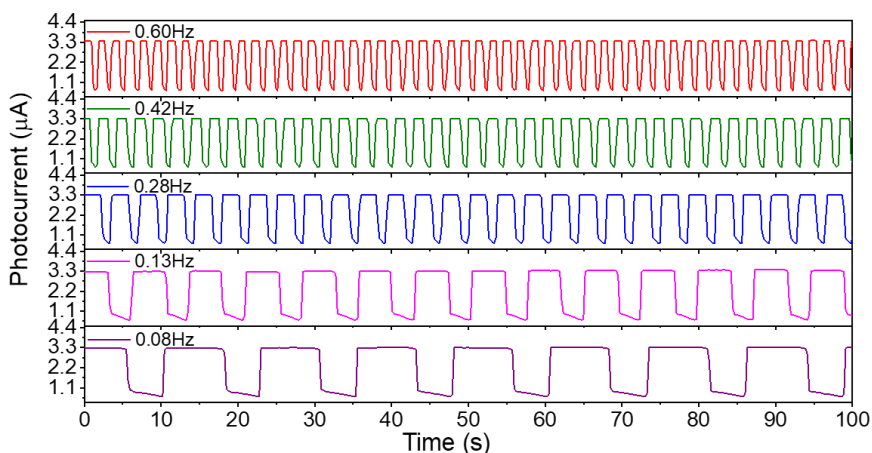
Figure 3.6 Photocurrent responses across various droplet frequencies.

Following the comprehensive characterization of the optical and electrical properties, a detailed investigation into the microsensor response to droplet flow is undertaken. Illustrated in Figure 3.5(a), the contact angle analysis between water droplets and the hydrophobic PDMS layer yields a value of 108.3° , confirming PDMS hydrophobic nature. Figure 3.5(b) visually captures the dynamic variation in photocurrent as a single water droplet traverses the sensor surface. Evidently, the photocurrent experiences a significant reduction when the droplet envelops the device, subsequently restoring to its initial value as the droplet departs. Subsequent assessments extend to varying droplet frequencies, ranging from 0.08 Hz to 0.6 Hz, as depicted in Figure 3.6. Notably, each droplet passage is distinctly discerned through corresponding changes in photocurrent, affirming the microsensor consistent response within this frequency range.

To assess the magnetic field compatibility of the device, the performance of the droplet sensor is tested under conditions with and without magnetic interference. A magnet measuring $5 \times 5 \times 10$ mm^3 is employed to establish a magnetic environment,

and Figure 3.7(a) displays the photograph of the sensor under magnetic interference. As shown in Figure 3.7(b), the photocurrent changes in the presence of magnetic interference closely align with the sensor data obtained without interference, thereby demonstrating the ability of droplet sensor to maintain stable operation in magnetically disruptive environments and confirming its excellent electromagnetic compatibility.
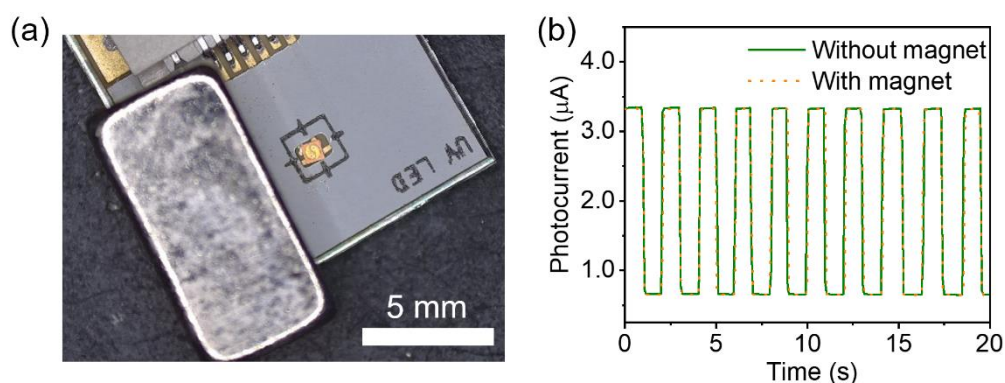
Figure 3.7 (a) Optical image of optical device under the interference of magnet.

(b) Droplet sensing performance with and without magnet interference.
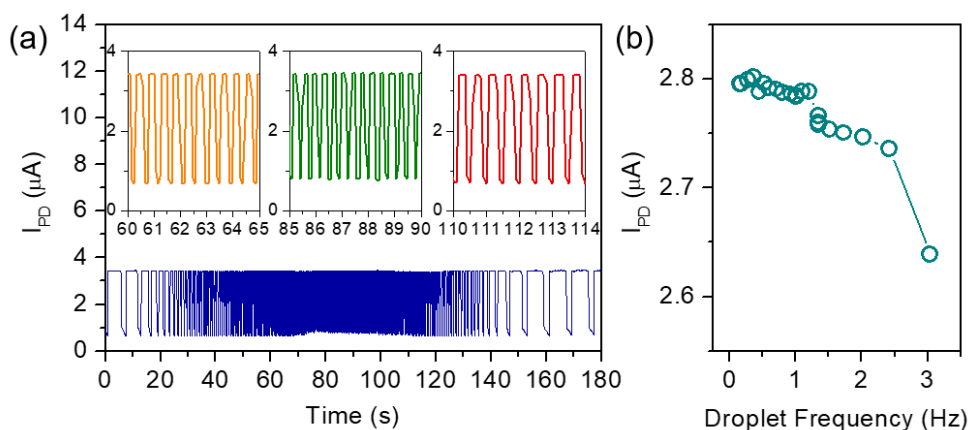
Figure 3.8 (a) Photocurrent response of the microsensor in reaction to varying droplet frequencies. (b) Chat of the peak-to-peak photocurrent as a function of droplet frequency.
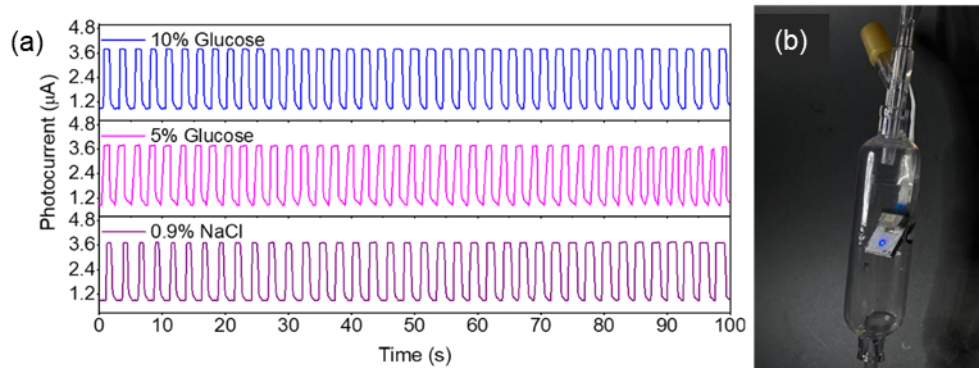
Figure 3.9 (a) Photocurrent responses of the microsensor within commercially available infusion sets, involving saline, 5% glucose solution, and 10% glucose solution. (b) Optical image showcasing the integration of the microsensor into the infusion set setup.

The frequency response of the fabricated device is subsequently scrutinized, employing varying droplet rates. Notably, the sensor demonstrates clear discernment of droplet occurrences even at a frequency of 3 Hz, as demonstrated in Figure 3.8. In a practical application demonstration, the sensor is integrated into a commercial infusion set, accommodating saline, 5% glucose solution, and 10% glucose solution. Figure 3.9 showcases the measured photocurrent response, effectively capturing a droplet frequency of approximately 0.4 Hz. Collectively, these findings underscore the significant potential of the droplet monitoring chip for practical utilization.

3.5 Conclusion

In summary, this work studied in the development of a compact GaN-based microsensor tailored for droplet detection. Leveraging shared GaN-based epilayers on a sapphire substrate, the optopairs demonstrate exceptional electrooptical properties

and enduring stability. Additionally, the GaN device exhibits rapid transient response within the microsecond range, enabling droplet recognition frequencies of up to 3 Hz. The successful integration of the microsensor into an infusion set exemplifies its tangible utility, promising practical applicability.

Chapter 4 GaN-based optoelectronic device for pH measurement

4.1 Introduction

Acidity affects a wide range of fields including the food industry, environmental monitoring, clinical medicine and life sciences. Therefore, it has been the goal of researchers to meet the different needs of pH detection in practical applications and to develop pH detection methods with simple operation, high sensitivity and fast response time[63].

Due to the small relative mass of hydrogen ions, it is difficult to directly influence the physical properties of a solution[64]. Common methods of measuring pH are based on chemical reactions. Traditional methods of measuring pH include colorimetric methods, indicator titration and electrochemical methods. The colorimetric method, represented by pH test strips, derives the pH value by comparing the color change of the liquid in contact with the test strip to a standard colorimetric chart[65]. Although this method is inexpensive and easy to operate, the low accuracy is inappropriate for practical industrial production. The second option is titration, which uses an acid-base indicator to produce a precise pH value by titration[66]. In contrast to the colorimetric method, the titration method possesses a highly accurate but complicated and time-consuming with operation. The most common method of pH measurement is the electrochemical pH meter[67, 68]. The pH meter works by forming a primary cell between electrodes and ions in solution, using the potential difference between different

samples to determine the pH value. This principle of operation endows the pH meter high accuracy and fast response, but it also results in the inability to work in electromagnetic environments. In addition, the working electrode of a pH meter has a large volume, requiring the provision of several milliliters of sample to ensure the accuracy of the test. Moreover, the pH meter has to go through the tedious process of calibration each time, which further complicates the test.

In response to these challenges, researchers have innovated optical solutions, which include fiber-optic approaches and fluorescent probes. The fluorescent probe method, recognized for its precision and specificity, is particularly suited for high-value cellular assays[69]. However, due to its narrowly focused applicability, it is not included in the broader discussion for wide-range pH testing. Currently, most of the research based on optical methods are fiber-optic pH sensors[70]. Fiber-optic pH sensors are usually made by infiltrating a pH indicator into a porous polymer as a coating on the surface of the fiber after removing the fiber cladding. The sensor uses the change in spectral properties of the fiber-optic sensing structure to obtain the pH value of the corresponding sample, which is highly accurate and resistant to electromagnetic interference[71]. The porous polymer substrate utilized to immobilize the indicator is typically a silica film produced by sol-gel method from tetraethoxysilane (TEOS). Such porous matrix is chemically inert, thermally and mechanically stable, while allowing for faster ion diffusion rates, making it ideal for immobilising pH indicators[72]. The photostable property further highlights the potential of porous silica substrate for optical chemical sensing applications. As a result, fiber optic pH sensors equipped with

sol-gel films are characterised by fast response, durability and mechanical robustness. However, the fiber-optic method requires the removal of the fiber-optic cladding by the hazardous hydrofluoric acid (HF) treatment and the large size of the external fiber-optic equipment, which is not conducive to on-site testing.

In pursuit of rapid testing across an expansive pH range, this study incorporated a more compact GaN device with reduced power consumption in place of the optical fiber, while combining it with the TEOS-based sol-gel film attached to a mixed indicator. Importantly, the monolithic integration technique was used to drastically shrink the size of the LED and PD in the GaN device to a mere 0.1 mm^3, thereby eliminating the need for extensive external facilities. The process of detection by the pH sensor is investigated through the evaluation of the reflective spectrum of the sensitive material. Further assessment of the stability of pH sensor is conducted, considering aspects such as resistance to ionic interference and repeatability. The proposed pH sensor is characterized by its low cost, diminutive size, swift response time, and excellent repeatability. Such a compact and efficient design offers promise for non-invasive, on-site detection in lab-on-chip applications.

4.2 Preparation and optimization of pH sensitive film

In order to realize optical pH sensing, it is necessary to select a sensitive material with an optical response of pH. The optical response can be a change in refractive index or a change in reflectance of the chip response wavelength range. There are two preferred choices at this point: a pH-sensitive hydrogel or a porous film anchored to a pH indicator. Hydrogels generally respond slowly and bind weakly to hydrophobic

sapphire surfaces, so porous films anchored to pH indicators are tried.

The experimentally designed pH-sensitive film has a three-dimensional spatial network structure, which allows the pH-sensitive indicator to be encapsulated in the three-dimensional pore array of the gel and adsorbed on the chip surface through a drying process. The sol-gel technology is a process in which one or several highly chemically active component substances are used as precursors, and these chemical reagent raw materials are homogeneously mixed in the liquid phase, and after some series of complex hydrolysis and condensation reactions, a stable and transparent sol-gel system is formed in solution, and then block materials, fiber materials, films, and composites are made by the drying process [73]. At present, the excellent characteristics of sol-gel technology are widely used in the preparation of ferroelectric materials, superconducting materials, powder metallurgy, ceramic materials, thin films and other materials.

4.2.1 The process of sol-gel preparing

The basic process of preparing a sol-gel is divided into the following four steps: preparation of a homogeneous precursor solution, preparation of a sol, aging, and drying.

Homogeneous precursor solutions are prepared to ensure that the hydrolysis reaction occurs at the molecular weight level. Due to the low solubility of esters in water, an appropriate amount of alcohol needs to be added as a solvent. In order to accelerate the rate of hydrolysis, polycondensation reaction, an appropriate amount of catalyst needs to be added to the mixed solution [74]. Usually, HCl is selected as the

acidic catalyst and NH_4OH as the basic catalyst. Continuous stirring of the mixed solution is also required during the preparation process to ensure the homogeneity of the precursor solution [75].

There are two common methods of preparing the sol: polymerization of molecular units (PMU) and destabilization of colloidal solutions (DCS) [76]. In the PMU method, the metal alkoxide is dissolved in organic solvent and partially hydrolyzed by controlling the amount of water added, and then the sol was formed by polymerization. The PMU method requires less water, which will affect the hydrolysis reaction in the glue, prompting the hydrolysis products and part of the unhydrolyzed ester compounds to polymerization, and then the formation of polymerized sol. The DCS method require a larger amount of water, which will prompt the ester compounds to fully hydrolyze, and then the formation of particles of sol. The hydrolysis and polycondensation is the fundamental reason for the transformation of homogeneous solution into sol, therefore, the correct selection of the reaction process: the amount of water, catalyst and solution pH and hydrolysis temperature and other conditions is the key to the preparation of high-quality sol [77].

Then, the sol is aged to obtain a wet gel. During the aging process, the sol changes to a wet gel due to solvent evaporation and continuing polycondensation reactions. During this process, the particles undergo Ostward ripening and gradually aggregate to form a network structure. This network structure meets the needs of the embedded the pH indicator [78].

Drying of wet gel is an extremely complex process, in the drying process there are

four kinds of force (capillary pressure, osmotic pressure, separation pressure, humidity stress) at the same time act on the wet gel, which is easy to cause wet gel cracking. In addition, a large number of solvents and water within the wet gel will make the drying process produce a large volume contraction, which in turn exacerbates the cracking of the wet gel. Therefore, it is extremely important to solve the cracking problem of gel in the drying process. At present, often through the control of drying conditions, adding chemical additives and the use of supercritical drying technology to solve this problem [79].

4.2.2 Optimization of the hydrolytic precursor ratio

Tetraethoxysilane (TEOS) is an important raw material for the preparation of silicone resin materials. All compounds containing the Si-C bond are commonly known as organosilicon compounds, and it is customary to treat those compounds that connect organic groups to silicon atoms through oxygen, sulfur, nitrogen, etc. as organosilicon compounds. Among them, polysiloxanes composed of silicon-oxygen bond (-Si-O-Si-) as the skeleton are the most numerous, the most deeply researched, and the most widely used class of organosilicon compounds, accounting for more than 90% of the total dosage. TEOS is used as a raw material, and a suitable TEOS prepolymer is obtained by hydrolysis reaction. TEOS can be hydrolyzed and condensed under the catalysis of acid or base [80]. The hydrolysis process is complex, and different forms of intermediates are produced under different conditions. In order to ensure that the pH-sensitive indicator can be successfully embedded in the three-dimensional pore array of the gel and attached to the surface of the chip, the amount and proportion of

individual chemical reagents need to be precisely controlled [81].

From a thermodynamic point of view, the complete hydrolysis of TEOS ultimately produces silica and ethanol, and the hydrolysis equation can be expressed as follows [82]:

$$Si(OC_2H_5)_4 + 2H_2O \rightarrow 4C_2H_5OH + SiO_2 \qquad\qquad 4.1$$
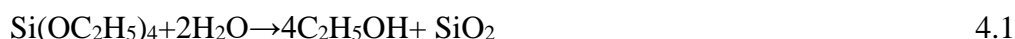
As can be seen from equation 4.1, 2 mol of water is required to completely hydrolyze 1 mol of TEOS.

The other extreme case is that all the silicon hydroxyl groups are not condensed, in which case 4 mol of water is required to completely hydrolyze 1 mol of TEOS:

$$Si(OC_2H_5)_4 + H_2O \rightarrow C_2H_5OH + Si(OC_2H_5)_3(OH) \qquad\qquad 4.2$$

$$Si(OC_2H_5)_3(OH) + H_2O \rightarrow C_2H_5OH + Si(OC_2H_5)_2(OH)_2 \qquad\qquad 4.3$$

$$Si(OC_2H_5)_2(OH)_2 + H_2O \rightarrow C_2H_5OH + Si(OC_2H_5)(OH)_3 \qquad\qquad 4.4$$

$$Si(OC_2H_5)(OH)_3 + H_2O \rightarrow C_2H_5OH + Si(OH)_4 \qquad\qquad 4.5$$
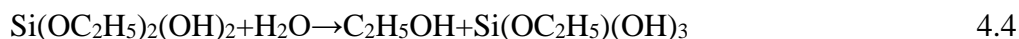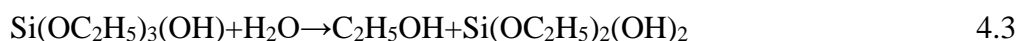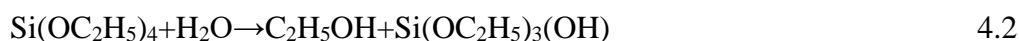
The most common case is that the ethoxy group is not fully hydrolyzed and the silica hydroxyl group is not fully condensed. In this case, the hydrolysis equation can be expressed in equation 4.6, where $m = 0, 1, 2, 3, 4$, $m \leq n \leq 4$:

$$Si(OEt)_4 + nH_2O \rightarrow SiO_{(n-m)/2}(OR)_{4-n}(OH)_m \qquad\qquad 4.6$$

In addition, when the molar ratio of water to TEOS $R_0 < 4$, the gelling time increases with the increase of R_0. This is because when $R_0 > 4$, TEOS has been completely hydrolyzed, the larger the R_0, TEOS hydrolyzed to form Si-OH group concentration is smaller, the more difficult to react between the groups by collision. As a result, the gelation time increases. In addition, water as one of the products of the

polycondensation reaction, the greater the concentration, the more difficult to carry out the polycondensation reaction [83].

At the same time, the amount of water will also affect the subsequent drying problem. Adding too much water will inevitably increase the drying stress of the sensitive film in the drying process, exacerbating the cracking phenomenon of the sensitive film.

Therefore, the synthesis of various factors and access to relevant information, this paper finally determine the experimental volume ratio of TEOS and distilled water is 3:1. To assume silica hydroxyl is not condensed, the theory of most of the TEOS only hydrolyzed off two ethoxy, which is conducive to the generation of the expected 2 or 3 monomer condensation of the prepolymer.

Due to the limited solubility of TEOS in water, a certain amount of co-solvent needs to be added in order to prepare precursor gels quickly and efficiently. The co-solvent is required to be miscible with both TEOS and water, so ethanol is chosen as the co-solvent. The TEOS-C_2H_5OH-H_2O system may still be in the ternary immiscibility zone if less ethanol is added, and the hydrolysis reaction of the system will be inhibited if more ethanol is added. In this paper, the final determination of the addition of ethanol and the volume ratio of TEOS is 1:1.

4.2.3 Optimization of the condensation catalyst and temperature

In the experiments, hydrolysis and polycondensation reactions are carried out simultaneously. The hydrolysis reaction can be carried out at a faster rate at room temperature, but the polycondensation reaction is slower, and the hydrolysis-

polycondensation reaction can be accelerated at higher temperatures and in the presence of a catalyst, which can have a great impact on the structure of the final gel formed as well as on the pH-sensitive properties [84]. Different catalysts in the case of different reaction time of the system, the generation of pH-sensitive membrane structure is different, which will lead to a great difference in the sensitivity of the sensor response time, as well as non-response to specific acids and bases, etc. In addition, too high a concentration of catalysts will lead to the generation of sol-gel retention time becomes shorter, which is not conducive to the reproducibility of the sensor coating as well as the storage of the sol-gel, so it is necessary to choose the right catalyst type, concentration, and the reaction time in the process of the experiment.

There are two general condensation mechanisms as follows.

1. Acid-catalyzed condensation

The reaction can be divided into two steps. In the first step, the proton of the catalyst associates to the oxygen atom of the silicon hydroxyl group as in equation 4.7.

$$\equiv Si\text{-}OH + H^+ \rightarrow \equiv Si\text{-}O\text{-}H + \text{-}H \qquad\qquad 4.7$$

This step is very rapid and is followed by the step that determines the rate of the reaction, as in equation 4.8.

$$\equiv Si\text{-}OH + H^+ \equiv Si\text{-}O\text{-}H + \text{-}H \rightarrow \equiv Si\text{-}O\text{-}Si\equiv + H_2O + H^+ \qquad\qquad 4.8$$
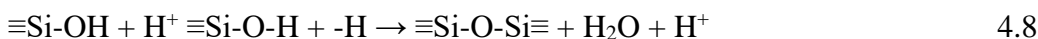
Equation 4.8 can be viewed as a nucleophilic attack by an oxygen on a silicon hydroxyl group on a silicon atom in a silicon hydroxyl molecule with a proton. When the silicon atom contains an electron-absorbing group, it reduces the electron cloud density on the oxygen atom of the silicon hydroxyl group, thus reducing its ability to

make a nucleophilic attack and decreasing the rate of the condensation reaction; conversely, if the silicon atom contains an electron-pushing group, it accelerates the reaction as in equation 4.9.

$$\equiv Si\text{-}OH + OH^- \rightarrow \ \equiv Si\text{-}O\text{-} + H_2O \qquad\qquad 4.9$$

2. Base-catalyzed condensation

The starting step of the reaction is:

$$\equiv Si\text{-}O + \equiv Si\text{-}O\text{-}H \rightarrow \ \equiv Si\text{-}O\text{-}Si\equiv + OH^- \qquad\qquad 4.10$$
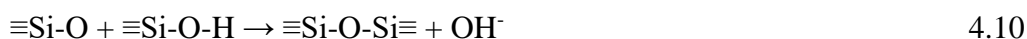
Equation 4.10 can be viewed as a nucleophilic attack of silicon in the silanol molecule by the anion of silicon oxygen. If the silicon in the silanol molecule contains electron-withdrawing groups, the electron cloud density on the silicon decreases, and it is susceptible to attack by the anionic silicon oxygen and therefore the reaction rate increases.

In fact, as the degree of condensation increases, the silyl hydroxyl group on the intermediate becomes more and more acidic, the easier it is to negatively ionize, yet the less likely it is to undergo nucleophilic attack. Therefore, the reaction under alkaline conditions causes the system to proceed more and more in the acidic direction and the system becomes unstable. A number of experimental results prove this point. The study showed that acid-catalyzed condensation as well as alkali-catalyzed condensation, and found that hydrolytic condensation under alkali-catalyzed hydrolysis, the reaction is violent, and its resulting hydrolysate cannot be effectively stored, while under acid-catalyzed hydrolysis, the resulting prepolymers have good storability [85].

On the other hand, the higher the temperature would shorten the gelation time of

the system. This is due to the elevation of the system temperature, the hydrolysis activity of TEOS increased at the same time as the average kinetic energy of water molecules increased, the rate of molecular movement accelerated, increasing the probability of collision between TEOS and water molecules. Ultimately, the hydrolysis reaction is accelerated, and the gelling time of the mixed solution is shortened.

In this work, after adding ammonia and hydrochloric acid solutions, both sensitive films cracked severely at the time of cracking. To prevent the cracking problem, we do not add any acid or alkali as the catalyst.

From the above, the final formulation of the pH sensitive film in this work is as follows.

4.2mg of cresol red, 4.2mg of chlorophenol red and 8.2mg of bromophenol blue are weighed into a 10mL beaker. Then, 3ml of TEOS, 3ml of anhydrous ethanol, 1ml of distilled (DI) water and 30μL of Triton X-100 are added and mixed well to obtain an orange-clarified liquid. Triton X-100 as a surfactant does not alter the course of the hydrolysis-condensation reaction and at the same time mitigates cracking during the drying process [86].

4.3 Fabrication and working principle of pH sensor

A 4-inch c-plane sapphire is selected as the substrate on which the epitaxial structure is grown on by MOCVD. The epitaxial structure includes undoped GaN, Si-doped n-type GaN, InGaN/GaN MQWs, and Mg-doped p-type GaN. The luminescent region is firstly defined by Cl_2-based ICP dry etching. To block the vertical current spread, SiO_2 was deposited on the p-GaN by PECVD to form the current blocking layer.

A thin layer of indium tin oxide is then deposited using reactive plasma deposition to form the current spreading layer. As the LED and PD are electrically isolated, the induced coupling plasma is applied to form a 10 μm spacing between the LED and PD. Electron beam evaporation deposits mixed metals at the corresponding positions on n-GaN and p-GaN to form the n- and p-electrodes, respectively. A 360 nm SiO_2 passivation layer is deposited on the chip surface by PECVD and then electron beam evaporation deposits the n-pad and p-pad on top of the n-electrode and p-electrode, respectively. Finally, the processed wafer is diced into 1100×1300 μm^2 chips.

The sol-gel solution is placed in an oil bath and stirred at 60 ℃ for 10h to obtain a viscous sol. 0.1μL of sol is added dropwise to the surface of the chip and spreads naturally as a thin film. After drying for 10 min at room temperature and pressure, the device is immersed in water for 20 min to remove the unbound indicator.

4.4 Optical and electrical properties of GaN-based optoelectronic device for pH measurement
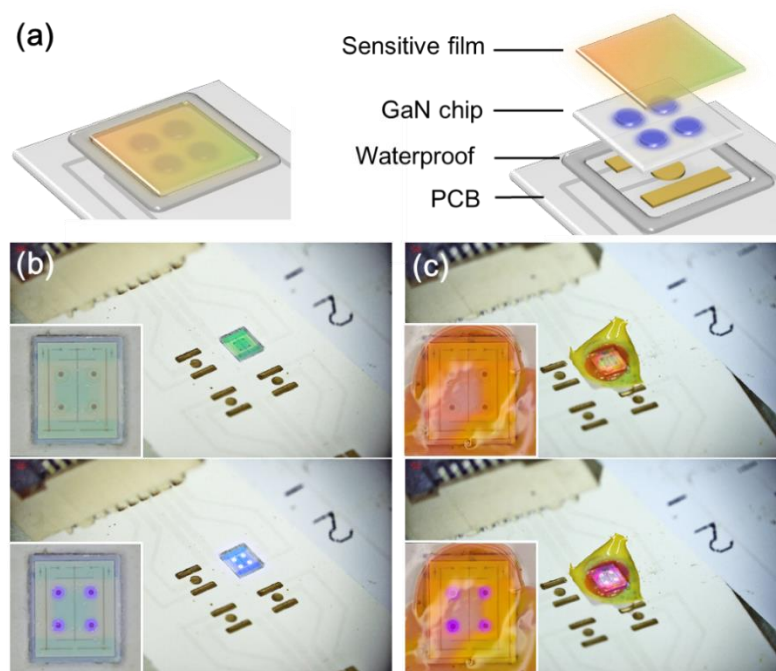
Figure 4.1 (a) Schematic diagram of the structure of the pH sensor. Photographs in 45 °view of unilluminated and illuminated (b) bare GaN chip and (c) assembled pH sensor. The insets are enlarged bird's eye views.

The architectural design of the pH sensor is depicted in Figure 4.1(a). At the outset of the sensor assembly, the chip is soldered onto the PCB using high-temperature solder paste. An epoxy resin adhesive is then applied to the perimeter of the GaN chip to prevent potential short-circuiting of the optoelectronic device by the liquid under examination. The process concludes with the fabrication of the sensitive film on the chip surface, thus forming the pH sensor. As clearly visible in Figure 4.1(b), the LED is designed with four circular light-emitting areas centrally located on the chip, each having a radius of 80 μm, with the remaining region functioning as the PD. Figure 4.1(c) exhibits the assembled pH sensor. The chip is encased in an epoxy resin adhesive, which does not adhere to the top surface of the sapphire. The sensitive film, transparent and

consistently colored in orange, presents a thickness approximating 16 μm.
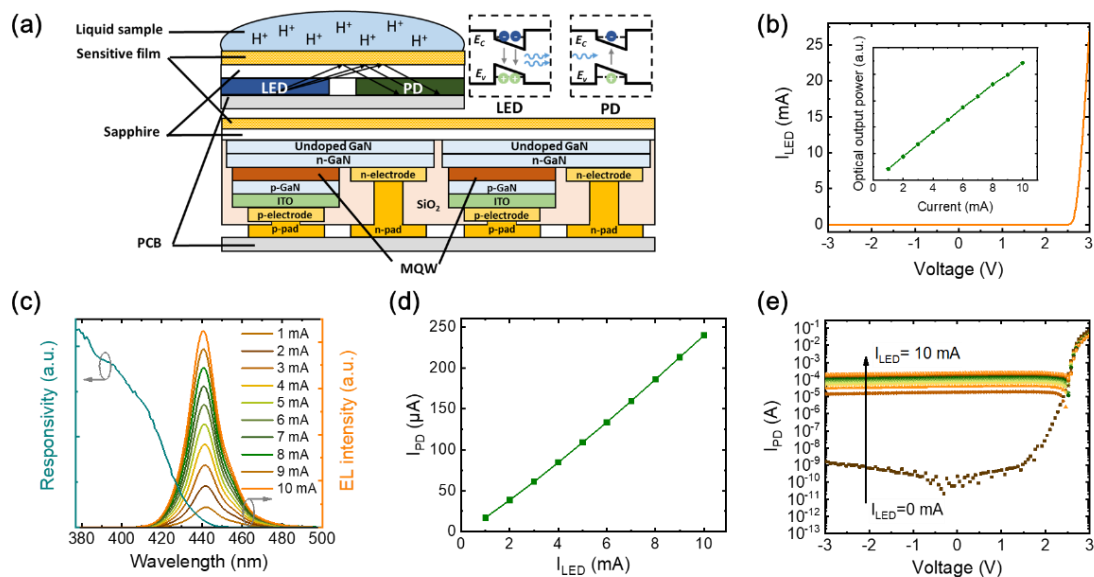
Figure 4.2 (a) The schematic diagram of the working principle of the pH sensor. (b) I-V curve of the LED. The inset demonstrate L-I plot of the LED. (c) EL spectra of the LED biased from 1 mA to 10 mA with the responsivity spectrum of the unbiased PD. (d) The chart illustrates PD photocurrent with the operated LED under different injection current. (e) I-V curves of the PD.

Figure 4.2(a) delineates the operational principle of the pH sensor. Upon current injection, the LED illuminates due to the recombination of the injected charge carriers with holes present in the MQWs. This emitted light is reflected and captured by the InGaN layer of the PD, thereby engendering electron-hole pairs and subsequently a photocurrent. The liquid subject to measurement is administered onto the surface of the sensitive film, permeating the interstitial spaces and interacting with the indicators. When dissolved in the solution, the pH indicators are partially ionised, forming indicator ions and hydrogen ions (or hydroxide ions). When the pH of the solution is

lowered, the indicators gain protons and the base component forms the conjugate acid. While the pH of the solution increases, protons are lost and the indicators transform to the conjugate base. Conjugate acid-base pairs demonstrate different colors due to the different structures. Thus, as the pH changes, the shift in the structures of the conjugate pairs leads to a change in the reflectance spectra, which is macroscopically manifested as a change in color. As the pH level of the liquid under scrutiny fluctuates, the color of the indicator embedded in the pH-sensitive film undergoes transformation. Consequently, the variation in the reflection spectrum incurs a change in the volume of light receivable by the PD.

The electrical and optical properties of the optoelectronic chips are first investigated. The electrical properties of the LEDs and PDs are measured using a Keithley 2450 sourcemeter. The I-V curve for the LED in Figure 4.2(b) shows an open voltage of 2.56 V and a resistance of 20.1 Ω as determined from the inverse slope. Figure 4.2(c) displays the EL spectrum of the LED subject to an injection current ranging between 1-10 mA. The peak wavelength is gradually blue-shifted from 442.1 nm to 440.6 nm due to band gap filling effects. The responsivity curve of the PD shows an overlap of approximately 30 nm with the emission spectra. Due to the Stark effect of quantum confinement and fluctuating indium content in the InGaN/GaN multiple quantum well, the responsivity experiences a gradual decrease with increasing wavelength. Figure 4.2(d) elucidates the correlation between the photocurrent of the PD and the current injected into the LED. In the injection current range of 1-10 mA, the PD photocurrent exhibits a linear escalation as the LED injection current amplifies.

The I-V characteristics of the PD are explored further and plotted in Figure 4.2(e). The dark current under reverse bias is relatively stable at 10^{-8} A, suggesting that the leakage current would not significantly affect the performance of the sensor. When 1-10 mA of current is injected into LED, the photocurrent rapidly increases to 10^{-5}-10^{-4} A, indicating that the PD has high responsiveness to the LED.
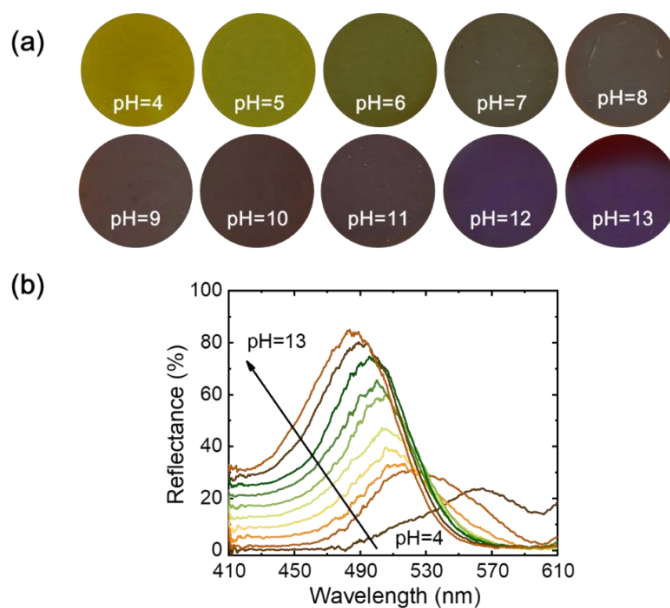
Figure 4.3. (a) Photographs and (b) reflectance spectra of sensitive films at pH 4-13.

Given that the sensitive film comprises three indicators, the color variation with pH represents a superimposition of three colors rather than a single color transition. To lucidly illustrate the color shift of the indicators, the sensitive film is applied to a coverslip, which is subsequently positioned on white paper after the addition of liquids of various pH levels for observation. As evident from Figure 4.3(a), the sensitive film manifests a yellow hue at pH 4, and the color progressively transitions through green, cyan, blue, to purple as the pH escalates.

Moreover, the reflective spectra corresponding to the sensitive film are analyzed,

as depicted in Figure 4.3(b). A singular reflection peak is noted at 450-540 nm, with the

peak wavelength gradually shifting from 510 nm to 490 nm in correlation with the pH

increase. Concurrently, the reflectance intensity within the 400-450 nm range

progressively ascends with the rise in pH. In light of the GaN chip operational principle

and the PD spectral responsivity outlined above, the PD response to wavelengths below

445 nm suggests that the photocurrent may enhance with the increment in pH.

4.5 Sensing performance of pH sensor
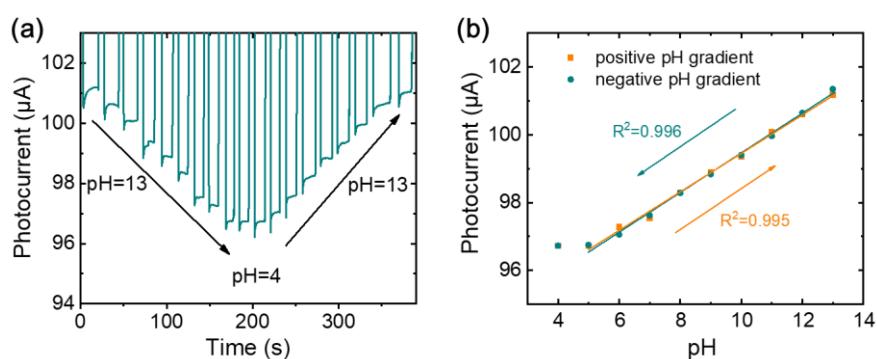
Figure 4.4 (a) Photocurrent response for pH with positive and negative gradients. (b)

Plot of PD photocurrent with pH changing positive and negative gradients.

The performance of the pH sensor is characterized using standard pH phosphate

buffer solutions (PBS, 0.2M), with the test conducted under a 10 mA LED injection

current. For testing, a 1 μL droplet of the standard pH liquid is added onto the surface

of sensitive film. The sensitive film possesses a certain degree of light transmittance,

and when a drop of the liquid to be measured is added to the surface of the sensitive

film, the photocurrent decreases due to the effect of the refractive index of the droplet.

As the droplet diffuses into the sensitive film, the photocurrent gradually rises. The test

waits for the photocurrent to stabilize before any residual moisture on the sensor surface

is wiped off, and then proceeds to the next test. Primarily, the standard liquid ranging from pH 4 to 13 is subjected to consecutive testing.

As depicted in Figure 4.4(a), the photocurrent exhibits a consistent ascension with the increase in pH, corroborating earlier predictions. The pH sensor response time, as derived from the fitting of the photocurrent versus time curve for each test, predominantly falls within the 3-5s range, averaging at 3.8s. The recorded photocurrent signal is plotted against the pH using the linearly fitted lines as illustrated in Figure 4.4(b). The photocurrent signals exhibit an excellent linear relationship with pH within the pH=5-13 range, as denoted by an R-squared value of 0.996. The insensitivity to liquids with a pH below 5 is attributable to the reflectance spectrum at this pH being outside the PD response interval. The fabricated pH sensor is subjected to continuous pH gradient testing to ascertain measurement errors instigated by variations in positive and negative gradients. Figures 4.4(b) portray the results of the positive and negative pH gradient testing and adjustments, indicating that the device performance remains unaffected by different gradients.
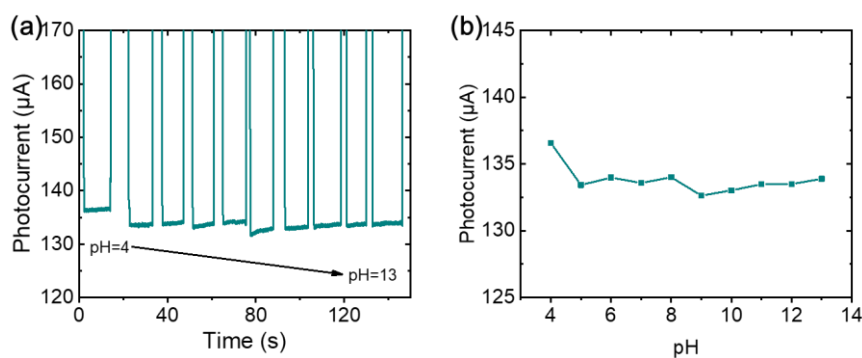
Figure 4.5 (a) Photocurrent response for pH changes of bare chip. (b) Plot of PD photocurrent response of bare chip with pH changing.

As a control, the response of the bare chip to pH was first tested. As can be seen from Figure 4.5, the photocurrent response does not show a significant change trend with the change of pH. In addition, thinner and thicker sensitive films, with thicknesses of 8 μm and 23 μm, are prepared for pH sensing.
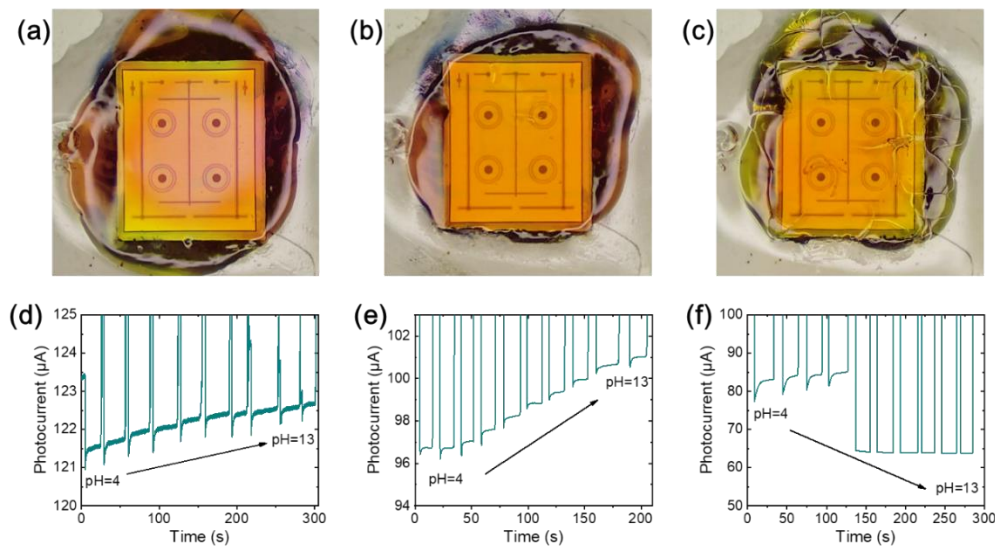
Figure 4.6 Micrographs of the pH sensor equipped with (a) 8μm (b) 16μm and (c) 23μm sensitive film. Photocurrent response of the pH sensor equipped with (d) 8μm (e) 16μm and (f) 23μm sensitive film.

Figure 4.6(a-c) shows photographs of sensors with three different thicknesses of sensitive films. As illustrated in Figure 4.6(d), the device equipped with thin films do not respond significantly to the pH changing. On the other hand, when the thickness is extended to 23 μm, the film may fail because of tension during the drying process. Cracking greatly reduces the lifetime of the thick film, demonstrated in Figure 4.5(e), where the sensor no longer responds to an increase in pH after 4 tests.
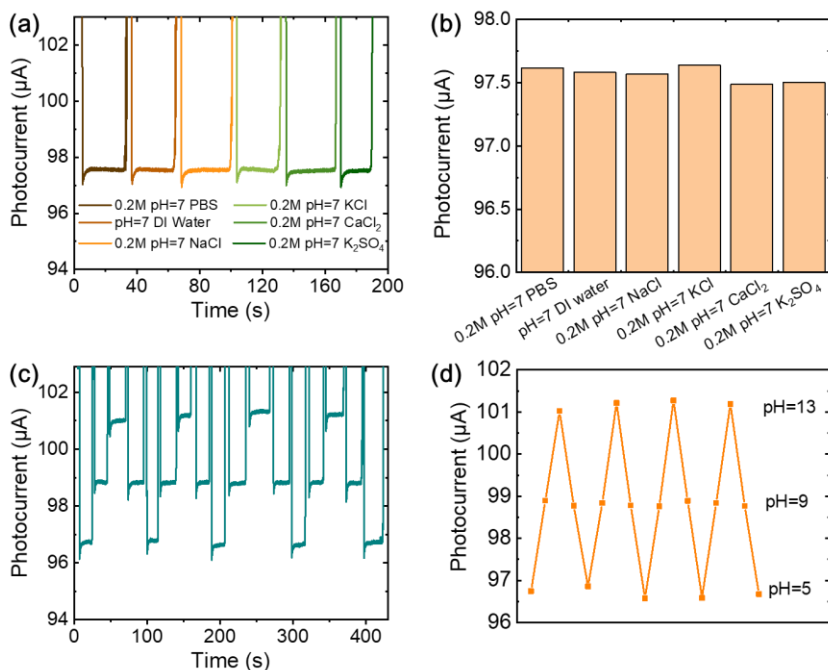
Figure 4.7 (a) Photocurrent response for various neutral solutions. (b) Plot of PD photocurrent versus neutral solutions (c) Photocurrent response for pH cycles between 5, 9 and 13. (d) Plot of PD photocurrent versus pH cycling.

The effect of different salt and ion concentrations on the sensor is further explored. Ionic interference tests are performed by selecting 0.2 M pH 7 PBS buffer, DI water and four common salt solutions. The solutes of the four salt solutions are NaCl, KCl, $CaCl_2$, and K_2SO_4, and the molar concentrations of the solutes are 0.2 M with the solutions pH adjusted to 7. The test and fitting outcomes presented in Figures 4.7(a) and (b) are within acceptable error margins, highlighting that the pH sensor possesses robust resistance to interference.

The reproducibility of pH sensor is assessed through continuous recording of the photocurrent within the pH 5-13 range. The photocurrent can rebound to maximum and minimum values at pH=13 and pH=5 respectively, as shown in Figures 4.7(c) and (d),

implying that the sensing readings are highly reproducible.
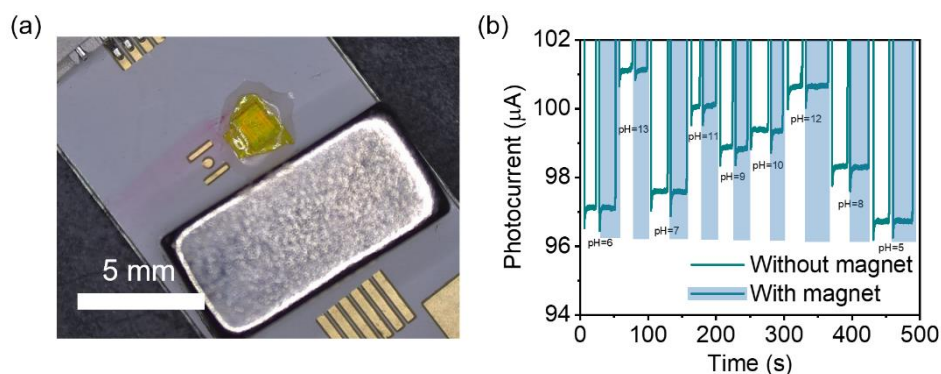
Figure 4.8 (a) Optical image of optical device under the interference of magnet. (b) Random pH sensing performance and electromagnetic immunity performance test of the device. The blue shaded areas are the photocurrent changes under magnetic interference.

To evaluate the performance of the pH sensor with disordered pH solutions, solutions with pH values ranging from 5 to 13 are randomly tested. Figure 4.8(b) displays a stable photocurrent response of the sensor to different pH levels, demonstrating its ability to accurately determine the acidity or alkalinity of solutions during random pH tests. Additionally, to assess the electromagnetic immunity of the sensor, electromagnetic interference was introduced during these tests. A magnet measuring $5 \times 5 \times 10$ mm^3 is used to establish a magnetic field environment, and Figure 4.8(a) shows the photograph of the sensor under magnetic field. The blue shaded areas in Figure 4.8(b) represent the photocurrent changes under magnetic interference. The consistent readings between shaded and non-shaded areas indicate that the sensor remains unaffected by magnetic fields, suggesting that the designed device can provide reliable and stable pH sensing performance in electromagnetic environments.

Table 4.1 Comparison with previously reported pH sensors

Sensor type	Sensitive materials	Sensing range	Sensor size	Sample volume	Response time	External light source	Ref.
Membrane resistance	Poly(HEMA) -based hydrogel	7.35-7.45	$1000 \times 30 \times 2\mu m^3$	6×10^{-4} cm^3	On the order of minutes	Required	[100]
Colorimetric	PANI/PEG composite	2-8	Circle with 2mm diameter	2μL	-	Required	[101]
Colorimetric	PVA/ acidochromic	5-12	1×1 cm^2	Immersed	1s	Required	[102]
Electrochemical	Hydrogen ionophore membrane	5-8.5	Conical electrodes with 1500 μm height and 400 μm diameter	-	$T_{95} < 5s$	Required	[103]
Colorimetric	Carboxymethyl cellulose/ bacterial cellulose + pH indicators	4-9	-	10μL	-	Required	[104]
Electrochemical	PANI + Carbon	3-10	1×2 cm^2	100μL	-	Required	[105]
Optical	SiO$_2$ film + pH indicators	5-13	1100×1300 μm^2	1 μL	3.8s	Not Required	This work

Table 4.1 aggregates and compares pH sensors reported in recent years with the present study [87-92]. As per the comparative outcomes, the pH sensor in this work features a compact design with small dimensions and a small sample volume that emphasizes the portability of the sensor. In addition, the optoelectronic pH sensor exhibits a rapid response capability over a broad dynamic pH range without the external light source, marking a substantial advance over previous endeavors.

4.6 Conclusion

In conclusion, this study presents the design of a pH sensor based on a monolithic integrated GaN-based optoelectronic chip, which operates by modulating the reflection intensity of indicators within specific wavelength regions at different pH levels. By integrating three kinds of indicators to extend the pH detection range, a wide linear sensing span from 5 to 13 is realized. The sensor incorporates a porous silica sensitive substrate with a thickness of merely 16μm, resulting in an average response time of just 3.8s. The sensor is able to operate in an electromagnetic environment and perform energy-efficient chip-level sensing attributable to the millimeter-sized low-power optoelectronic chip. This offers significant practical value for sensing applications such as real-time pH monitoring.

Chapter 5 GaN-based optoelectronic nose for organic liquid identification

5.1 Introduction

The identification of organic solvents is an important task in various industrial and research fields [93]. Traditional methods such as gas chromatography and mass spectrometry require expensive equipment and trained personnel [94]. Therefore, there is a growing demand for alternative methods that are more cost-effective, portable, and easy to use.

One promising approach is based on mimicking the human olfactory perception system, also known as artificial noses [95]. To be specific, artificial noses simulate the nasal cavity, olfactory nerve and other tissues in an artificial way to perceive the external environment. With the development of electronics and nanotechnology, artificial noses diversified with intelligence, which has been rapidly developed and widely used. Among them, electronic noses (E-noses) and photonic noses (P-noses) are of particular interest. E-noses base the principles of electrochemistry [96, 97], semiconductors or quartz crystal micro-tensions to detect and identify gases by measuring changes in the electrical properties of the sensor. Although commercially available, E-noses are undeniably limited by radiation or high electric/magnetic fields.

While on the other side, P-noses with photonic technology provide researchers with new ideas for electromagnetic immune sensor [98, 99]. Theoretically, the guest molecule is recognized in P-noses by detecting changes in the optical properties of the

sensitive material. Benefiting from advances in photonic technology, the sensitive materials of P-noses have improved the sensitivity and stability of sense, providing a non-invasive solution for detecting organic chemicals. Photonic crystals, as materials with a periodic structure, have a photonic band gap effect that enables selective transmission of light at specific wavelengths [100, 101]. The variation in the optical properties of photonic crystals can be analyzed by spectrometers, smartphones or even the naked eye, making it possible to detect organic substances on site [102]. Whilst P-noses have significantly improved the bulky and time-consuming traditional instruments of organic identification, most P-noses techniques still require external optical measurement devices that cannot meet the sensing needs of lab-on-chips and wearables. On the other hand, P-noses based on colorimetric methods, which are distinguishable to the naked eye, can lead to low sensing accuracy due to differences in the perception of color by different people.

In this work, we propose a photonic crystal optoelectronic nose based on a GaN-based optoelectronic chip to be applied in the identification of organic compounds. It is worth mentioning that LED and PD are compressed into a $0.21mm^3$ chip, achieving a high degree of integration of the conventional light source and photodetector. Self-assembled photonic crystals are constructed directly on the surface of the photonic chip to fingerprint the organic compounds by using the change in the photocurrent and recovery time, allowing rapid and precise identification of organic species in the field within 30 seconds. The proposed optoelectronic nose offers a sensitive and rapid method for detecting and identifying organic chemicals, which is critical for

environmental monitoring, industrial safety, and public health.

5.2 Preparation and characterization of optoelectronic nose

The GaN-based optoelectronic flip-chip consists of LEDs and PDs, which are manufactured by a wafer-level manufacturing process. The undoped GaN, Si-doped GaN, InGaN/GaN MQWs and Mg-doped GaN are grown sequentially on a 4-inch *c*-surface sapphire substrate using MOCVD. The LED and PD mesas are defined by photolithography and dry etching with ICP to expose the n-GaN. An ITO layer of 120 nm thickness is deposited on the p-GaN surface by reactive plasma deposition to act as a current spreading layer. After electrically isolating LED and PD by ICP, 1.65 μm Cr/Al/Ti/Pt/Au is plated by electron beam evaporation on the ITO layer and the exposed n-GaN layer as p-electrodes and n-electrodes. A 360 nm SiO_2 passivation layer is then deposited by plasma-enhanced chemical vapor deposition directly onto the wafer, followed by 46 layers of SiO_2/TiO_2 as distributed Bragg reflectors coated using an optical thin film coater. The previously fabricated p-electrodes and n-electrodes are exposed by ICP etching and the p- and n-pads are deposited on top by electron beam evaporation. Finally, the fabricated wafer is diced into $1 \times 1 \times 0.21$ mm^3 optoelectronic chips by laser micromachining. The flip-chip is attached to the printed circuit board by soldering.
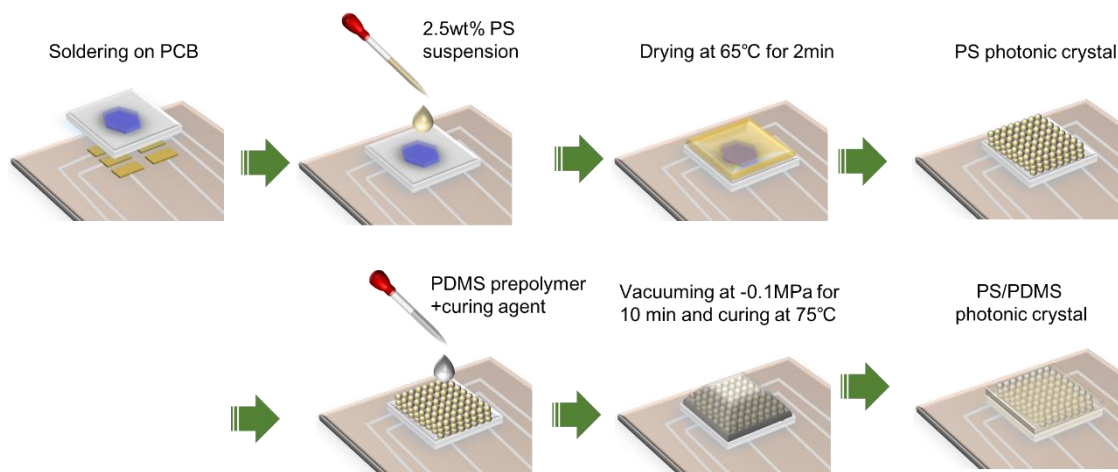
Figure 5.1 Schematic diagram showing the fabrication process of optoelectronic nose.

Monodisperse polystyrene (PS) microspheres suspension with a particle size of 180 nm is purchased from Rigor Biotechnology Co., Ltd. (Wuxi, China). The PS microspheres are dispersed in pure water at a mass fraction of 2.5 wt.% without further treatment. The preparation process of the optoelectronic nose is shown in Figure 5.1. After soldering the chip onto the PCB, a micropipette is used to take 2.0 μL of PS dispersion and add it vertically dropwise onto the sapphire of the flip-chip. The chip is placed on a heating plate at 65 ℃ and dried for 2 min until the water evaporates completely, leaving a self-assembled PS film of ~32.0 μm thickness on the surface of the sapphire. The PDMS prepolymer and the curing agent are mixed in a 10:1 ratio and a drop of the mixture is applied to the PS film with a needle tip and spread evenly over the surface. The chip is placed in a vacuum vessel at -0.1MPa for 10 minutes to ensure that the PDMS mixture penetrated into the gaps of the self-assembled PS film. Finally, the PDMS is cured at 75 ℃ to obtain an optoelectronic nose anchored with a PDMS wrapped PS photonic crystal.
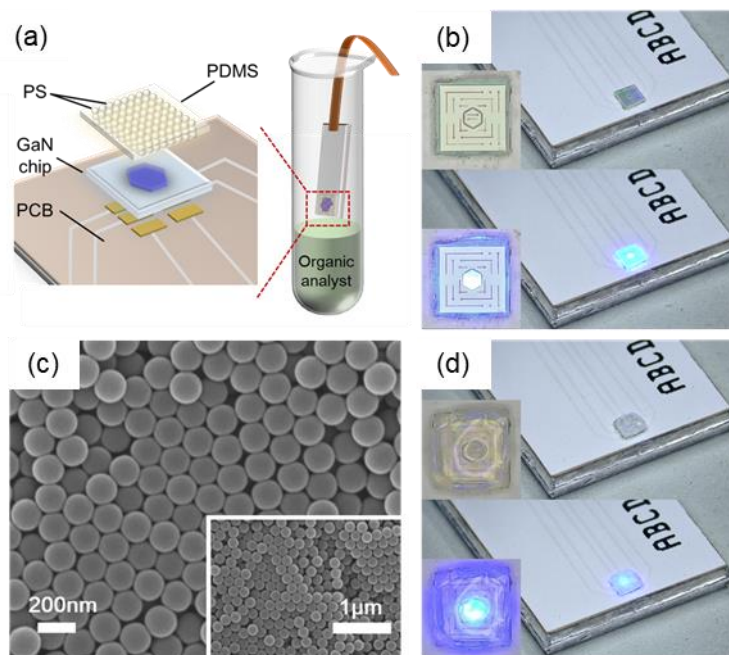
Figure 5.2 (a) Schematic of the structural of the optoelectronic nose. Digital photographs of the unilluminated and illuminated chip (b) before and (c) after combined with photonic crystal with a viewing angle of 45 °. The insets are from an overhead view. (d) SEM images of the PS self-assembled structure.

The structure of the optoelectronic nose is illustrated in Figure 5.2 (a), with a GaN-based optoelectronic chip mounted upside down on a printed circuit board and a PDMS-coated PS photonic crystal assembled on the sapphire surface of the chip. For the identification of the organic compounds, the optoelectronic nose is merely placed close to the surface of liquid and interacts with the volatile gas without contaminating the chemical to be measured. The optoelectronic chip consists of two parts, the LED and the PD. The light-emitting area is designed as a hexagon with a side length of 160 μm in the center of the chip, while the outer area assumes the role of the PD. Figure 5.2 (b) visualizes the bare GaN chip in its unlit and lit state. The Scanning electron microscopy

(SEM) images show a high-resolution view of the PS self-assembled structure (Figure 5.2 (c)). The microspheres are arranged in a tightly packed hexagonal structure, with each sphere being tightly connected to its six nearest neighbors. Such arrangement of PS microspheres plays a crucial role in determining the photonic crystal structure of the microspheres. According to previous research, the face-centered cubic (FCC) structure allows for a regular arrangement between the microspheres, resulting in a perfectly periodic structure of the photonic crystal and thus a significant optical band gap effect. Specifically, when the frequency of the light wave is at the Bragg reflection condition of the medium, the light wave is reflected back by the periodic structure of the lattice, thus forming an optical band gap in the medium. For light waves in other frequency ranges, the Bragg reflection condition is not met and they are confined outside the optical band gap. This optical band gap effect allows photonic crystals to selectively reflect or transmit different wavelengths of light, resulting in a specific color and optical effect. As a result, the PDMS-coated photonic crystal appears translucent and reflects a blue-violet luster, which can be observed in Figure 5.2 (d), close to the color of the light emitted by the LED. Besides, the PS microspheres self-assemble on the sapphire surface of the chip by evaporation. The outward flow of solvent during evaporation causes particles to accumulate at the edges of the droplets, resulting in a raised "coffee ring" around the chip [103].

5.3 Theory calculation and simulation of organic-sensitive photonic crystal

The structure of photonic crystals has a periodic refractive index distribution,

which allows the light of only specific wavelengths to be Bragg-reflected in photonic crystals, while other wavelengths are diffracted, refracted or scattered and eventually absorbed or diffused out. Thus, the wavelength range of light reflected by a photonic crystal can be selected by adjusting the structure of the photonic crystal. An array of photonic crystals can be considered as consisting of dielectric sphere and dielectric medium, obeying both Bragg's law and Snell's law of refraction. Bragg's law is modified to equation 5.1, where m is the order of reflection, λ is the wavelength of the reflected light, d is the distance between particle planes, n_{eff} is the average effective RI, and θ is the angle between the incident light and the normal to the interface [104, 105]. For (111) plane of the FCC lattice, the reflected wavelength is derived from the relationship between the cell parameters, particle size and crystal face spacing in equation 5.2. Where D is the center-to-center distance between the particles, n and V are the RI and the volume fraction of each component phase.

$$\lambda=2d(n_{eff}^2-\sin^2\theta)^{\frac{1}{2}}$$
5.1

$$\lambda=2\sqrt{\frac{2}{3}}D(\sum_i n_i^2 V_i)^{\frac{1}{2}}$$

5.2

In this work, the dielectric sphere of the photonic crystal is PS microsphere of size 180 nm (D=180 nm n_1=1.59 V_1=74%) and the dielectric medium is PDMS (n_2=1.40 V_2=26%). Thus, the theoretical wavelength of reflected light from the photonic crystal can be obtained as ~452nm.

PDMS, as an elastic silicone material, consists mainly of -Si-O- and -CH$_3$ groups.

At room temperature and pressure, humidity does not affect the photonic crystal due to the hydrophobic effect of $-(O-Si(CH_3)_2)$ groups on the PDMS surface. When PDMS comes into contact with organic gas, the guest molecules are adsorbed by the PDMS groups and the molecular chains are stressed which in turn triggers the volume expansion of the PDMS [106]. According to previous studies, the swelling behavior of PDMS is related to molecular cohesive energy [107]. The cohesion energy of organic vapors is separated into three components: dispersion interactions (δ_d), dipolar interactions (δ_p) and hydrogen bonding interactions (δ_h), referred to as Hansen solubility parameters (HSPs). Aside from HSPs, vapor pressure is another element that affects PDMS swelling [108]. An equation 5.3 was proposed by Rumens et al [109]. to quantify the swelling ratio of PDMS (Q_V) by combining HSPs and vapor pressure.

$$Q_V = a + (b_{\delta d} \times \delta_d) + (b_{\delta p} \times \delta_p) + (b_{\delta h} \times \delta_h) + (b_{Pvp} \times P_{vp}) \qquad 5.3$$

where a is the calculated constant, b is the calculated constant from each independent variable, P_{vp} is the vapor pressure.

Due to the weak intermolecular forces between the groups and the organic molecules, the organic molecules will come out of the organic gas environment and the PDMS will return to its original state. In PDMS-PS photonic crystals, the expansion of the PDMS by interaction with organic molecules triggers a change in the spacing of the PS microspheres, which in turn changes the wavelength reflected by the photonic crystal. It is true that the interaction with organic molecules leads to a change in the effective refractive index of the photonic crystal, but previous studies have shown that this change is too small to cause a significant redshift in the reflectance spectrum. In

addition, the PDMS matrix acts as a "receiver" for the organic analyte, but also as a "buffer" to protect the self-assembled PS structure from direct organic stimuli, enabling the repeated use of the photonic crystal-sensitive film.

The finite-difference time-domain (FDTD) method is employed to explore the reflectance behavior of photonic crystal sensitive film. Given that the self-assembled PS film thickness of around 32 μm corresponds to 200-210 layers of PS nanospheres, the simulation model is designed as 30-220 layers of PS nanospheres wrapped in PDMS. The simulation findings in Figure 5.3 (a) demonstrate that the reflectance is close to 100% for PS over 90 layers and does not vary considerably with layer number. With Gaussian fitting, the peak wavelength of the photonic crystal reflection peak is determined as 450nm, which is compatible with the experimental results. Furthermore, the reflectance spectra of the photonic crystal in the presence of PDMS solvation is investigated.
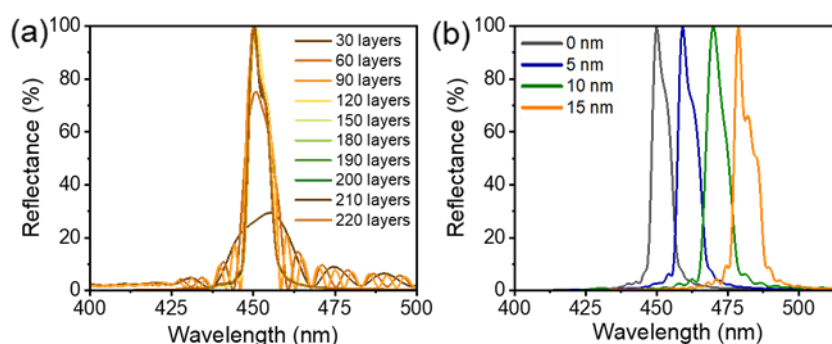
Figure 5.3 (a) The calculated reflectance spectra of PS nanosphere stacks with different layers. (b) The calculated reflectance spectra of 200-layer PS nanosphere with different spacing.
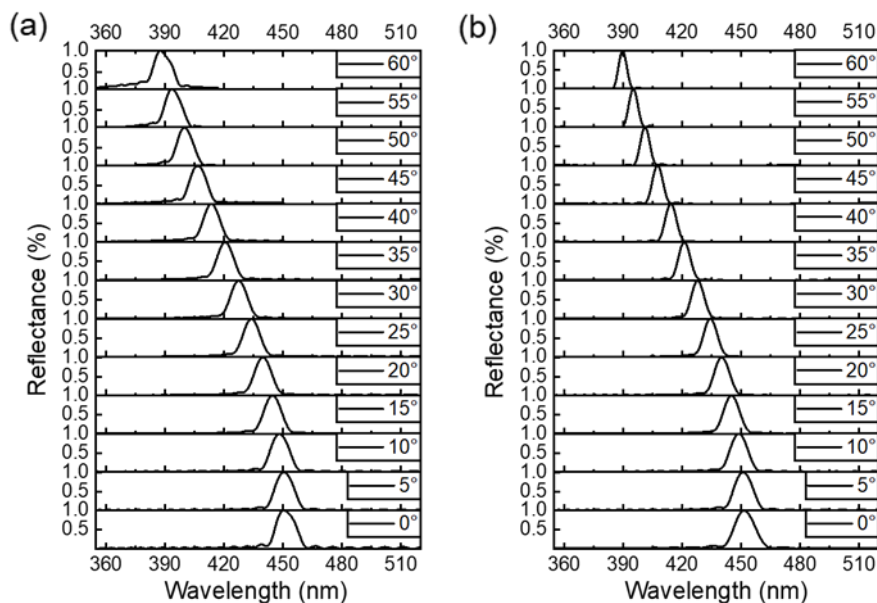
Figure 5.4 Plots of calculated reflectance as a function of wavelength for (a) TM and

(b) TE modes.

The reflectance peaks are simulated under the condition of 200-layer PS nanospheres stacking with a spacing of 0-15 nm, as shown in 5.3 (b). As the separation grows, the wavelength of the reflectance peaks gradually redshifts. The reflectance spectra of the photonic crystal redshift 9, 20 and 30 nm for PS nanosphere spacing of 5, 10 and 15 nm respectively, demonstrating that the increase in PS spacing produced by the dissolution of organic molecules when absorbed by PDMS does result in a reflectance redshift.

In addition, the wavelength of light reflected by the photonic crystal is related to the angle of light incidence. Based on the GaN-based device applied in this work, the angle of incidence was calculated to be between 0 ° and 57 °. Based on the 200-layer PS nanospheres simulation model, the reflectance characteristics of transverse electric (TE)

and transverse magnetic (TM) modes are calculated as a function of angle. As shown in Figure 5.4, the reflection peaks blueshift as the incident angle increases. Since the LED emission is omnidirectional, according to the simulation results, the reflected light from the photonic crystal received by the PD should be a broad peak with a wavelength between 380 nm and 460 nm.

5.4 Working principle of optoelectronic nose

Figure 5.5 illustrates the operative principle of the optoelectronic nose. Through current injection, carriers in the LED radiatively recombine to emit light in the MWQ. The light flows through the sapphire to the photonic crystal, where it is reflected and absorbed by the InGaN layer of PD, producing electron-hole pairs and generating photocurrents.
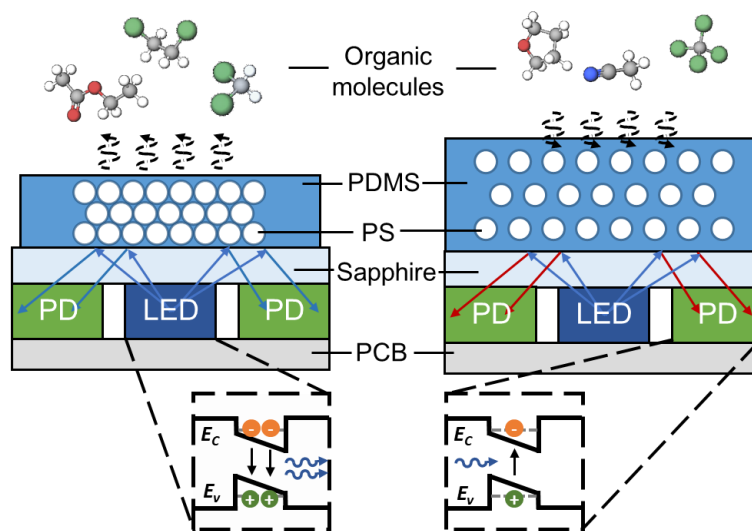
Figure 5.5 Schematic diagram of the working principle of the optoelectronic nose.

As the photonic crystal comes into touch with the organic gas, the PDMS expands, increasing the distance between PS beads and causing a redshift in the reflectance

spectrum. The region of overlap between the reflected and absorbed spectra diminishes, resulting in a weakening of the light intensity in the response spectrum and a decrease in photocurrent. Once the guest molecules have completely evaporated, the PDMS will shrink back, the reflected spectrum of photonic crystal gradually shifts to blue, and the area of spectral overlap and the PD photocurrent returns to its initial state.

5.5 Optical and electrical properties of GaN-based chip for optoelectronic nose
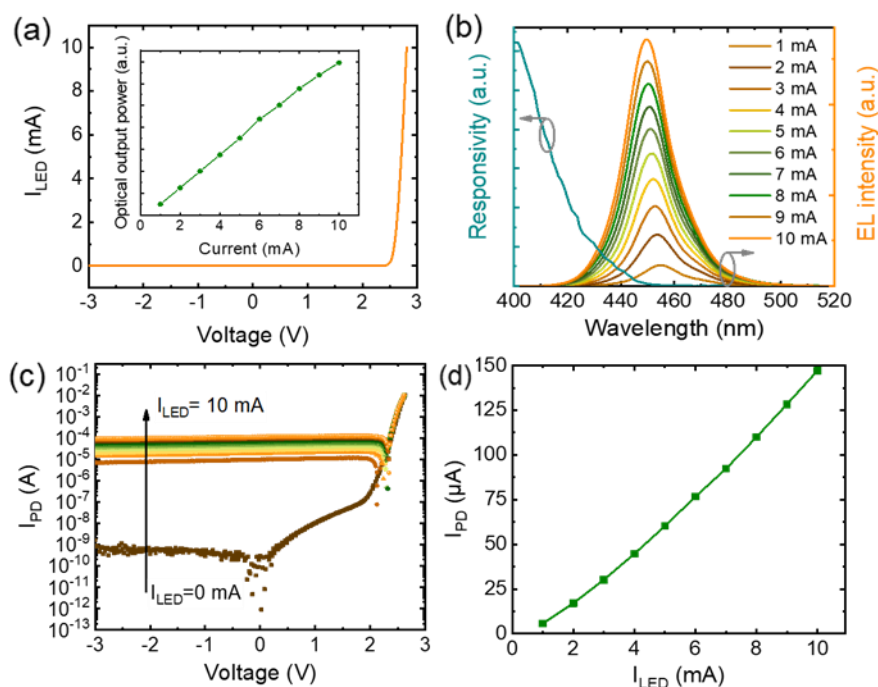
Figure 5.6 (a) The I-V properties of LED. The inset is the corresponding L-I curve. (b) The LED EL spectra while operated from 1 mA to 10 mA. And the PD responsiveness spectrum. (c) The I-V curves of PD at 0-10mA at LED injection current of 0-10mA. (d) The I_{LED}-I_{PD} plot in constant current mode.

For starters, LED and PD, as light-emitting and photodetecting components of an optoelectronic nose, are electrically and optically critical to the sensing performance.

The I-V curve of the LED is shown in Figure 5.6 (a). The forward bias voltage of the LED is 2.81V at an injection current of 10mA, and the turn-on voltage calculated from the I-V curve extension is 2.57V with a resistance of 41.5Ω based on the slope of the curve. The inset of Figure 5.6 (a) demonstrates that the light output power of the LED increases linearly with increasing current.

The luminescence of the LED is observed through the EL spectrum (Figure 5.6 (b)) and it is found that the EL intensity of the LED gradually increases as the input current increases. In addition, the peak wavelength of the LED gradually blue shifted as the drive current increases, due to the band gap-filling effect. The PD adopts the same epitaxial structure as the LED, and the response spectrum of the PD overlaps the LED emission spectrum by approximately 20 nm. Due to the quantum-confined Stark effect and the fluctuation of indium content in the MQWs, the responsivity of the PD gradually decreases with increasing wavelength, which is visualized by the spectral difference and band-tailing phenomenon. Further, the I-V curve of the PD is tested to probe the light detection capability of the PD (Figure 5.6 (c)). The dark current of the PD is kept at a depressed level of 10^{-9} A without the emitting light of LED. As the LED injection current increases, the photocurrent of the PD increases significantly. When the injection current rises to 10 mA, the photocurrent increases by four orders of magnitude to 10^{-5}-10^{-4} A. The large differential between photocurrent and dark current indicates the high sensitivity of the PD to the presence of emitter light. In addition, the stable reverse bias current proves that the leakage current of the PD can be neglected. Figure 5.6 (d) demonstrates that the photocurrent of PD shows a good linear relationship with

the LED injection current.

5.6 Sensing performance of optoelectronic nose
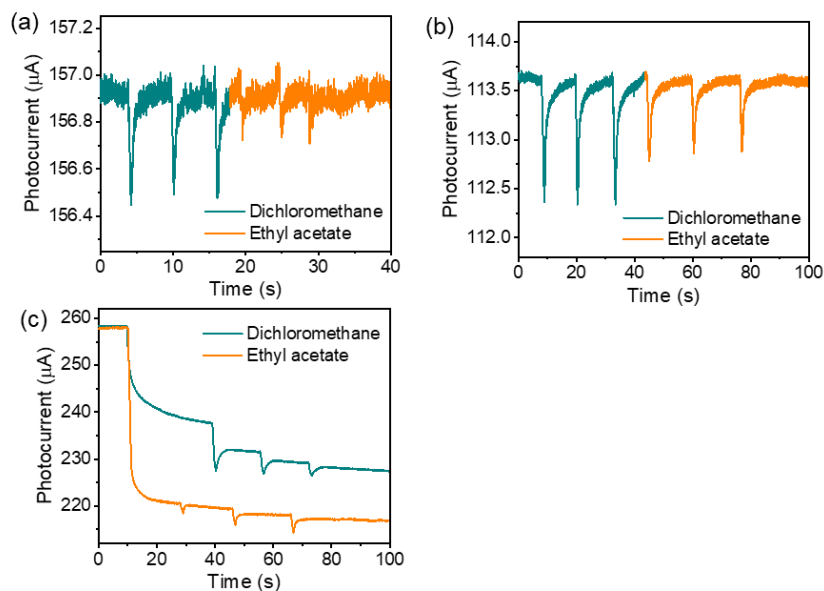
Figure 5.7 Photocurrent response of (a) bare chip, (b) PDMS film and (c) PS film to

dichloromethane and ethyl acetate.

The photocurrent responses of the bare chip to dichloromethane and ethyl acetate are examined firstly. As shown in Figure 5.7 (a), there are small decreases in photocurrent after exposure to both organic gases. Due to the condensation of the organics into tiny droplets on the sapphire surface, the organics-sapphire surface replaces the air-sapphire interface. The changes in the refractive index alter the degree of total reflection on the sapphire surface, which in turn leads to the decrease in photocurrent. Such a variation in the photocurrent of the bare chip is much smaller than that in the presence of the PDMS-coated PS photonic crystal film.

The photocurrent variations of the devices equipped PDMS film and PS film to organics are plotted in Figures 5.7 (b) and (c). For the device assembled with the PDMS

film, a gentle decrease in photocurrent has been observed since PDMS are caused a refractive index change under the solvation of the organics. Upon leaving the organic environment, the photocurrent recovered to the initial value, demonstrating the restoration of PDMS to the pristine state. In contrast, the device equipped with pure PS film showed a drastic decline in photocurrent after encountering organic gases with no recovery. Due to the dissolving effect of organics on PS, the lattice structure of pure PS photonic crystal could not be regained after being destroyed. This leads to a decrease in the reflectivity of the PS film, which causes an irreversible drop in the photocurrent. The three control groups demonstrated that neither the bare chip, the pure PDMS film, nor the pure PS film could enable the optoelectronic nose to recognize organics reversibly. In other words, the PDMS-PS photonic crystal is the essential component for the optoelectronic nose to be recognizable for organic gases.

The optical response of the photonic crystal to the selected organic substances is examined by using *in-situ* reflectance spectroscopy. As shown in Figures 5.8, all seven analytes have a red-shifted effect with an enhancement reflectance intensity on the photonic crystal when transiently exposed to the gas above the organic liquid. The photonic crystal reflectance peaks all mostly recover to their original condition after several seconds of removal from the organic environment, suggesting that the observed identification process is reversible.
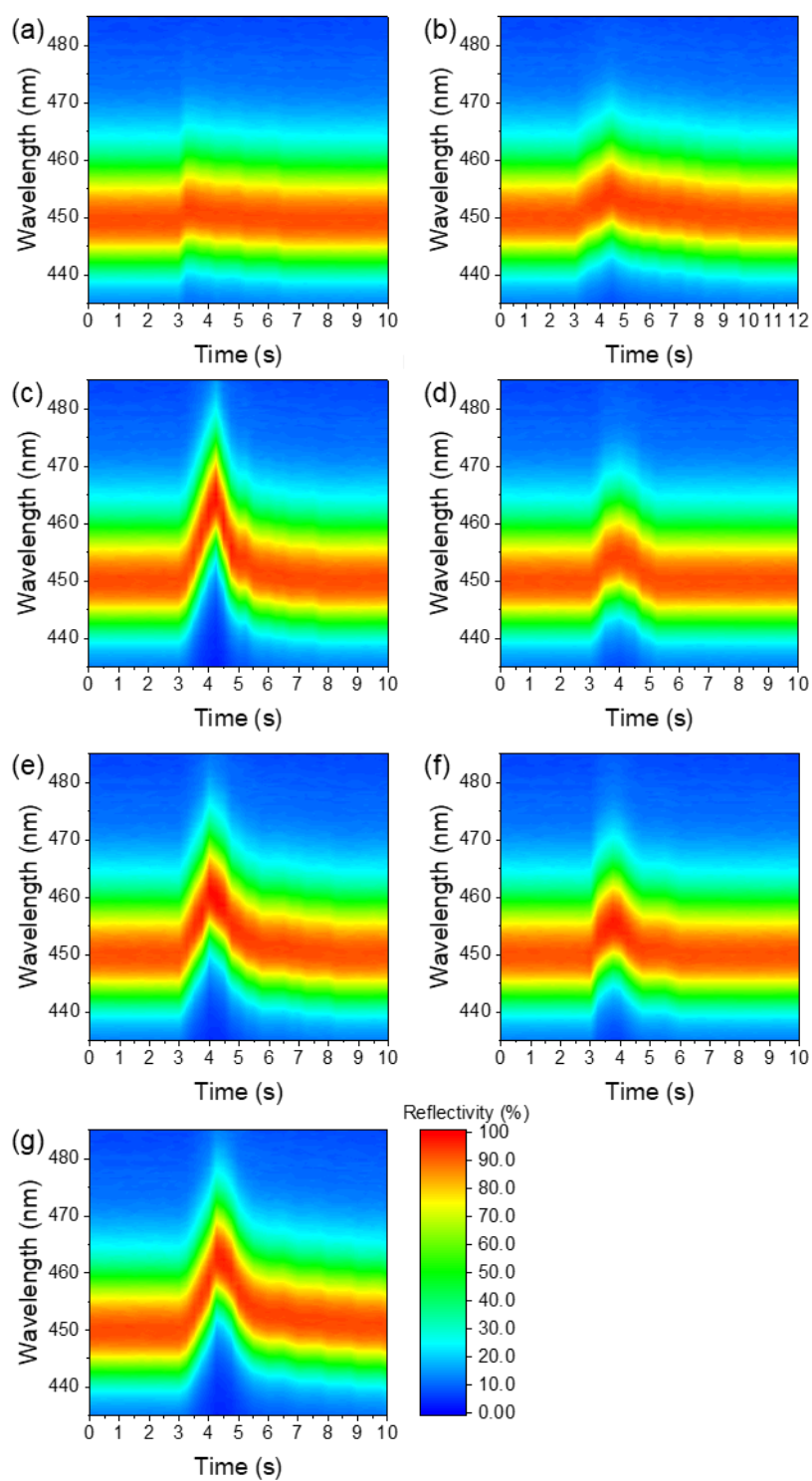
Figure 5.8 Reflectance spectra of photonic crystals during the adsorption and desorption of (a) methanol, (b) acetonitrile, (c) dichloromethane,(d)1,2-dichloroethane, (e) tetrachloromethane, (f) ethyl acetate, (g) tetrahydrofuran.
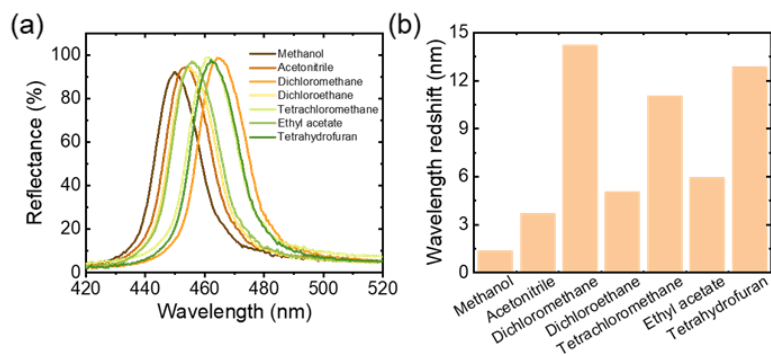
Figure 5.9 Plots of (a) reflectance spectra and (b) wavelength variations of photonic

crystals with the most significant alterations upon contact with different organic

gases.

Figure 5.9 summarizes the wavelength shifts when the photonic crystal comes into

contact with the seven organic gases to show the spectrum alterations more clearly. The

analysis shows that the seven organics can be well distinguished by the spectra.

Methanol has the smallest redshift of 1.37 nm, while dichloromethane shows an

extremely strong spectral shift reaching 14.23 nm. Dichloroethane and ethyl acetate

demonstrate similar effects with wavelength shifts of 5.06 nm and 5.96 nm respectively.

As previously stated, the magnitude of the spectral shift is positively correlated

with Q_V of the PDMS. The swelling of PDMS by organic gases has been classified into

three categories based on equation 5.3 and reported in the literature [109-111]: Non-

polar to weakly polar solvent vapors induce the greatest swelling ($Q_V > 2.0$), including

ethers, tetrahydrofuran, n-hexane and DCM. The least swelling ($Q_V = 1.0$-1.3) is caused

by polar solvent vapors, alcohols and acetonitrile. Other solvent vapors (similar to ethyl

acetate) produced moderate swelling volumes ($1.3 < Q_V < 2.0$). That is entirely

consistent with the observations of the present work.

After analyzing the photonic crystal spectrum response and the optical characteristics of the GaN chip, the assembled optoelectronic nose is used for the identification of guest organics. Specifically, 1 mL of the liquid to be measured is dropped into a 3 mL centrifuge tube, the optoelectronic nose is placed close to but not in touch with the liquid surface, at a distance of approximately 0.5 mm from the liquid surface, as illustrated in Figure 5.2 (a).
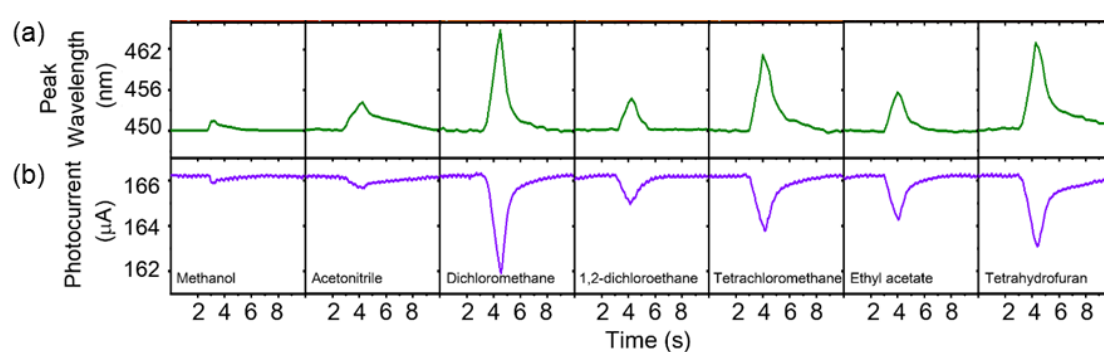
Figure 5.10 Visualizations of (a) photonic crystal wavelength shift and (b) optoelectronic nose photocurrent variety.

The optoelectronic nose is evacuated from the organic gas environment and put under normal atmospheric conditions after contact with the gas, and the change in photocurrent of the optoelectronic nose during the contact-exit from the organic gas is recorded. Further, the *in-situ* reflectance spectra of the photonic crystal are recorded by Gaussian fitting of the peak wavelength and peak reflectance curves with time and compared with the photocurrent variation, which is demonstrated in Figure 5.10. The contact time of the optoelectronic nose with each organic gas is standardized to the 3rd second. As seen in Figure 5.10, the spectral redshift and reflectance intensity peak after 1-2 seconds of gas exposure and then progressively recover. Moreover, the photocurrent

response is unified with the spectral change, the larger the spectral redshift, the greater the reduction in photocurrent.

To verify precision and repeatability, the optoelectronic nose is applied to continuous guest molecule recognition. Figure 5.11 (a) depicts the fluctuation in photocurrent with time for each analyte based on three measurements. When in contact with the same organic species, the optoelectronic nose displays the same trend of homogenous and steady photocurrent curves with high repeatability. At the same time, there is also difference in photocurrent variation for various organic vapors, which proves that the photoelectronic nose can distinguish between different organic vapors.
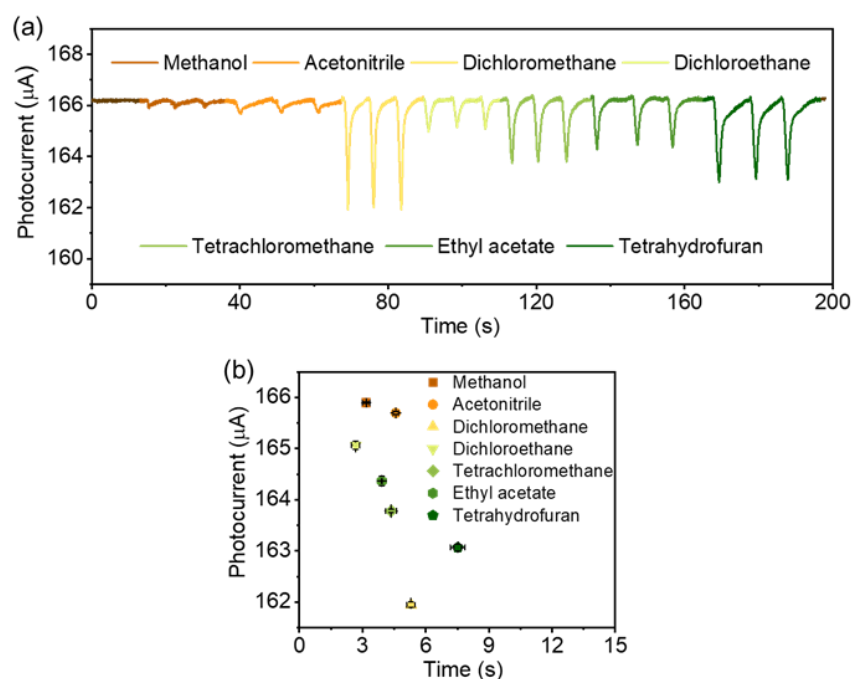
Figure 5.11 (a) Continuous photocurrent response for different organic gases. (b) Diagram of the recovery time-photocurrent response to different organic gases.

For optoelectronic noses, the photocurrent does not always give a significant enough difference to distinguish between analytes, such as methanol and acetonitrile.

The recovery period of the photocurrent is another key observable that can be utilized to distinguish between guest molecules with similar photocurrents. A "recovery time-photocurrent matrix" validation approach is employed to assess the predictability of the resulting sensor to further characterize its discriminating capacity. The mean values and errors of the measured photocurrents and recovery durations in Figure 5.11 (a) are analyzed, with the results summarized in Figure 5.11 (b). All analytes are sorted into well-defined clusters, confirming the precision of guest molecule identification, and acceptable error levels show the repeatability of optoelectronic nose sensing.

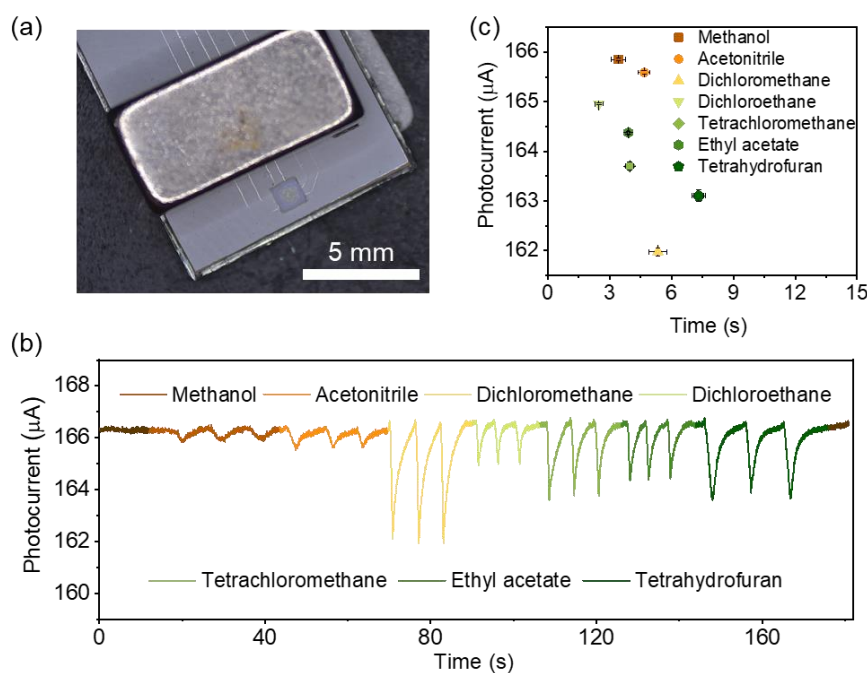Figure 5.12 (a) Optical image of optical device under the interference of magnet. (b) Continuous photocurrent response for different organic gases under the interference of magnet. (c) Diagram of the recovery time-photocurrent response to different organic gases under the interference of magnet.

In the electromagnetic immunity testing of the optoelectronic nose, a magnet

measuring $5 \times 5 \times 10$ mm^3 is affixed to the PCB surface to establish a magnetic environment. The photograph of the device is presented in Figure 5.12(a). As illustrated in Figure 5.12(b), the device exhibits a trend consistent with that of the non-magnetically interfered device shown in Figure 5.11(a). Data extracted and displayed in Figure 5.12(c) indicate that the response to organic compounds in a magnetic environment does not show significant changes, with both photocurrent and recovery time errors remaining within acceptable limits. Thus, the organic sensor demonstrates robust electromagnetic immunity and can operate stably in magnetic environments.

Table 5.1 Comparison with previously reported organic identification methods.

Sensitive materials	Sensing method	Sensor number	Number of target organics	Sensing Time	Ref.
UiO-66	Reflection spectra variation	1	5	5s	[112]
ZIF-8 with Nile red	Fluorescence detection	1	6	-	[113]
Photonic crystal based on PMMA and methylcellulose	Colorimetric method	1	5	-	[114]
ZIF-8	Colorimetric method	1	6	1000s	[115]
ZIF-8 of different morphologies	Colorimetric method	3	4+3+8*	350s	[116]
Photonic crystal based on PDMS and PS	Optoelectronic method	1	7	<60s	This work

* The three sensors correspond to four, three and eight target molecules respectively.

In Table 5.1, the optoelectronic nose developed in this study is compared with various recent optical-based organic identification methods. Previous research used spectrum monitoring approaches with shorter sensing durations but larger analytical

devices. The fluorescence detection requires cost-consuming instruments while the colorimetric method needs more time for the large molecules adsorption by ZIF-8. This work is highly competitive in terms of analysis time, number of target molecule species, accuracy and cost, and demonstrates the excellent potential of optoelectronic noses for organic identification. In addition, the optoelectronic nose outperforms previously described E-noses and P-noses in various ways. Firstly, the optical properties of the photonic crystal are derived from its periodic structure, avoiding the issue of quenching by an applied fluorescent agent. Besides that, the monolithic integrated LED-PD optoelectronic device minimizes the size of the external light source and detector, while also reducing cost and power consumption. Most all, the prepared photonic nose is easy to use and reusable, reducing the requirement for users to handle multiple liquids in organic exposures and offering excellent potential for industrial and environmental testing.

5.7 Conclusion

In summary, we have design a photonic crystal-based optoelectronic nose that provides accurate and reliable identification of volatile organic compounds. The optoelectronic nose consists of a photonic crystal sensitive film and a GaN-based integrated optoelectronic chip, which is capable of selectively interacting with gas molecules, resulting in a change in the reflectance spectrum of the photonic crystal. The change in the overlap between the reflectance spectrum of the photonic crystal and the absorption spectrum of the optoelectronic chip is then used to fingerprint and

characterize the substance to be measured by the change in the optoelectronic signal, which can be used to identify the specific gas present. The optoelectronic nose offers numerous significant benefits over conventional organic compounds detection technologies, including low cost, tiny sensor size, sub-minute response time, high accuracy of fingerprinting determination and low interference from environmental factors. In addition, the optoelectronic nose is a non-invasive sensing approach that eliminates the need for costly and time-consuming laboratory analysis. The optoelectronic nose, as an ideal tool for applications such as environmental monitoring and industrial safety, provides a powerful solution that may assist limit the potential hazards of organic exposure and enhance overall safety in industrial environments.

Chapter 6 Conclusions and Outlook

6.1 Conclusions

In this thesis, three monolithic integrated flip-chip GaN LED-PD optoelectronic devices are designed and fabricated. The working principle, optical characteristics and electrical characteristics of each monolithic integrated device are investigated. The principle and performance of each sensor in liquid property detection are specifically analyzed. The thesis is summarized here as follows.

Firstly, the GaN LED-PD device with monolithic integration is designed according to the working principle of GaN-based LEDs and PDs. The structure of this GaN-based chip is proposed based on energy band theory and Stokes shift theory. The two types of photonic units, light emitting and detection, are fabricated on the same sapphire substrate GaN wafer containing InGaN/GaN MQWs, which can achieve both light emitting and detection functions at the same time. The overlap of the emission and absorption spectra of the same MQWs allows PDs to always respond to the optical signals of homogeneous light-emitting diodes in devices fabricated with the same epitaxial structure. In the design of monolithic flip-chip LED-PD devices, it is necessary to simultaneously consider the interaction between the PD and the LED, the overall size of the device, and the feasibility of preparation and packaging. Once the appropriate package design has been completed, the optical characteristics, electrical characteristics and optical coupling mechanism of the devices should be tested and analyzed. The optical and electrical properties of LEDs and PDs of flip-chip devices

are investigated by basic characteristics such as I-V curves, IPD-ILED curves, EL spectral curves and so on. The results show that the monolithic integrated LED-PD device can realize the self-response of the PDs to the LEDs, and the induced photocurrent of the PDs is linearly related to the driving current of the LEDs. Meanwhile, the wafer-level device preparation process can produce hundreds of homogeneous chips on a single wafer, miniaturizing and reducing production costs. Performance testing of the devices shows that the three systems-on-the-chip are compact, functionally complete and feature high sensitivity, high performance, high resolution, high reliability and low power consumption.

Next, the device with a centrosymmetric pattern of LED-PD is applied for droplet detection. In this droplet sensor, the device is encapsulated with the biocompatible waterproof material PDMS as a waterproof layer, and the exposed sapphire is used directly as the sensing interface. The high refractive index of sapphire allows the light emitted from the LED to undergo a total reflection phenomenon at the sapphire-air interface, which is reflected back to the PD to generate a photocurrent. The sapphire-air interface is replaced by the sapphire-droplet interface when the droplet adheres to the sapphire surface. The presence of liquid droplets reduces the amount of light returned to the PD by total reflection, resulting in a decrease in photocurrent. The response time of the device is only 3.88 μs in the optoelectronic performance test, proving that the droplet sensor has the ability to detect droplets quickly. The droplet sensor can now be used to monitor the flow rate of infusion devices. The continuous frequency conversion test proves that the assembled droplet sensor can monitor droplets

with frequencies up to 3 Hz. In addition, the proposed LED-PD device has the advantages of low cost, compact structure, robustness and simple operation, which is very suitable for the practical application of droplet detection.

In addition, the GaN LED PD chip mounted with indicator film is used for liquid pH detection. According to the optical characteristic measurement, the device responds to the light with a wavelength of 415-445 nm. Therefore, if the mounted indicator film has a variation of reflectance spectrum at 415-445 nm, it would match the response range of the chip. The amount of light reaching the PD is adjusted according to the reflectance response of the indicator film at different pH. The pH tests have shown that the photocurrent of the device has a linear response over a wide range of pH in the range 5-13. A fast response time of 3.8 s and a sample volume of 1 μL enable on-site detection and reduce sample loss. Repeatability measurement and ion interference test prove that the assembled pH sensor has the characteristics of anti-interference, high repeatability and low error, demonstrating good performance for practical applications. Such a pH sensor improves the accuracy of pH identification based on the traditional indicator colorimetric method, and at the same time avoids the problem of complicated operation of the fiber-optic pH meter with redundant external equipment.

Finally, a GaN LED-PD chip with a central wavelength of 450 nm is integrated with a thin film of photonic crystal to develop an optoelectronic nose targeting the recognition of organic liquids. Due to the special periodic nanostructures of the photonic crystal, the photonic crystal film can selectively reflect light at specific wavelengths. Simulations and reflectivity measurement demonstrate that the peak

reflection wavelength of the selected PDMS-PS photonic crystal is 450 nm, which corresponds to the center wavelength of GaN-based LED and the operating wavelength range of PD. PDMS undergoes different degrees of volume reversible changes upon exposure to different organic gases, which triggers changes in the structure of the PDMS-PS photonic crystal and in the wavelength of the reflected light. The change in the amount of reflected light leads to a change in the photocurrent, which allows for the specific identification of organic gases. In addition, the small size and low energy consumption of the optoelectronic nose can expand the range of applications and reduce the cost of use, which is conducive to industrial applications. This work is of great significance for the detection of hazardous gases in the air of relevant workplaces, health protection of workers, environmental protection and accident prevention.

6.2 Outlook

With the improvement of process level and application requirements, the research on GaN based optoelectronic devices tends to be miniaturized, arrayed, integrated and flexible. The research in this thesis has the characteristics of miniaturization and integration, but does not include LED arrays and flexible electronics. Also, the proposed sensors still rely on photocurrent comparison for data analysis and cannot be read directly. The outlooks for future research are proposed here:

By improving the design of the mask plate and chip structure, the detection range and response capability of the device can be enhanced by expanding from a single-chip structure to an array structure, which can be extended to a wider range of application scenarios while improving the sensing performance. In particular, applying the array

structure to the optoelectronic nose can expand the types of organic liquids that can be detected. When the optoelectronic chip array is combined with a droplet sensor, different drugs can be detected while monitoring the flow rate of the infuser.

Flexible materials can be used as substrates, combined with micro-nano processing technology or 3D printing fabrication technology, to produce flexible optoelectronic sensing devices. Flexible electronic devices feature thinness, low power consumption, good biocompatibility and tunable mechanical properties, etc. They can be attached to the human skin for a long time without interfering with daily activities, and can continuously monitor the health status of the human body anytime and anywhere. The multiple sensors proposed in this thesis can be combined with flexible materials to achieve wearable on-site fluid analysis by optimizing the system interface.

Sensor data processing relies on manual calculation, which is time-consuming and labor-intensive, so the sensor results can be obtained directly through machine learning. Compared to manual data processing, machine learning algorithms have higher processing speed and efficiency. When processing and analyzing large amounts of data, machine learning algorithms enable faster calculations and predictions, which can significantly reduce the time needed to analyze data and make decisions. Implementing machine learning allows computers to automatically learn from data and make predictions or decisions without being explicitly programmed to do so, reducing data processing time during collection.

Data collection in this thesis relies on wires and source meters, which cannot be directly applied to wearable devices. Wireless monitoring can be achieved by

attempting to combine the device with a Bluetooth module and using Bluetooth technology to upload the data to a computer or mobile phone before data analysis and processing. This will provide better portability and a wider range of services for wearable devices.

Reference

[1]   F. Roccaforte *et al.*, "Emerging trends in wide band gap semiconductors (SiC and GaN) technology for power devices," *Microelectronic Engineering,* vol. 187-188, pp. 66-77, 2018/02/05/ 2018, doi: 10.1016/j.mee.2017.11.021.

[2]   M. Abdel-Baki and F. El-Diasty, "Optical properties of oxide glasses containing transition metals: Case of titanium- and chromium-containing glasses," *Current Opinion in Solid State and Materials Science,* vol. 10, no. 5, pp. 217-229, 2006/10/01/ 2006, doi: 10.1016/j.cossms.2007.08.001.

[3]   J. W. Precker, "Simple experimental verification of the relation between the band-gap energy and the energy of photons emitted by LEDs," *European Journal of Physics,* vol. 28, no. 3, p. 493, 2007/03/23 2007, doi: 10.1088/0143-0807/28/3/010.

[4]   H. Amano, M. Kito, K. Hiramatsu, and I. Akasaki, "P-Type Conduction in Mg-Doped GaN Treated with Low-Energy Electron Beam Irradiation (LEEBI)," *Japanese Journal of Applied Physics,* vol. 28, no. 12A, p. L2112, 1989/12/01 1989, doi: 10.1143/JJAP.28.L2112.

[5]   S. Nakamura, T. Mukai, and M. Senoh, "Candela‐class high‐brightness InGaN/AlGaN double‐heterostructure blue‐light‐emitting diodes," *Applied Physics Letters,* vol. 64, no. 13, pp. 1687-1689, 1994, doi: 10.1063/1.111832.

[6]   R. A. Yotter and D. M. Wilson, "A review of photodetectors for sensing light-

emitting reporters in biological systems," *IEEE Sensors Journal,* vol. 3, no. 3, pp. 288-303, 2003, doi: 10.1109/JSEN.2003.814651.

[7]   E. V. Gorokhov, A. N. Magunov, V. S. Feshchenko, and A. A. Altukhov, "Solar-blind UV flame detector based on natural diamond," *Instruments and Experimental Techniques,* vol. 51, no. 2, pp. 280-283, 2008/03/01 2008, doi: 10.1134/S002044120802022X.

[8]   G. Chai, O. Lupan, L. Chow, and H. Heinrich, "Crossed zinc oxide nanorods for ultraviolet radiation detection," *Sensors and Actuators A: Physical,* vol. 150, no. 2, pp. 184-187, 2009/03/25/ 2009, doi: 10.1016/j.sna.2008.12.020.

[9]   R. Bogue, "Sensors for fire detection," *Sensor Review,* vol. 33, no. 2, pp. 99-103, 2013, doi: 10.1108/02602281311299635.

[10]   S. J. Young *et al.*, "ZnO-based MIS photodetectors," *Sensors and Actuators A: Physical,* vol. 135, no. 2, pp. 529-533, 2007/04/15/ 2007, doi: 10.1016/j.sna.2006.10.001.

[11]   P.-C. Chang *et al.*, "High UV/visible rejection contrast AlGaN/GaN MIS photodetectors," *Thin Solid Films,* vol. 498, no. 1, pp. 133-136, 2006/03/01/ 2006, doi: 10.1016/j.tsf.2005.07.094.

[12]   M. Razeghi and A. Rogalski, "Semiconductor ultraviolet detectors," *Journal of Applied Physics,* vol. 79, no. 10, pp. 7433-7473, 1996, doi: 10.1063/1.362677.

[13]   Q. Chen *et al.*, "Schottky barrier detectors on GaN for visible–blind ultraviolet detection," *Applied Physics Letters,* vol. 70, no. 17, pp. 2277-2279, 1997, doi: 10.1063/1.118837.

[14] A. Osinsky *et al.*, "Low noise p-π-n GaN ultraviolet photodetectors," *Applied Physics Letters,* vol. 71, no. 16, pp. 2334-2336, 1997, doi: 10.1063/1.120023.

[15] Z. Jiang *et al.*, "Monolithic integration of nitride light emitting diodes and photodetectors for bi-directional optical communication," *Opt. Lett.,* vol. 39, no. 19, p. 5657, 2014.

[16] Y. D. Jhou *et al.*, "Nitride-based light emitting diode and photodetector dual function devices with InGaN/GaN multiple quantum well structures," *Solid-State Electronics,* vol. 49, no. 8, pp. 1347-1351, 2005/08/01/ 2005, doi: 10.1016/j.sse.2005.06.002.

[17] L. W. Ji, S. J. Young, C. H. Liu, W. Water, T. H. Meen, and W. Y. Jywe, "Nitride-based light-emitter and photodiode dual function devices with InGaN/GaN multiple quantum dot structures," *Journal of Crystal Growth,* vol. 310, no. 10, pp. 2476-2479, 2008/05/01/ 2008, doi: 10.1016/j.jcrysgro.2008.01.028.

[18] K. H. Li, H. Lu, W. Y. Fu, Y. F. Cheung, and H. W. Choi, "Intensity-Stabilized LEDs With Monolithically Integrated Photodetectors," *IEEE Transactions on Industrial Electronics,* vol. 66, no. 9, pp. 7426-7432, 2019, doi: 10.1109/TIE.2018.2873522.

[19] A. Mishra, A. Sudhakar, B. Jithender, and N. C, "AGRICULTURE & FOOD: e-Newsletter Volume 1 -Issue 7 - Applications of light emitting diodes for post-harvest quality management of fruits and vegetables," 07/01 2019.

[20] R. W. Martin, P. G. Middleton, K. P. O'Donnell, and W. Van der Stricht,

"Exciton localization and the Stokes' shift in InGaN epilayers," *Applied Physics Letters,* vol. 74, no. 2, pp. 263-265, 1999, doi: 10.1063/1.123275.

[21]   K. H. Li *et al.*, "InGaN RGB Light-Emitting Diodes With Monolithically Integrated Photodetectors for Stabilizing Color Chromaticity," *IEEE Transactions on Industrial Electronics,* vol. 67, no. 6, pp. 5154-5160, 2020, doi: 10.1109/TIE.2019.2926038.

[22]   Z. Shi, J. Yuan, S. Zhang, Y. Liu, and Y. Wang, "Simultaneous dual-functioning InGaN/GaN multiple-quantum-well diode for transferrable optoelectronics," *Optical Materials,* vol. 72, pp. 20-24, 2017/10/01/ 2017, doi: 10.1016/j.optmat.2017.05.039.

[23]   J. W. Lee, B. U. Ye, Z. L. Wang, J.-L. Lee, and J. M. Baik, "Highly-sensitive and highly-correlative flexible motion sensors based on asymmetric piezotronic effect," *Nano Energy,* vol. 51, pp. 185-191, 2018/09/01/ 2018, doi: 10.1016/j.nanoen.2018.06.059.

[24]   Y. Peng *et al.*, "Achieving high-resolution pressure mapping via flexible GaN/ZnO nanowire LEDs array by piezo-phototronic effect," *Nano Energy,* vol. 58, pp. 633-640, 2019/04/01/ 2019, doi: 10.1016/j.nanoen.2019.01.076.

[25]   Y. Peng *et al.*, "Self-powered high-performance flexible GaN/ZnO heterostructure UV photodetectors with piezo-phototronic effect enhanced photoresponse," *Nano Energy,* vol. 94, p. 106945, 2022/04/01/ 2022, doi: 10.1016/j.nanoen.2022.106945.

[26]   X. Gao *et al.*, "Wireless light energy harvesting and communication in a

waterproof GaN optoelectronic system," *Communications Engineering,* vol. 1, no. 1, p. 16, 2022/07/07 2022, doi: 10.1038/s44172-022-00016-5.

[27]   F. M. Stürner *et al.*, "Compact integrated magnetometer based on nitrogen-vacancy centres in diamond," *Diamond and Related Materials,* vol. 93, pp. 59-65, 2019/03/01/ 2019, doi: 10.1016/j.diamond.2019.01.008.

[28]   J. L. Webb *et al.*, "Detection of biological signals from a live mammalian muscle using an early stage diamond quantum sensor," *Scientific Reports,* vol. 11, no. 1, p. 2412, 2021/01/28 2021, doi: 10.1038/s41598-021-81828-x.

[29]   R. K. Joshi, J. E. Weber, Q. Hu, B. Johnson, J. W. Zimmer, and A. Kumar, "Carbon monoxide sensing at room temperature via electron donation in boron doped diamond films," *Sensors and Actuators B: Chemical,* vol. 145, no. 1, pp. 527-532, 2010/03/04/ 2010, doi: 10.1016/j.snb.2009.12.070.

[30]   C. Lu, Y. Li, S. Tian, W. Li, J. Li, and C. Gu, "Enhanced gas-sensing by diamond nanoneedle arrays formed by reactive ion etching," *Microelectronic Engineering,* vol. 88, no. 8, pp. 2319-2321, 2011/08/01/ 2011, doi: 10.1016/j.mee.2011.02.074.

[31]   K. O. Ho, Y. Shen, Y. Y. Pang, W. K. Leung, N. Zhao, and S. Yang, "Diamond quantum sensors: from physics to applications on condensed matter research," *Functional Diamond,* vol. 1, no. 1, pp. 160-173, 2021/01/02 2021, doi: 10.1080/26941112.2021.1964926.

[32]   B. S. Miller *et al.*, "Spin-enhanced nanodiamond biosensing for ultrasensitive diagnostics," *Nature,* vol. 587, no. 7835, pp. 588-593, 2020/11/01 2020, doi:

10.1038/s41586-020-2917-1.

[33]   W. Liu *et al.*, "Silicon-Vacancy Nanodiamonds as High Performance Near-Infrared Emitters for Live-Cell Dual-Color Imaging and Thermometry," *Nano Letters,* vol. 22, no. 7, pp. 2881-2888, 2022/04/13 2022, doi: 10.1021/acs.nanolett.2c00040.

[34]   Y. Hou *et al.*, "A Versatile, Incubator-Compatible, Monolithic GaN Photonic Chipscope for Label-Free Monitoring of Live Cell Activities," *Advanced Science,* vol. 9, no. 17, p. 2200910, 2022/06/01 2022, doi: 10.1002/advs.202200910.

[35]   L. Chen, Y. P. Wu, and K. H. Li, "Monolithic InGaN/GaN photonic chips for heart pulse monitoring," *Opt. Lett.,* vol. 45, no. 18, pp. 4992-4995, 2020/09/15 2020, doi: 10.1364/OL.400733.

[36]   J. Yan *et al.*, "Reflection-type photoplethysmography pulse sensor based on an integrated optoelectronic chip with a ring structure," *Biomed. Opt. Express,* vol. 12, no. 10, pp. 6277-6283, 2021/10/01 2021, doi: 10.1364/BOE.437805.

[37]   J. Yin *et al.*, "A Miniature GaN Chip for Surface Roughness Measurement," *IEEE Transactions on Electron Devices,* vol. 68, no. 10, pp. 4977-4981, 2021, doi: 10.1109/TED.2021.3105077.

[38]   J. Jing, X. An, Y. Luo, L. Chen, Z. Chu, and K. H. Li, "A Compact Optical Pressure Sensor Based on a III-Nitride Photonic Chip with Nanosphere-Embedded PDMS," *ACS Applied Electronic Materials,* vol. 3, no. 5, pp. 1982-1987, 2021/05/25 2021, doi: 10.1021/acsaelm.1c00130.

[39]   Y. Luo, X. An, L. Chen, and K. H. Li, "Chip-scale optical airflow sensor," *Microsystems & Nanoengineering,* vol. 8, no. 1, p. 4, 2022/01/04 2022, doi: 10.1038/s41378-021-00335-1.

[40]   L. Chen, X. An, J. Jing, H. Jin, Z. Chu, and K. H. Li, "Ultracompact Chip-Scale Refractometer Based on an InGaN-Based Monolithic Photonic Chip," *ACS Applied Materials & Interfaces,* vol. 12, no. 44, pp. 49748-49754, 2020/11/04 2020, doi: 10.1021/acsami.0c13144.

[41]   J. Chen, L. Chen, L. Zhu, X. Zhang, and K. H. Li, "Simultaneous Curing and Monitoring of Resin Using GaN Chips," *IEEE Sensors Letters,* vol. 6, no. 4, pp. 1-4, 2022, doi: 10.1109/LSENS.2022.3144998.

[42]   J. Chen, J. Yin, X. An, L. Chen, L. Zhu, and K. H. Li, "III-Nitride Microchips for Sugar Concentration Detection," *IEEE Sensors Journal,* vol. 22, no. 3, pp. 2078-2082, 2022, doi: 10.1109/JSEN.2021.3138746.

[43]   X. An, L. Chen, J. Li, Q. Wang, and K. H. Li, "Compact GaN-Based Photonic Chip for In Situ Real-Time Monitoring of Low Water Content in Ethanol," *ACS Applied Electronic Materials,* vol. 2, no. 11, pp. 3502-3507, 2020/11/24 2020, doi: 10.1021/acsaelm.0c00794.

[44]   X. An, H. Yang, Y. Luo, Z. Chu, and K. H. Li, "Ultrafast miniaturized GaN-based optoelectronic proximity sensor," *Photon. Res.,* vol. 10, no. 8, pp. 1964-1970, 2022/08/01 2022, doi: 10.1364/PRJ.462933.

[45]   Y. Luo, B. Yu, L. Chen, and K. H. Li, "Micro Humidity Sensor Based on a GaN Chip With Silica Opal," *IEEE Electron Device Letters,* vol. 42, no. 5, pp.

743-746, 2021, doi: 10.1109/LED.2021.3070392.

[46]   X. An, Y. Luo, B. Yu, L. Chen, and K. H. Li, "A Chip-Scale GaN-Based

         Optical Pressure Sensor With Microdome-Patterned Polydimethylsiloxane

         (PDMS)," *IEEE Electron Device Letters,* vol. 42, no. 10, pp. 1532-1535, 2021,

         doi: 10.1109/LED.2021.3103891.

[47]   T.-X. Lee, K.-F. Gao, W.-T. Chien, and C.-C. Sun, "Light extraction analysis

         of GaN-based light-emitting diodes with surface texture and/or patterned

         substrate," *Opt. Express,* vol. 15, no. 11, pp. 6670-6676, 2007/05/28 2007, doi:

         10.1364/OE.15.006670.

[48]   P. Liu, C. She, L. Tan, P. Xu, and L. Yan, "Development of LED Package Heat

         Dissipation Research," *Micromachines*, vol. 13, no. 2*,* doi:

         10.3390/mi13020229.

[49]   H. Wu, "Wire sawing technology: A state-of-the-art review," *Precision

         Engineering,* vol. 43, pp. 1-9, 2016/01/01/ 2016, doi:

         10.1016/j.precisioneng.2015.08.008.

[50]   M. D. Craven, S. H. Lim, F. Wu, J. S. Speck, and S. P. DenBaars, "Structural

         characterization of nonpolar (1120) a-plane GaN thin films grown on (1102) r-

         plane sapphire," *Applied Physics Letters,* vol. 81, no. 3, pp. 469-471, 2002,

         doi: 10.1063/1.1493220.

[51]   S. Jia *et al.*, "A coating-free superhydrophobic sensing material for full-range

         human motion and microliter droplet impact detection," *Chemical Engineering

         Journal,* vol. 410, p. 128418, 2021/04/15/ 2021, doi:

10.1016/j.cej.2021.128418.

[52]   J. A. Hernandez-Valdes, M. Stegge, J. Hermans, J. Teunis, and O. P. Kuipers,

"Enhancement of amino acid production and secretion by Lactococcus lactis

using a droplet-based biosensing and selection system," *Metabolic*

Engineering Communications, vol. 11, p. e00133, 2020.

[53]   R. Panckow, L. Reinecke, M. Cuellar, and S. Maaß, "Photo-Optical In-Situ

Measurement of Drop Size Distributions: Applications in Research and

Industry," *Oil & Gas Science and Technology,* vol. 72, p. 14, 05/01 2017, doi:

10.2516/ogst/2017009.

[54]   K.-C. Liu *et al.*, "A flexible and superhydrophobic upconversion-luminescence

membrane as an ultrasensitive fluorescence sensor for single droplet

detection," *Light: Science & Applications,* vol. 5, no. 8, pp. e16136-e16136,

2016/08/01 2016, doi: 10.1038/lsa.2016.136.

[55]   D. Choi and D. S. Kim, "A Zeta (ζ)-Pipet Tip to Reduce the Spontaneously

Induced Electrical Charge of a Dispensed Aqueous Droplet," *Langmuir,* vol.

30, p. 6644, 2014.

[56]   L. Alwis, T. Sun, and K. T. V. Grattan, "[INVITED] Developments in optical

fibre sensors for industrial applications," *Optics & Laser Technology,* vol. 78,

pp. 62-66, 2016/04/01/ 2016, doi: 10.1016/j.optlastec.2015.09.004.

[57]   J. Tröndle, A. Ernst, W. Streule, R. Zengerle, and P. Koltay, "Non-contact

optical sensor to detect free flying droplets in the nanolitre range," *Sensors*

and Actuators A: Physical, vol. 158, no. 2, pp. 254-262, 2010/03/01/ 2010,

doi: 10.1016/j.sna.2010.01.023.

[58]   L. Liu, S. Korposh, D. Gomez, R. Correia, B. R. Hayes-Gill, and S. P. Morgan, "Localised plasmonic hybridisation mode optical fibre sensing of relative humidity," *Sensors and Actuators B: Chemical,* vol. 353, p. 131157, 2022/02/15/ 2022, doi: 10.1016/j.snb.2021.131157.

[59]   F. Canfarotta *et al.*, "A novel capacitive sensor based on molecularly imprinted nanoparticles as recognition elements," *Biosensors and Bioelectronics,* vol. 120, pp. 108-114, 2018/11/30/ 2018, doi: 10.1016/j.bios.2018.07.070.

[60]   O. Atalay, A. Atalay, J. Gafford, and C. Walsh, "A Highly Sensitive Capacitive-Based Soft Pressure Sensor Based on a Conductive Fabric and a Microporous Dielectric Layer," *Advanced Materials Technologies,* 10.1002/admt.201700237 vol. 3, no. 1, p. 1700237, 2018/01/01 2018, doi: 10.1002/admt.201700237.

[61]   M. H. Zulfiqar, M. Saleem, M. Zubair, M. Q. Mehmood, and K. Riaz, *Foldable, Eco-Friendly and Low-Cost Microfluidic Paper-Based Capacitive Droplet Sensor*. 2020.

[62]   C. Lu *et al.*, "Investigation of the electroluminescence spectrum shift of InGaN/GaN multiple quantum well light-emitting diodes under direct and pulsed currents," *Journal of Applied Physics,* vol. 113, no. 1, p. 013102, 2013/01/07 2013, doi: 10.1063/1.4772683.

[63]   A. Behnood, K. Van Tittelboom, and N. De Belie, "Methods for measuring pH in concrete: A review," *Construction and Building Materials,* vol. 105, pp.

176-188, 2016/02/15/ 2016, doi: 10.1016/j.conbuildmat.2015.12.032.

[64]   M. Yuqing, C. Jianrong, and F. Keming, "New technology for the detection of

pH," *Journal of Biochemical and Biophysical Methods,* vol. 63, no. 1, pp. 1-9,

2005/04/29/ 2005, doi: 10.1016/j.jbbm.2005.02.001.

[65]   J. Yang, T. J. Kwak, X. Zhang, R. McClain, W.-J. Chang, and S. Gunasekaran,

"Digital pH Test Strips for In-Field pH Monitoring Using Iridium Oxide-

Reduced Graphene Oxide Hybrid Thin Films," *ACS Sensors,* vol. 1, no. 10,

pp. 1235-1243, 2016/10/28 2016, doi: 10.1021/acssensors.6b00385.

[66]   E. Ficara, A. Rozzi, and P. Cortelezzi, "Theory of pH-stat titration,"

Biotechnology and Bioengineering, vol. 82, no. 1, pp. 28-37, 2003/04/05 2003,

doi: 10.1002/bit.10541.

[67]   K. Xu, B. Wu, J. Wan, Y. Li, and M. Li, "An All Solid State Electrochemical

pH Sensor Based on Niobium Modified Electrode," *IEEE Sensors Journal,*

vol. 21, no. 24, pp. 27275-27281, 2021, doi: 10.1109/JSEN.2021.3123633.

[68]   D. J. Graham, B. Jaselskis, and C. E. Moore, "Development of the Glass

Electrode and the pH Response," *Journal of Chemical Education,* vol. 90, no.

3, pp. 345-351, 2013/03/12 2013, doi: 10.1021/ed300246x.

[69]   S. Ohkuma and B. Poole, "Fluorescence probe measurement of the

intralysosomal pH in living cells and the perturbation of pH by various

agents," *Proceedings of the National Academy of Sciences,* vol. 75, no. 7, pp.

3327-3331, 1978/07/01 1978, doi: 10.1073/pnas.75.7.3327.

[70]   W. Tan, Z. Y. Shi, and R. Kopelman, "Development of submicron chemical

fiber optic sensors," *Analytical Chemistry,* vol. 64, no. 23, pp. 2985-2990, 1992/12/01 1992, doi: 10.1021/ac00047a019.

[71]   M. Garc á-Heras, C. Gil, N. Carmona, J. Faber, K. Kromka, and M. A. Villegas, "Optical behaviour of pH detectors based on sol–gel technology," *Analytica Chimica Acta,* vol. 540, no. 1, pp. 147-152, 2005/05/17/ 2005, doi: 10.1016/j.aca.2004.09.031.

[72]   J. Y. Ding, M. R. Shahriari, and G. H. Sigel, "Porous Fiber Optical Sensor For pH Measurement," in *8th Optical Fiber Sensors Conference*, 29-31 Jan. 1992 1992, pp. 321-324, doi: 10.1109/OFS.1992.763098.

[73]   J. Zha and H. Roggendorf, "Sol–gel science, the physics and chemistry of sol–gel processing, Ed. by C. J. Brinker and G. W. Scherer, Academic Press, Boston 1990, xiv, 908 pp., bound—ISBN 0-12-134970-5," *Advanced Materials,* vol. 3, no. 10, pp. 522-522, 1991/10/01 1991, doi: 10.1002/adma.19910031025.

[74]   C.-Y. Li *et al.*, "A wide pH range optical sensing system based on a sol–gel encapsulated amino-functionalised corrole," *Analyst,* 10.1039/B514510D vol. 131, no. 3, pp. 388-393, 2006, doi: 10.1039/B514510D.

[75]   K. Ertekin, C. Karapire, S. Alp, B. Yenig ül, and S. I ḑi, "Photophysical and photochemical characteristics of an azlactone dye in sol-gel matrix; a new fluorescent pH indicator," *Dyes and Pigments,* vol. 56, no. 2, pp. 125-133, 2003/02/01/ 2003, doi: 10.1016/S0143-7208(02)00125-0.

[76]   M. Chen, S. G. J. Heijman, and L. C. Rietveld, "State-of-the-Art Ceramic

Membranes for Oily Wastewater Treatment: Modification and Application,"
Membranes, vol. 11, no. 11, doi: 10.3390/membranes11110888.

[77]   L. L. Hench and J. K. West, "The sol-gel process," *Chemical Reviews,* vol. 90,
no. 1, pp. 33-72, 1990/01/01 1990, doi: 10.1021/cr00099a003.

[78]   J. Konishi, K. Fujita, K. Nakanishi, and K. Hirao, "Monolithic TiO2 with
Controlled Multiscale Porosity via a Template-Free Sol−Gel Process
Accompanied by Phase Separation," *Chemistry of Materials,* vol. 18, no. 25,
pp. 6069-6074, 2006/12/01 2006, doi: 10.1021/cm0617485.

[79]   G. W. Scherer, "Aging and drying of gels," *Journal of Non-Crystalline Solids,*
vol. 100, no. 1, pp. 77-92, 1988/03/01/ 1988, doi: 10.1016/0022-
3093(88)90008-7.

[80]   C. M. Chan, G. Z. Cao, H. Fong, M. Sarikaya, T. Robinson, and L. Nelson,
"Nanoindentation and adhesion of sol-gel-derived hard coatings on polyester,"
Journal of Materials Research, vol. 15, no. 1, pp. 148-154, 2000/01/01 2000,
doi: 10.1557/JMR.2000.0025.

[81]   F. Hoffmann, M. Cornelius, J. Morell, and M. Fröba, "Silica-Based
Mesoporous Organic–Inorganic Hybrid Materials," *Angewandte Chemie
International Edition,* vol. 45, no. 20, pp. 3216-3251, 2006/05/12 2006, doi:
10.1002/anie.200503075.

[82]   J. Šefčik and A. V. McCormick, "Kinetic and thermodynamic issues in the
early stages of sol-gel processes using silicon alkoxides," *Catalysis Today,* vol.
35, no. 3, pp. 205-223, 1997/03/28/ 1997, doi: 10.1016/S0920-

5861(96)00158-7.

[83]   R. Jae Chul and J. C. In, "Structures and properties of silica gels prepared by the sol—gel method," *Journal of Non-Crystalline Solids,* vol. 130, no. 1, pp. 8-17, 1991/06/01/ 1991, doi: 10.1016/0022-3093(91)90151-U.

[84]   F. Rubio, J. Rubio, and J. L. Oteo, "A FT-IR Study of the Hydrolysis of Tetraethylorthosilicate (TEOS)," *Spectroscopy Letters,* vol. 31, no. 1, pp. 199-219, 1998/01/01 1998, doi: 10.1080/00387019808006772.

[85]   R. Mukkamala and H. M. Cheung, "Acid and base effects on the morphology of composites formed from microemulsion polymerization and sol–gel processing," *Journal of Materials Science,* vol. 32, no. 17, pp. 4687-4692, 1997/09/01 1997, doi: 10.1023/A:1018610426210.

[86]   F. B. M. Suah, M. Ahmad, and M. N. Taib, "Applications of artificial neural network on signal processing of optical fibre pH sensor based on bromophenol blue doped with sol–gel film," *Sensors and Actuators B: Chemical,* vol. 90, no. 1, pp. 182-188, 2003/04/20/ 2003, doi: 10.1016/S0925-4005(03)00026-1.

[87]   A. Bhat, J. M. Amanor-Boadu, and A. Guiseppi-Elie, "Toward Impedimetric Measurement of Acidosis with a pH-Responsive Hydrogel Sensor," *ACS Sensors,* vol. 5, no. 2, pp. 500-509, 2020/02/28 2020, doi: 10.1021/acssensors.9b02336.

[88]   Y. Ko, H. Y. Jeong, G. Kwon, D. Kim, C. Lee, and J. You, "pH-responsive polyaniline/polyethylene glycol composite arrays for colorimetric sensor application," *Sensors and Actuators B: Chemical,* vol. 305, p. 127447,

2020/02/15/ 2020, doi: 10.1016/j.snb.2019.127447.

[89]   L. Ding *et al.*, "A naked-eye detection polyvinyl alcohol/cellulose-based pH sensor for intelligent packaging," *Carbohydrate Polymers,* vol. 233, p. 115859, 2020/04/01/ 2020, doi: 10.1016/j.carbpol.2020.115859.

[90]   J. J. García-Guzmán, C. Pérez-Ràfols, M. Cuartero, and G. A. Crespo, "Toward In Vivo Transdermal pH Sensing with a Validated Microneedle Membrane Electrode," *ACS Sensors,* vol. 6, no. 3, pp. 1129-1137, 2021/03/26 2021, doi: 10.1021/acssensors.0c02397.

[91]   T. Siripongpreda, B. Somchob, N. Rodthongkum, and V. P. Hoven, "Bacterial cellulose-based re-swellable hydrogel: Facile preparation and its potential application as colorimetric sensor of sweat pH and glucose," *Carbohydrate Polymers,* vol. 256, p. 117506, 2021/03/15/ 2021, doi: 10.1016/j.carbpol.2020.117506.

[92]   S. NajafiKhoshnoo *et al.*, "A 3D Nanomaterials-Printed Wearable, Battery-Free, Biocompatible, Flexible, and Wireless pH Sensor System for Real-Time Health Monitoring," *Advanced Materials Technologies,* vol. 8, no. 8, p. 2201655, 2023/04/01 2023, doi: 10.1002/admt.202201655.

[93]   M. Khatib and H. Haick, "Sensors for Volatile Organic Compounds," *ACS Nano,* vol. 16, no. 5, pp. 7080-7115, 2022/05/24 2022, doi: 10.1021/acsnano.1c10827.

[94]   A. G. Fung *et al.*, "Wearable Environmental Monitor To Quantify Personal Ambient Volatile Organic Compound Exposures," *ACS Sensors,* vol. 4, no. 5,

pp. 1358-1364, 2019/05/24 2019, doi: 10.1021/acssensors.9b00304.

[95]   X. Chen *et al.*, "Portable Analytical Techniques for Monitoring Volatile

Organic Chemicals in Biomanufacturing Processes: Recent Advances and

Limitations," *Frontiers in Chemistry,* Mini Review vol. 8, 2020. [Online].

Available: https://www.frontiersin.org/articles/10.3389/fchem.2020.00837.

[96]   W. A. Byers and S. P. Perone, "Generation of an electrochemical data base for

pattern recognition," *Analytical Chemistry,* vol. 55, no. 4, pp. 615-620,

1983/04/01 1983, doi: 10.1021/ac00255a008.

[97]   Z. Li *et al.*, "Multiplexed Analysis of Photochemical Oxidants Using a

Nanoparticle-Based Optoelectronic Nose," *Analytical Chemistry,* vol. 93, no.

41, pp. 13990-13997, 2021/10/19 2021, doi: 10.1021/acs.analchem.1c03457.

[98]   Z. Xie *et al.*, "An Optical Nose Chip Based on Mesoporous Colloidal Photonic

Crystal Beads," *Advanced Materials,* vol. 26, no. 15, pp. 2413-2418,

2014/04/01 2014, doi: 10.1002/adma.201304775.

[99]   Z. Li, J. R. Askim, and K. S. Suslick, "The Optoelectronic Nose: Colorimetric

and Fluorometric Sensor Arrays," *Chemical Reviews,* vol. 119, no. 1, pp. 231-

292, 2019/01/09 2019, doi: 10.1021/acs.chemrev.8b00226.

[100]   J. Hou, M. Li, and Y. Song, "Recent advances in colloidal photonic crystal

sensors: Materials, structures and analysis methods," *Nano Today,* vol. 22, pp.

132-144, 2018/10/01/ 2018, doi: 10.1016/j.nantod.2018.08.008.

[101]   J. D. Joannopoulos, P. R. Villeneuve, and S. Fan, "Photonic crystals," *Solid

State Communications,* vol. 102, no. 2, pp. 165-173, 1997/04/01/ 1997, doi:

10.1016/S0038-1098(96)00716-8.

[102] C. Huang, Y. Cheng, Z. Gao, H. Zhang, and J. Wei, "Portable label-free inverse opal photonic hydrogel particles serve as facile pesticides colorimetric monitoring," *Sensors and Actuators B: Chemical,* vol. 273, pp. 1705-1712, 2018/11/10/ 2018, doi: 10.1016/j.snb.2018.07.050.

[103] H. Fudouzi, "Fabricating high-quality opal films with uniform structure over a large area," *Journal of Colloid and Interface Science,* vol. 275, no. 1, pp. 277-283, 2004/07/01/ 2004, doi: 10.1016/j.jcis.2004.01.054.

[104] C. Fenzl, T. Hirsch, and O. S. Wolfbeis, "Photonic Crystals for Chemical Sensing and Biosensing," *Angewandte Chemie International Edition,* vol. 53, no. 13, pp. 3318-3335, 2014/03/24 2014, doi: 10.1002/anie.201307828.

[105] Y. J. Lee and P. V. Braun, "Tunable Inverse Opal Hydrogel pH Sensors," *Advanced Materials,* vol. 15, no. 7-8, pp. 563-566, 2003/04/17 2003, doi: 10.1002/adma.200304588.

[106] A. K. Yetisen, I. Naydenova, F. da Cruz Vasconcellos, J. Blyth, and C. R. Lowe, "Holographic Sensors: Three-Dimensional Analyte-Sensitive Nanostructures and Their Applications," *Chemical Reviews,* vol. 114, no. 20, pp. 10654-10696, 2014/10/22 2014, doi: 10.1021/cr500116a.

[107] H. Fudouzi and Y. Xia, "Photonic Papers and Inks: Color Writing with Colorless Materials," *Advanced Materials,* vol. 15, no. 11, pp. 892-896, 2003/06/05 2003, doi: 10.1002/adma.200304795.

[108] H. Zhang, L. Lin, D. Liu, Q. Chen, and J. Wu, "Optical nose based on porous

silicon photonic crystal infiltrated with ionic liquids," *Analytica Chimica Acta,* vol. 953, pp. 71-78, 2017/02/08/ 2017, doi: 10.1016/j.aca.2016.11.053.

[109] C. V. Rumens, M. A. Ziai, K. E. Belsey, J. C. Batchelor, and S. J. Holder, "Swelling of PDMS networks in solvent vapours; applications for passive RFID wireless sensors," *Journal of Materials Chemistry C,* 10.1039/C5TC01927C vol. 3, no. 39, pp. 10091-10098, 2015, doi: 10.1039/C5TC01927C.

[110] C. K. Yeom, H. K. Kim, and J. W. Rhim, "Removal of trace VOCs from water through PDMS membranes and analysis of their permeation behaviors," *Journal of Applied Polymer Science,* vol. 73, no. 4, pp. 601-611, 1999/07/25 1999, doi: 10.1002/(SICI)1097-4628(19990725)73:4<601::AID-APP16>3.0.CO;2-#.

[111] R. Kanawade *et al.*, "Negative axicon tip-based fiber optic interferometer cavity sensor for volatile gas sensing," *Opt. Express,* vol. 27, no. 5, pp. 7277-7290, 2019/03/04 2019, doi: 10.1364/OE.27.007277.

[112] R. Zhang *et al.*, "Metal–Organic Framework Crystal-Assembled Optical Sensors for Chemical Vapors: Effects of Crystal Sizes and Missing-Linker Defects on Sensing Performances," *ACS Applied Materials & Interfaces,* vol. 11, no. 23, pp. 21010-21017, 2019/06/12 2019, doi: 10.1021/acsami.9b05933.

[113] J. F. Olorunyomi *et al.*, "Advancing Metal-Organic Frameworks toward Smart Sensing: Enhanced Fluorescence by a Photonic Metal-Organic Framework for Organic Vapor Sensing," *Advanced Optical Materials,* vol. 8, no. 19, p.

2000961, 2020/10/01 2020, doi: 10.1002/adom.202000961.

[114] D. Yan *et al.*, "Flexible construction of cellulose photonic crystal optical sensing nano-materials detecting organic solvents," *Analyst,* 10.1039/C8AN01236A vol. 144, no. 6, pp. 1892-1897, 2019, doi: 10.1039/C8AN01236A.

[115] C. Li, L. Li, S. Yu, X. Jiao, and D. Chen, "High Performance Hollow Metal–Organic Framework Nanoshell-Based Etalons for Volatile Organic Compounds Detection," *Advanced Materials Technologies,* vol. 1, no. 7, p. 1600127, 2016/10/01 2016, doi: 10.1002/admt.201600127.

[116] S. Yu, X. Wang, X. Jiao, C. Li, and D. Chen, "Polyhedral metal–organic framework monolayer colloidal crystals with sharpened and crystal facet-dependent selectivity for organic vapor sensing," *Journal of Materials Chemistry C,* 10.1039/D1TC00810B vol. 9, no. 16, pp. 5379-5386, 2021, doi: 10.1039/D1TC00810B.